POLITECNICO DI TORINO

Collegio di Ingegneria Meccanica, Aerospaziale, dell'Autoveicolo e della Produzione

Corso di Laurea Magistrale

in Mechanical Engineering

Tesi di Laurea Magistrale

Investigation of the dynamic behaviour of underplatform dampers

Relatori

Prof. Teresa Berruti, Politecnico di Torino

Prof. Daniele Botto, Politecnico di Torino

Prof. Farid Amirouche, University of Illinois at Chicago

Prof. Mario Guagliano, Politecnico di Milano

Candidato

Adrian Vladimir Sernaque Chuncho

Ottobre 2018

ACKNOWLEDGMENTS

I want to sincerely thank my advisor and my family for their support during the thesis work.

AS

TABLE OF CONTENTS

TABLE OF CONTENTS (continued)

<u>CHAPTER</u> <u>PAGE</u>

TABLE OF CONTENTS (continued)

LIST OF TABLES

LIST OF FIGURES

LIST OF FIGURES (continued)

FIGURE **PAGE**

LIST OF FIGURES (continued)

FIGURE **PAGE**

CHAPTER 1

1 INTRODUCTION

1.1 Vibration in turbines

The main cause of failure in turbines is due to the fact that they usually work close to resonance frequencies. Therefore, particular devices, the so-called "underplatform dampers", are required in order to dissipate the energy produced by the vibrations through friction in the contact with the blades, pressed against the platforms by the centrifugal force as shown in . Even though they may seem to be simple, their design is far from being straightforward: the mass is fundamental since the centrifugal force is proportional to it and the geometry must perfectly adapt to the underplatorm, allowing the dissipation of the highest amount of energy.

1.2 Thesis approach and aim

The starting point of the thesis is the data already available from experiments carried out at the Politecnico di Torino in 2006. Not only they allow drawing a comparison in order to understand the validity of the obtained final results in the end, but are fundamental in the intermediate process in order to check the correctness of the followed steps.

Throughout the thesis there are two parallel processes, that meet at the end in order to yield the final results: on one hand we have the creation of the full Finite Element model, and the verification of its consistency along the path that bring it to be used as an input for the non-linear numerical method; on the other hand we have the numerical tool[1] described in

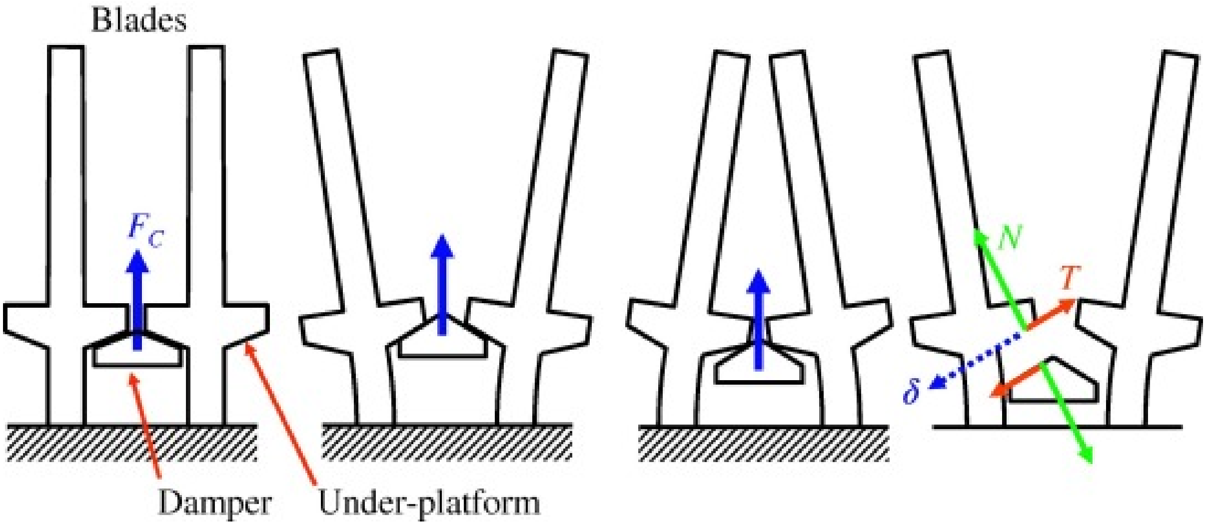

Figure 1: Underplatform damper working principle

Appendix C, which needs to be adapted and verified in order to have attendable results, which will be the input for the first process.

1.3 Thesis overview

The thesis can be considered as divided into three main parts. The first part deals with the description of the physical experiments as they were carried out, which provided the experimental data that serves as a final term of comparison for the obtained results throughout the work.

The second part deals with the first verifications of the steps followed and the tools to be used, such as the verification of the FE models and of the numerical method used to find the stiffness values.

The last part instead, deals with the actual calculation of such parameters which serve as an input for the non-linear numerical tool, allowing a final comparison with the experimental results.

CHAPTER 2

PHYSICAL EXPERIMENTS

2.1 General description

A campaign of experiments were carried out at the LAQ AERMEC laboratory at the Politecnico di Torino in 2005[2]. The obtained results in these experiments are used as a main reference to draw a comparison with and to discuss the results that are found in the steps followed throughout the work.

The experiments simulated two adjacent turbine's blades in order to study their response to an exciting force into two different conditions:

- Free condition, without a damper in between the blades in order to study the natural resonance frequencies of the system, such that in the end it is possible to better appreciate the effect of the dampers on the blades' vibration.
- Forced condition, with the damper in position, while one of the blades is directly excited and the amplitude response is measured.

Moreover, experiments were performed for two types of dampers, a symmetric damper and an asymmetric one, which will be described into detail in the following sections. The damper is kept in place by two couples of steel wires, pulling the damper upwards, in order to simulate the centrifugal forces acting on it, as it will be explained in 2.3. The blades and the dampers are all made of steel and their material properties are sum up in Table Table I. The overall

TABLE I: STEEL PROPERTIES

Elastic modulus	200 MPa
Poisson's ratio	0.3
Density	7800 Kg/m^3

experiment layout is shown in the sketch in Figure 2

2.2 Blades characteristics and dimensions

In the experiments two types of blades were used and each of them is attached to a base which is the same for both. In Figure 3 we can see the main dimensions of the base. In Figure 4 we have the top view showing the position where the blades are attached in.

The dimensions of the two blades are reported in Figure 5 and in Figure 6. It is important to notice the angles in the middle part of the blades on each side, which are fundamental for the contact area with the damper. When performing the experiments with the two different dampers, the only difference was in the blades arrangement.

Two supporting spines are used in order to keep the basis aligned throughout the experiment, passing through the two holes present in each of them. The alignment is shown in Figure 7.

The bases are constrained by an hydraulic press able to exert up to 700bar on their lateral faces, in order to keep them motionless during the experiment. The areas the pressure is applied on, can be seen in Figure 2.

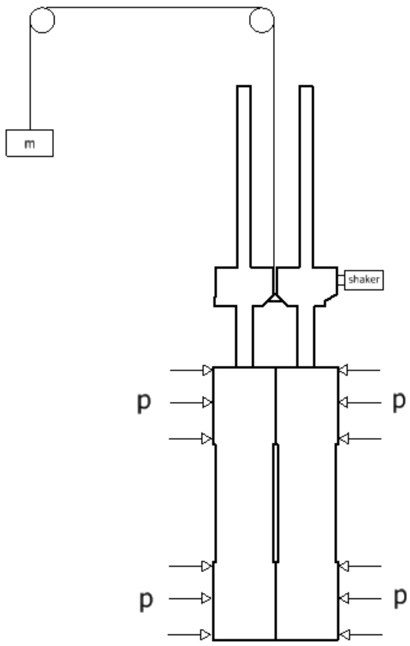

Figure 2: Experiment layout

2.3 Centrifugal force

The turbine's rotation generates the centrifugal force that presses the damper towards the under platforms according to

$$F_C = m\omega r \tag{2.1}$$

where m is the damper's mass, ω is the angular velocity and r the distance from the rotation axes. In the experiments the centrifugal force is simulated by two couple of steel wires, which pull the damper upwards. In order not to generate an unwanted rotation of the damper, they pass through the barycentre when inside the body. The wires are directly connected to a system

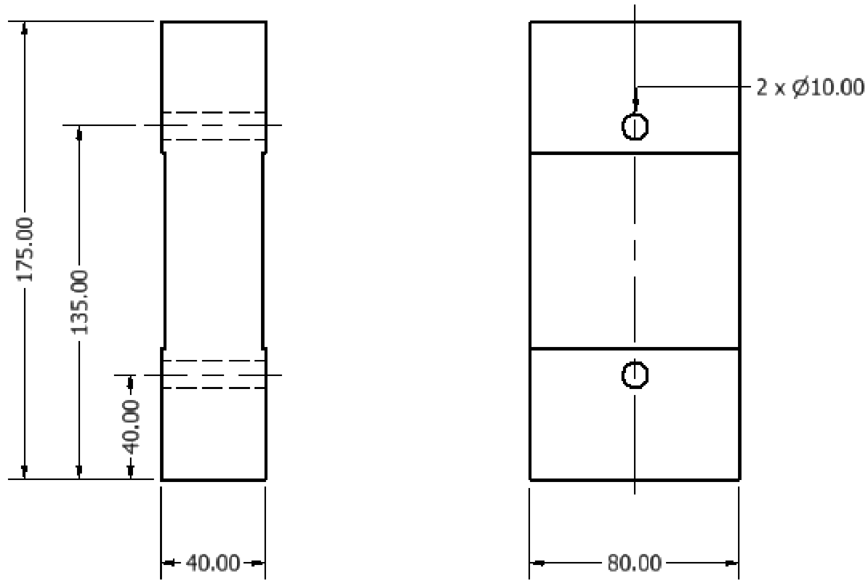

Figure 3: Dimensions of the base

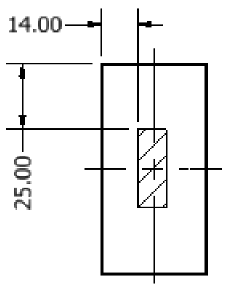

Figure 4: Top view of the view

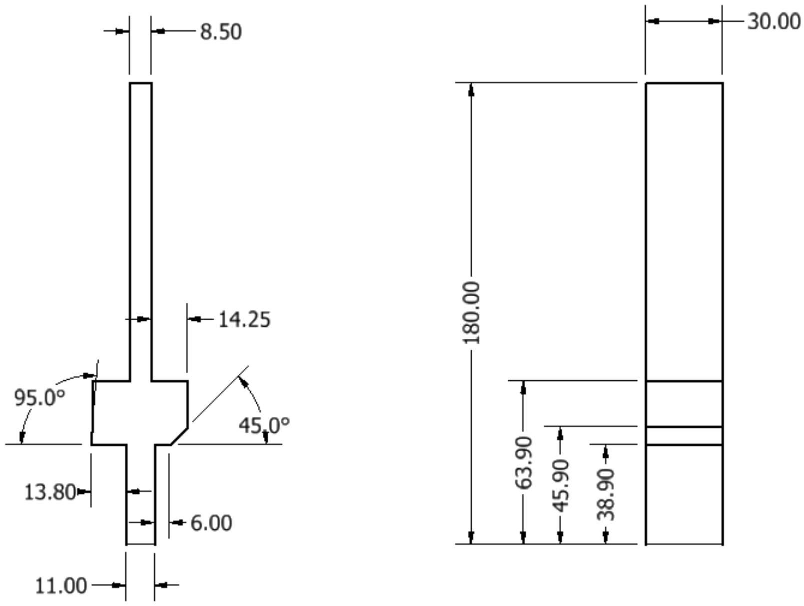

Figure 5: Dimensions of the right blade

of pulleys, with a mass attached to its end, as shown in Figure 2, and they are placed such that they do not interfere with the experiment procedure. The simulated centrifugal force will be simply

$$F_C = mg \tag{2.2}$$

where g is the acceleration gravity equal to 9,81 $\frac{m}{s^2}$, and m is the mass attached to the wires.

2.4 Excitation sytem

The exciting force is provided by an electromagnetic shaker, which must be isolated in working conditions in order not to influence the experiment results with its resonance frequency. Therefore, an ad-hoc structure was adopted, which the shaker is attached to through four helical

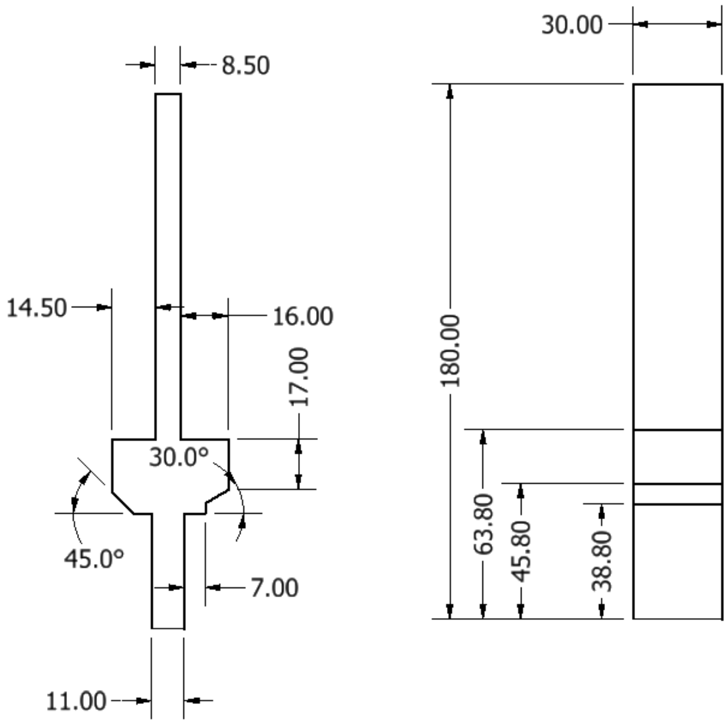

Figure 6: Dimensions of the left blade

Figure 7: Spines used for basis alignment

springs, as shown in Figure 8. The exciting force is applied on the middle point of the blade's core on the right-hand side in both experiments.

2.5 Response measurement technique

The amplitude of the response is registered by two piezoelectric transducers, which measure the acceleration. Since their signal is usually weak, an amplifier is required. They are placed at about 5 mm from the top edge of the external face of the two blades. The response which is actually taken into account is the one of the blade on the left-hand side, which is the one not directly excited by the shaker.

Figure 8: Shaker and its structure

2.6 Symmetric damper

2.6.1 Geometry and dimensions

The symmetric damper presents two angles of 45° at the bottom and its length matches the platform width. In Figure 9 we show its dimensions and the position of the holes where the steel wires pass in.

2.6.2 Experiment configuration

The arrangement of the two blades in the experiments involving the symmetric damper, can be seen in Figure 10, with the faces showing the 45° angles opposite to each other. The point of view of this picture will be the standard front view we will have in all the figures regarding the models of the experiments.

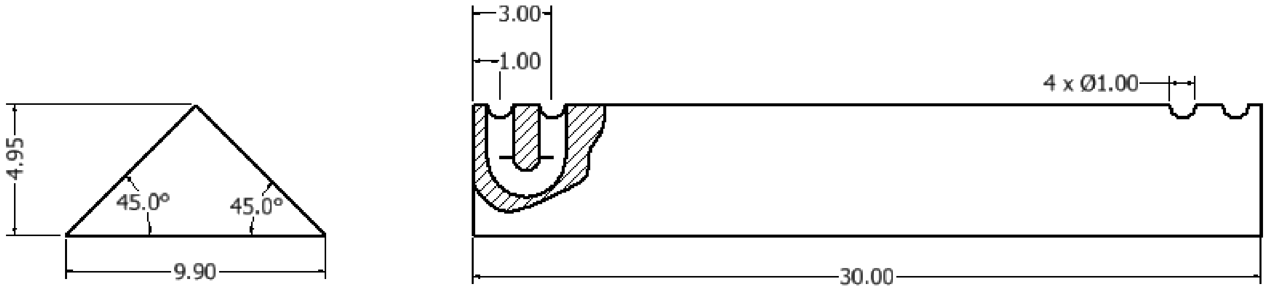

Figure 9: Main dimensions in the symmetric damper

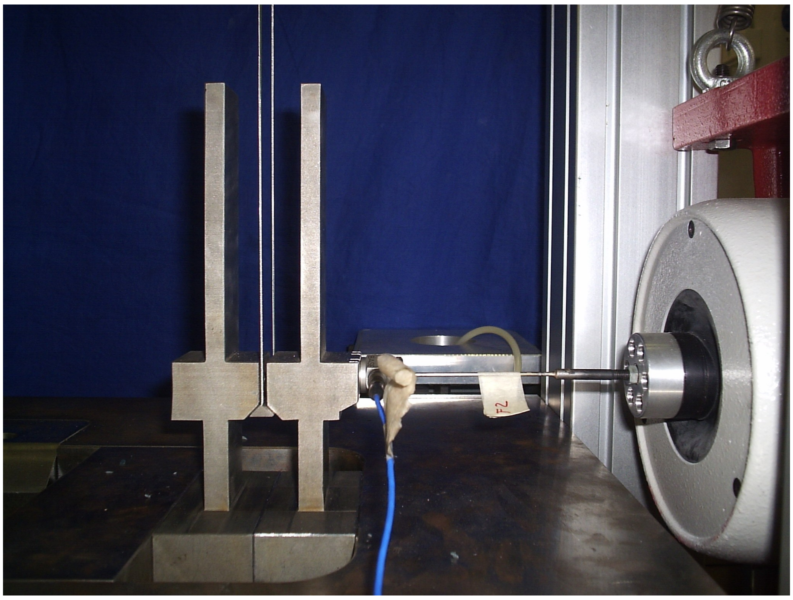

Figure 10: Layout for the symmetric damper experiments

TABLE II: SYMMETRIC CASE MAIN RESULTS

Free condition	First eigenfrequency	295 Hz
Forced condition	First eigenfrequency	-
	Second eigenfrequency	340 Hz

2.6.3 Main results

The main results regard the the response amplitude as a function of the exciting frequency, both for the free and forced condition. In the free condition the first natural frequencies, as expected, corresponds to the one of the single blades, since no damper is present yet and there is no coupling. The plots are shown in Figure 11; along the x-axes we find the exciting frequencies while on the y-axes we have the ratio of the measured amplitude of the acceleration to the magnitude of the exciting force.

However, throughout this work, we will be mainly interested in the condition which more closely resembles the stick condition. Therefore, among the curves present in Figure 11, we will focus on the one related to the highest F_e to F_c ratio. For easiness, in Table II we can find the numerical values of the main results which will be useful in the subsequent steps.

2.6.4 Damper condition after experiments

By looking at the damper after the experiments, we can easily notice some worn areas on the faces that were in contact with the underplatform. It is important to well identify their location within the contact area, in order to verify and discuss the results that will be obtained when applying the numerical method. In Figure Figure 12 a picture of the damper is presented.

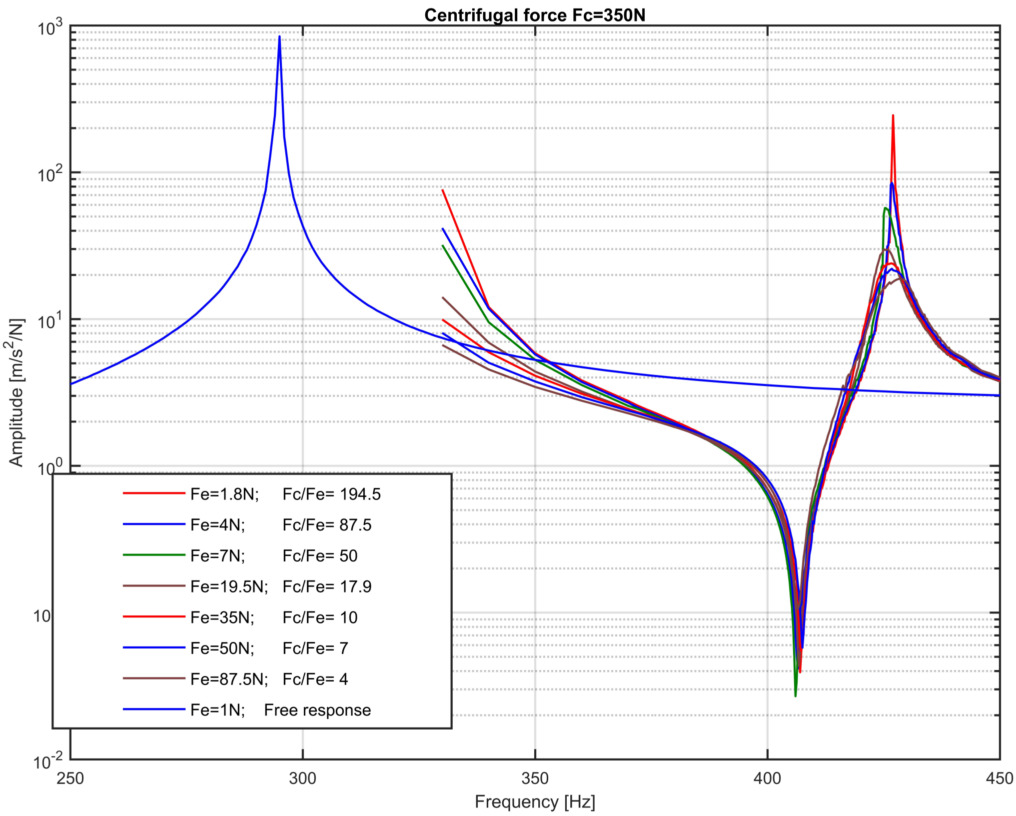

Figure 11: Symmetric damper response: free and force condition

Figure 12: Symmetric damper condition after experiments

2.7 Asymmetric damper

2.7.1 Geometry and dimensions

For the asymmetric damper we have two different angles at its bottom: a 60° degree and a 95° degree angle, the third angle consequently being of 25°. Moreover, the surface in contact is no longer completely plane, as for the symmetric damper, but presents two separate cases. Therefore, the contact area will be smaller. Moreover, if we consider one of the couple of wires that are pulling the damper upwards, we can notice that each of them is passing below the cases. The main dimensions and the holes position for the wires are shown in Figure 13.

2.7.2 Experiment configuration

The blades are arranged in a different way for this type a damper: both the blades are turned by 180° such that in between we have the space for the asymmetric damper. However,

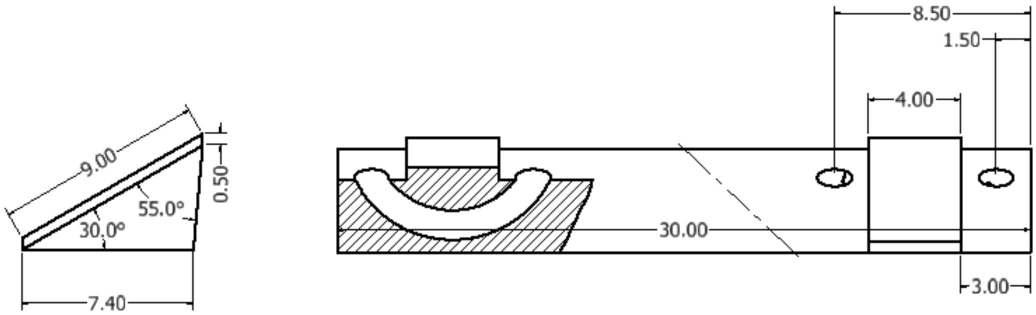

Figure 13: Main dimensions in the asymmetric damper

it is always the right blade which is directly excited by the shaker. The overall arrangement is shown in Figure 14.

2.7.3 Main results

The natural frequencies for the free condition are expected to be equal to the ones already found in the symmetric-damper case, since it coincides with the resonance frequency of a single blade, and only the arrangement has been changed. In Figure 15 we can see the plot for the free condition and force condition, for different F_C to F_e ratios.

As already mentioned for the symmetric case, for the forced experiments we will mainly focus on the condition which is closest to the stuck one. The main values are reported in Table III.

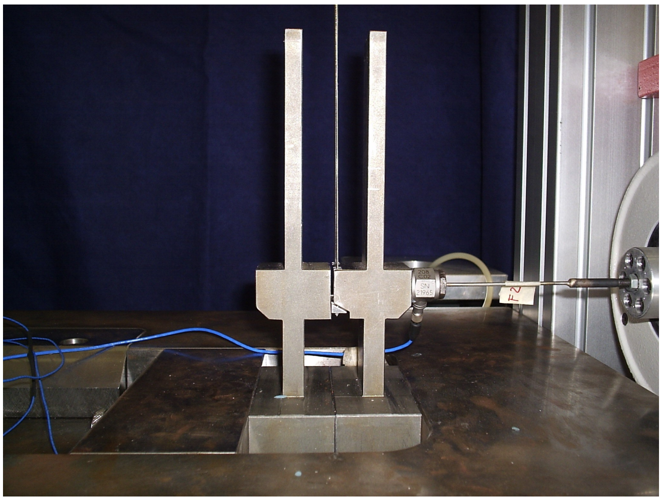

Figure 14: Layout for asymmetric damper experiments

TABLE III: ASYMMETRIC CASE MAIN RESULTS

Free condition	First eigenfrequency	295 Hz
Forced condition	First eigenfrequency	377 Hz
	Second eigenfrequency	440 Hz

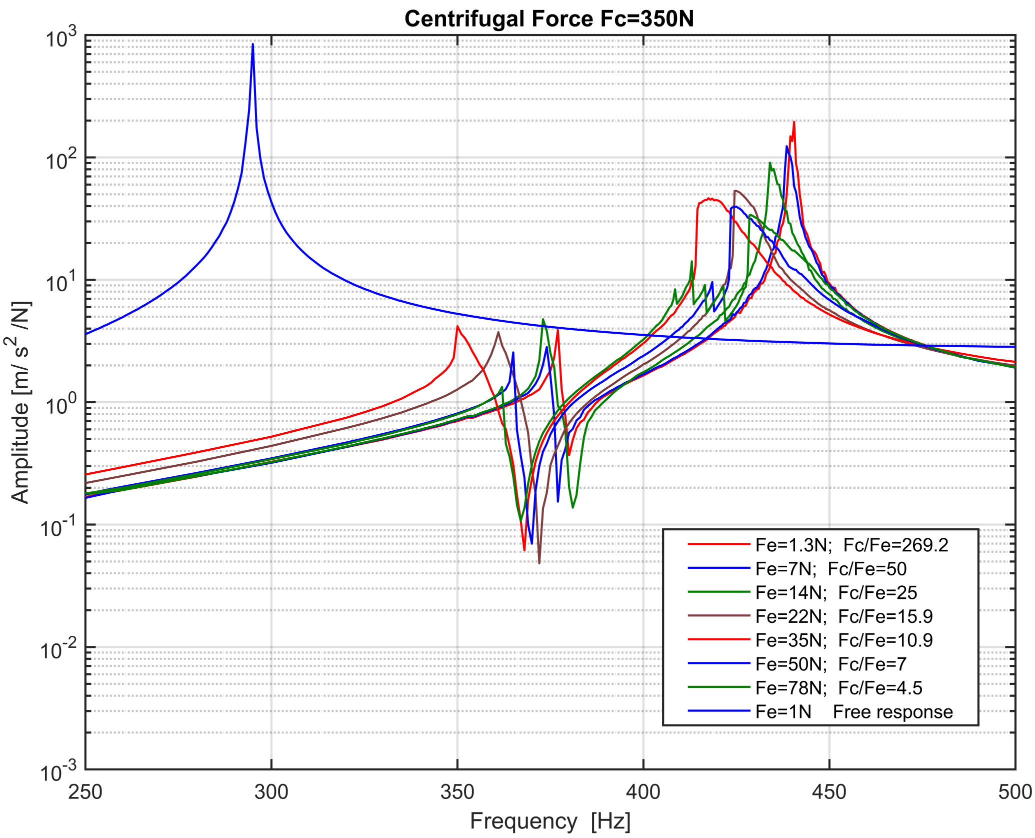

Figure 15: Asymmetric damper response: free and forced condition

2.7.4 Damper condition after experiments

Also in this case, it is interesting to notice the worn zones in the contact area, which is smaller with respect to the previous case. One worn area is present in each 'gradino', and it is found in between the holes were the wires are located. In Figure 16 we have a clear view of the contact area on the damper's face.

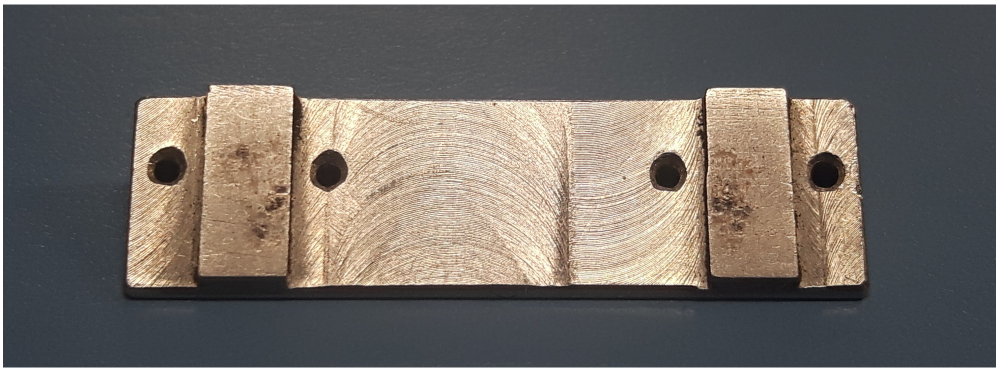

Figure 16: Asymmetric damper condition after experiments

CHAPTER 3

FE MODELS IN ANSYS

All the models were first created in Solidworks, following the dimensions of the components involved in the experiments and subsequently imported into Ansys APDL. Across the chapter, the FE model of each part is shown into detail with its main features.

3.1 Blades

Once the models with the symmetric and asymmetric dampers are assembled in Solidworks, resembling the arrangement of the experiments as were shown in Figure 10 and Figure 14, they need to be imported into Ansys APDL, by using any of the available formats. We decided to use the ACIIS format, which has a .sat extension.

In Ansys we will find two different volumes, one for each blade, which needed to be split into smaller and more uniform volumes in order to have a higher control over the generated mesh, which is fundamental in some critical areas. The whole meshing process followed for both cases is carefully described into Appendix A.

Particular attention was paid to the top end of the blades and to the part connecting the core to the bases since there are the parts which are most demanded during the vibration. The meshed volume of the top was made up of 920 hexahedral elements, while the lower volume of 260 elements. For the two bases instead, a free meshed was chosen since they were not much interested by vibrations since they were well-constrained.

3.2 Symmetric damper

Besides the simulations in section —, dampers' FE models are not required in most of the following steps. However, they allow having a clearer and immediate view of the contact points on the dampers face. The faces of the symmetric damper which are to be in contact with the underplatform were meshed with 40 quadrilateral elements each. In Figure 17 we can see the FE model.

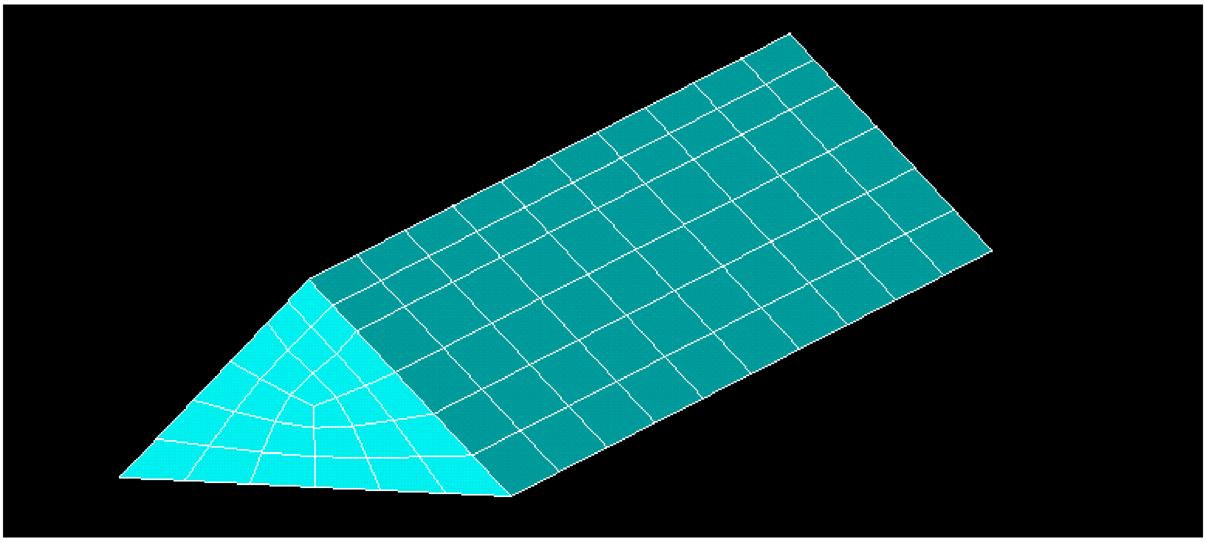

Figure 17: Fe model of the symmetric damper

3.3 Asymmetric damper

The asymmetric damper was divided into three smaller volumes: one for the core and two for the two cases in order to have a more regular mesh. Each contact area is meshed with 18 elements. The FE model can be seen in Figure 18.

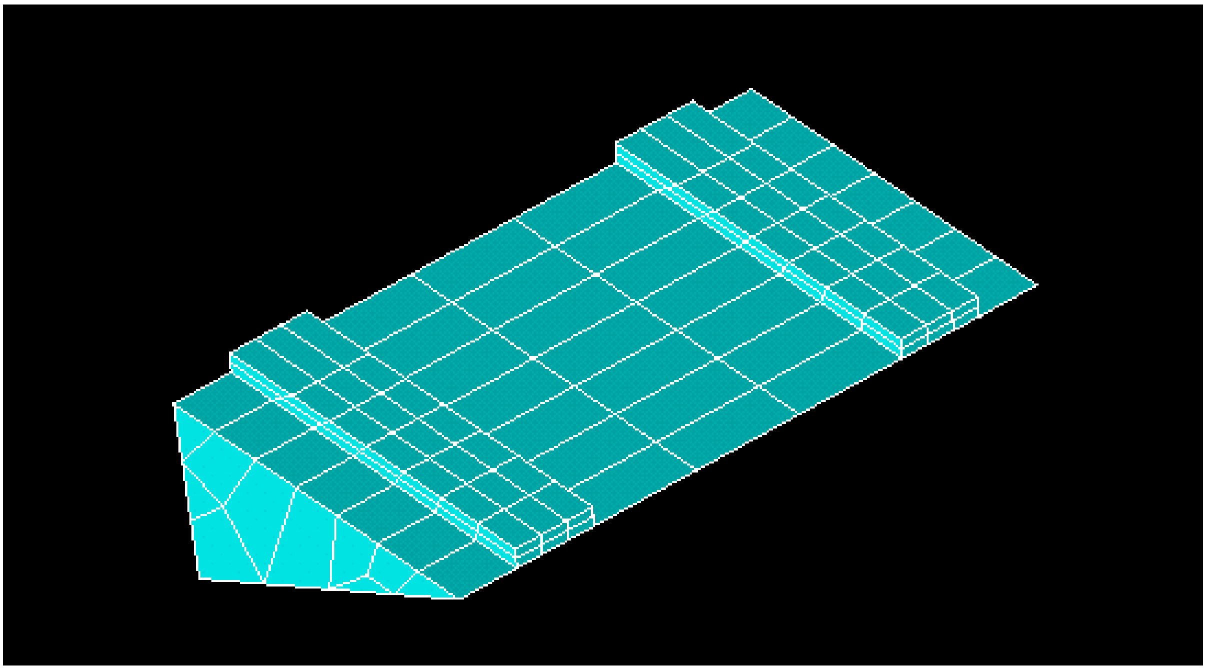

Figure 18: Fe model of the asymmetric damper

3.4 Contact area

3.4.1 Symmetric damper case

A critical step was the meshing process of the contact areas between the damper and the platform: the mesh on the two areas must superpose perfectly, such that we are able to merge their nodes, otherwise the damper will completely detach when running the simulations in Ansys for the forced condition.

Therefore, when preparing the damper and the platform for the meshing process, on both bodies we divided the faces in contact, creating a new area that corresponds to the contact region. The contact area on the two sides is shown in Figure 19 and Figure 20.

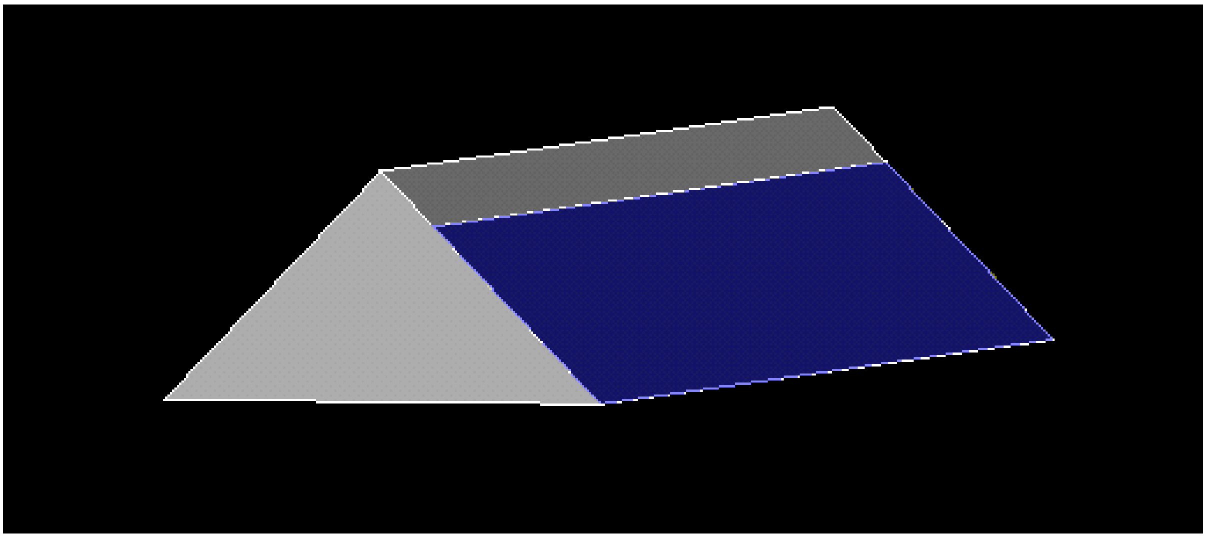

Figure 19: Contact area on symmetric damper face

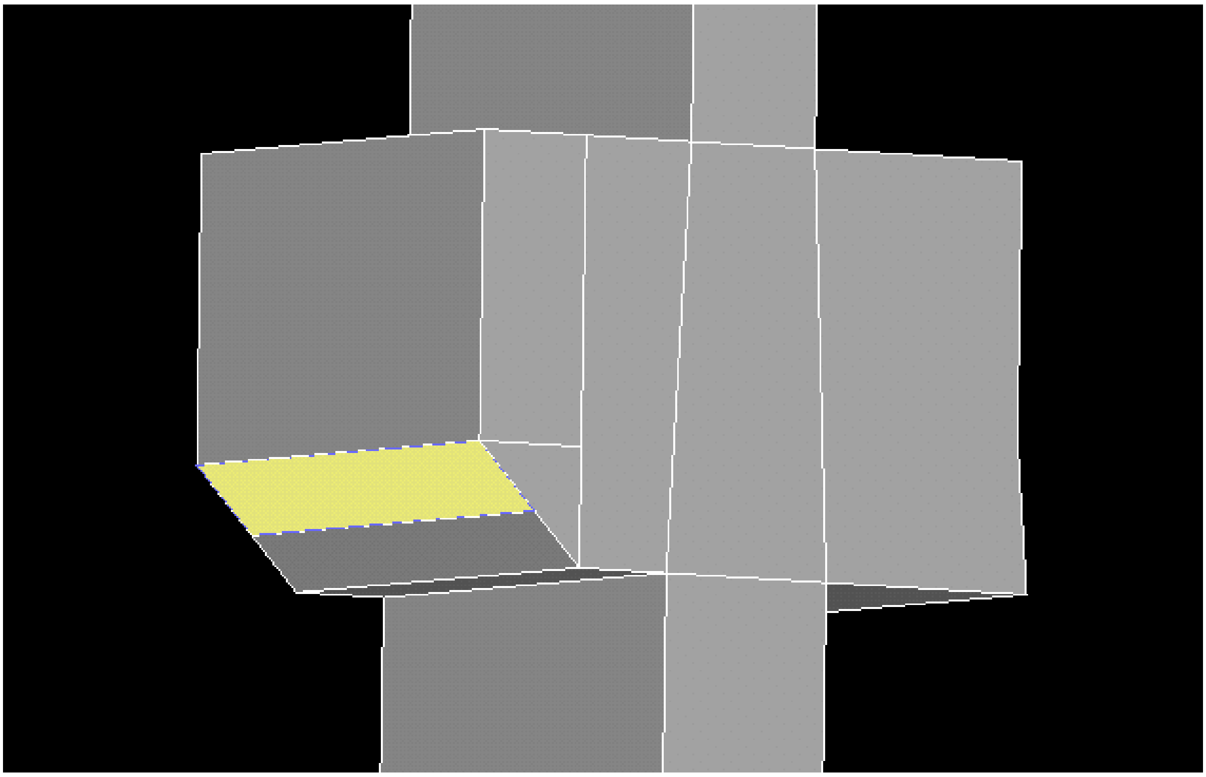

Figure 20: Contact area on blade face

At this point, since the areas are exactly the same on the damper's and platform's side, it is sufficient to mesh the edges of the contact area on each side with the same number of elements, and subsequently mesh the area with quadrilaterals elements. In Figure 21 and Figure 22 we can see the meshed contact area on both bodies, noticing how they perfectly match.

In the end, merging nodes is carried out without any further issue.

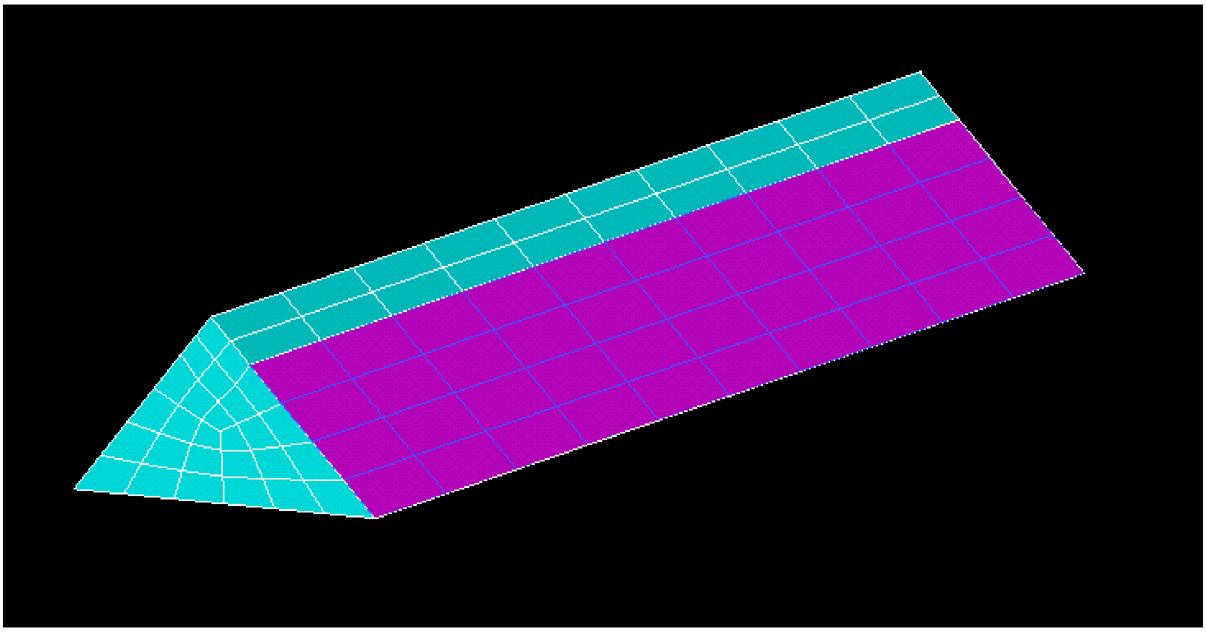

Figure 21: Meshed contact area on symmetric damper face

3.4.2 Asymmetric damper case

The same procedure applied to the symmetric case, holds for the asymmetric damper. The only difference is that on the platform's side, the face needed to be further split in order to match the area of the two cases on the damper's surface. In Figure 23 and Figure 24 we can see the underlined meshed contact areas on the bodies.

3.5 Final FE models

The final assemblies which represent the starting points for the following-up steps, for both cases, can be seen in Figure 25 and Figure 25.

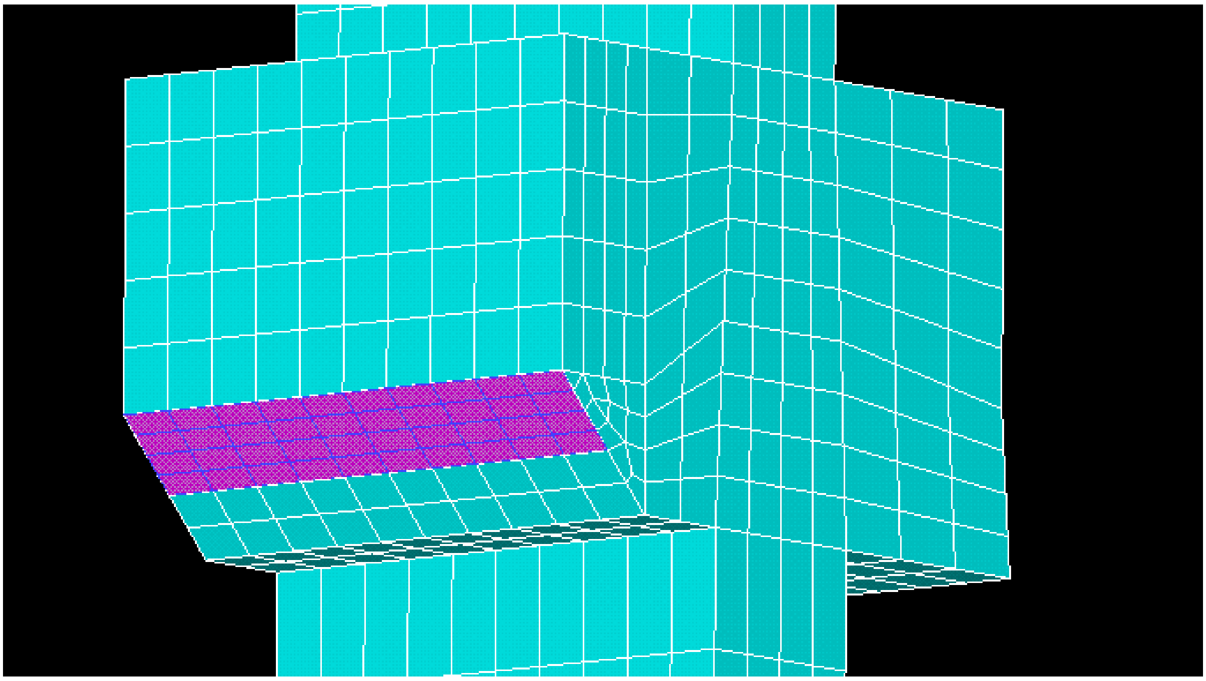

Figure 22: Meshed contact area on blade face

3.6 Applied constraints

Only one constraint is applied on the model, it is the one simulating the hydraulic press on the base lateral surfaces, which was shown in Figure 2. Therefore, we set a null displacement along any direction for those surfaces. The constrained surfaces are shown in Figure 27.

3.7 Loads and accelerometers application nodes

Since it will come useful for the next steps, it is necessary to identify the nodes corresponding to the point where the load is applied by the shaker and the ones where the accelerometers are placed. We consider the shaker to apply the exciting force in one point only, in the middle node on the right face of the blade, as shown in Figure 28.

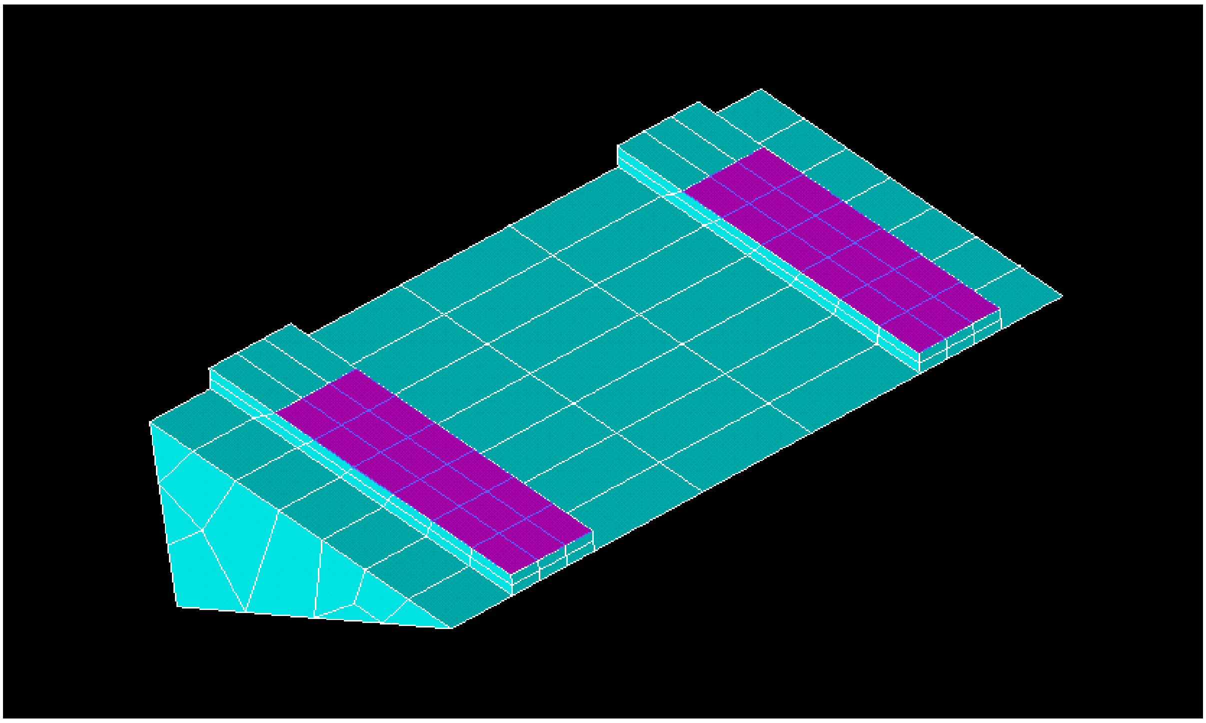

Figure 23: Contact area on asymmetric damper face

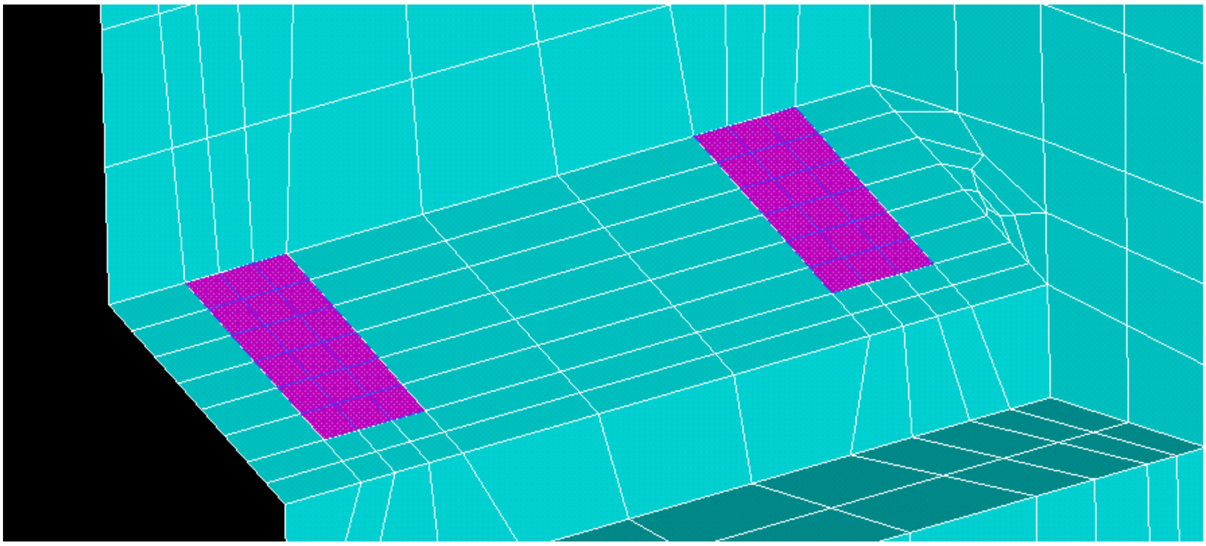

Figure 24: Contact area on asymmetric damper face

While for the accelerometers position, two nodes on the external faces of the blades were identified as shown in Figure Figure 29 and Figure 30.

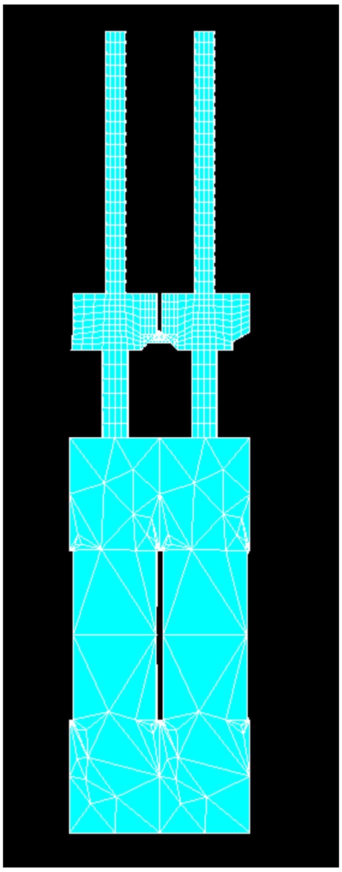

Figure 25: FE model for symmetric damper experiments

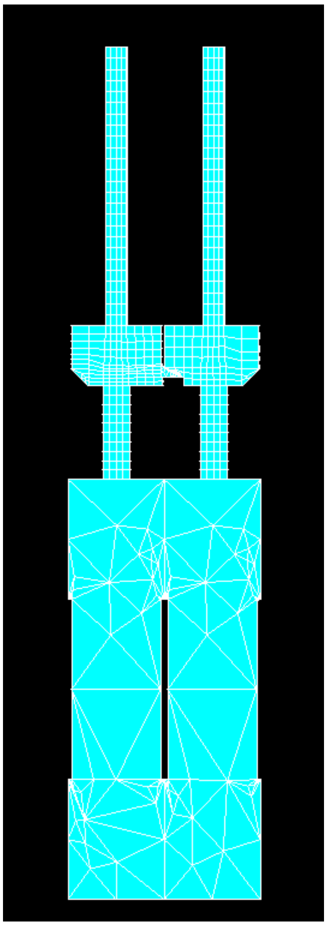

Figure 26: FE model for asymmetric damper experiments

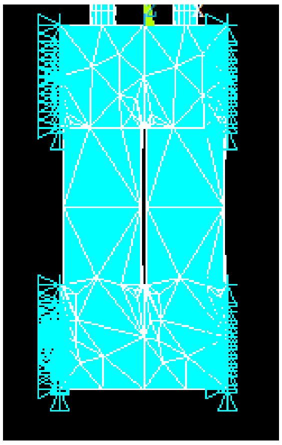

Figure 27: Surfaces constrained

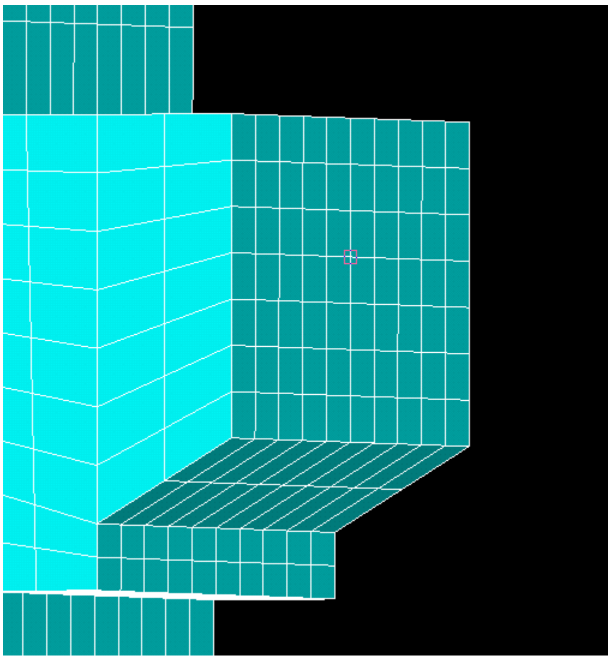

Figure 28: Node of application load

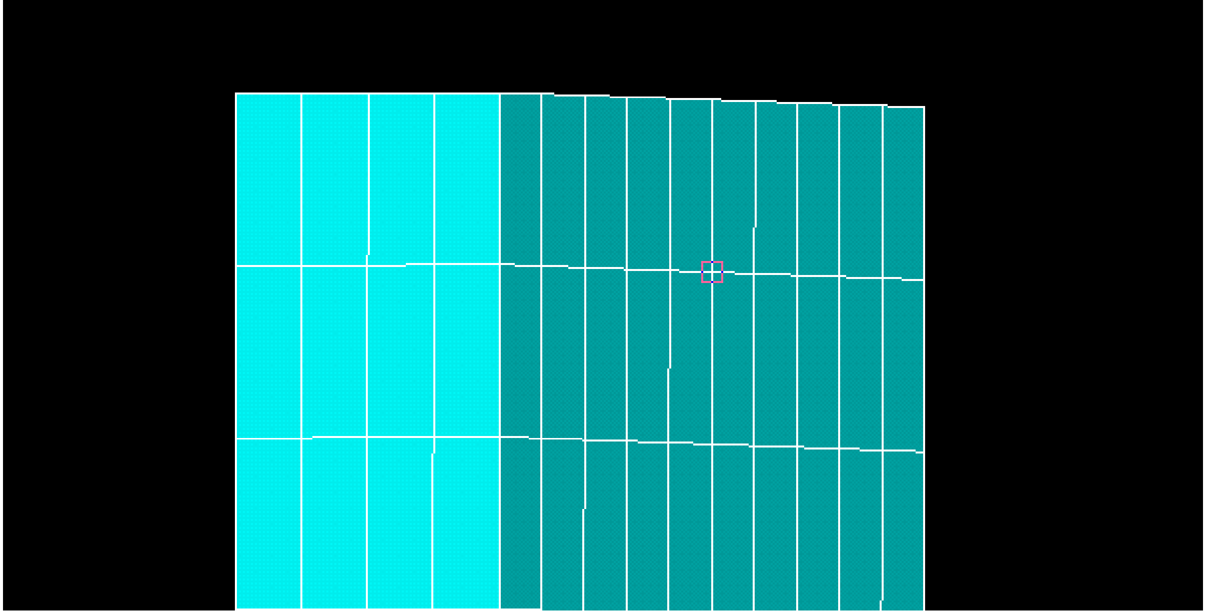

Figure 29: Node for the accelerometer on the left blade

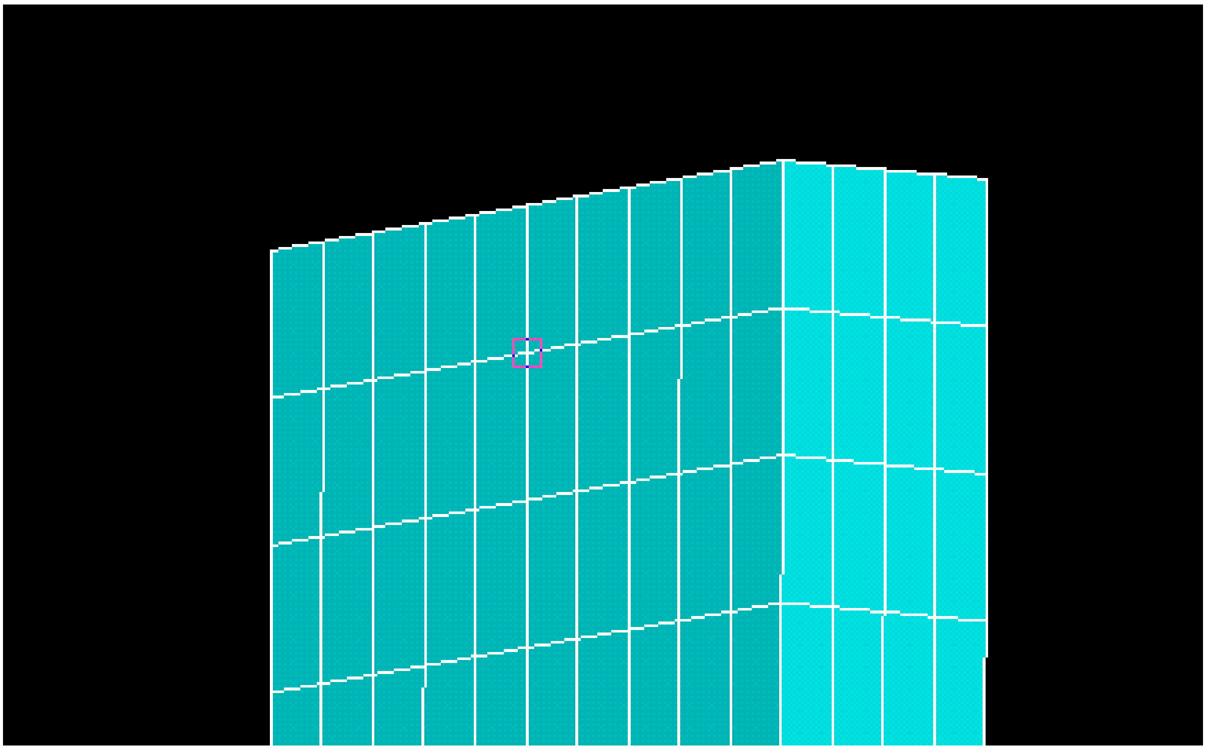

Figure 30: Node for the accelerometer on the right blade

CHAPTER 4

MODAL ANALYSIS IN FREE AND 'GLUED' CONDITION

4.1 Modal analysis in Ansys in free condition

A modal analysis extended to the first four natural frequencies was performed since it will come useful in the following section. However, only the first one was use to check the consistency of the model by drawing a comparison with the experimental results, since it was the only one available. The four modes are shown in Figure 31. As expected, we can see that the found eigenfrequencies of the system coincide with the one of each blade as if they are alone since there is not any kind of coupling yet.

4.2 Comparison with experimental results

In Table IV we reported the results of the modal analysis performed in Ansys and the one obtained in the experiments. The modal analysis was performed both for symmetric and the asymmetric case models even though ideally they should match since the blades are the same, but small differences may be present due to the different meshing.

We can see that the frequency of the first modes of the modal analysis for both cases is significantly close to the experimental result, therefore, there is no need to perform a tuning in order to make them match. Moreover, all the frequencies of the remaining modes actually match, further validating the consistency of the FE models created in Ansys APDL.

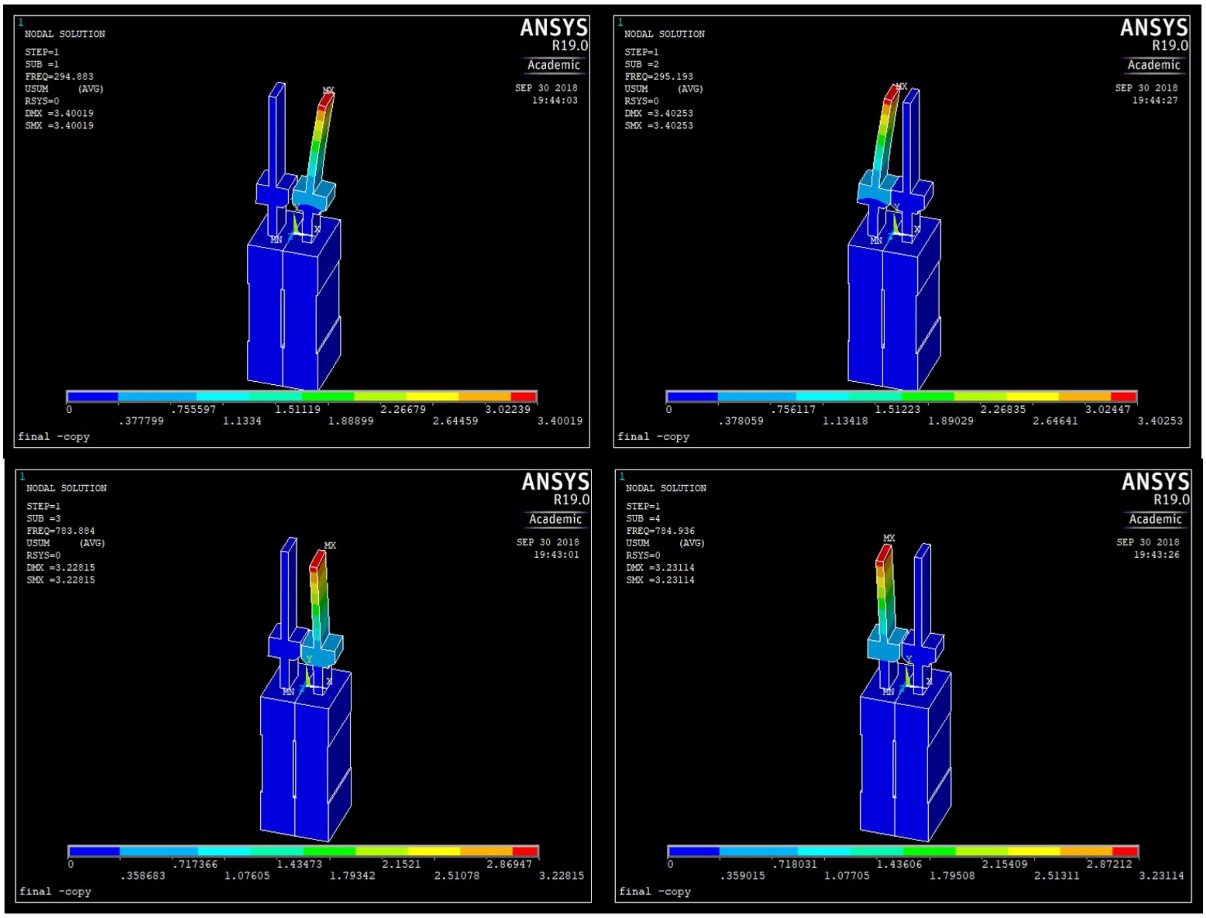

Figure 31: Free condition modal analysis

TABLE IV: COMPARISON FREE CONDITION

	Experiment [Hz]	**Symmetric conf. [Hz]**	Asymmetric conf.[Hz]
First mode	295	294.88	294.77
Second mode	-	295.19	294.78
Third mode	-	783.88	784.06
Fourth mode	-	784.94	784.29

TABLE V: FORCED CONDITION MODAL ANALYSIS

	Modal Analysis symmetric conf, [Hz]
First mode	446.60
Second mode	463.92
Third mode	783.97
Fourth mode	1030.10

4.3 Modal analysis in Ansys in 'glued' condition

In order not to have a complete detachment of the damper from the underplatforms, we need to merge the nodes in the contact area, which becomes, indeed, a unique shared area between the two bodies in contact. Therefore, we have a 'glued' condition, since no relative normal displacement is allowed for any couple of opposite nodes. The result is that the system behaves as if it was a single body. In Figure 32 we have the first four modes found in the modal analysis, while in Table V. we have the values of their frequencies.

Even though the obtained results are not to be compared with the experiments, since it is an unrealistic condition, it sets an upper limit to the eigenfrequencies in the forced condition such that we can know how far we are from this extreme case.

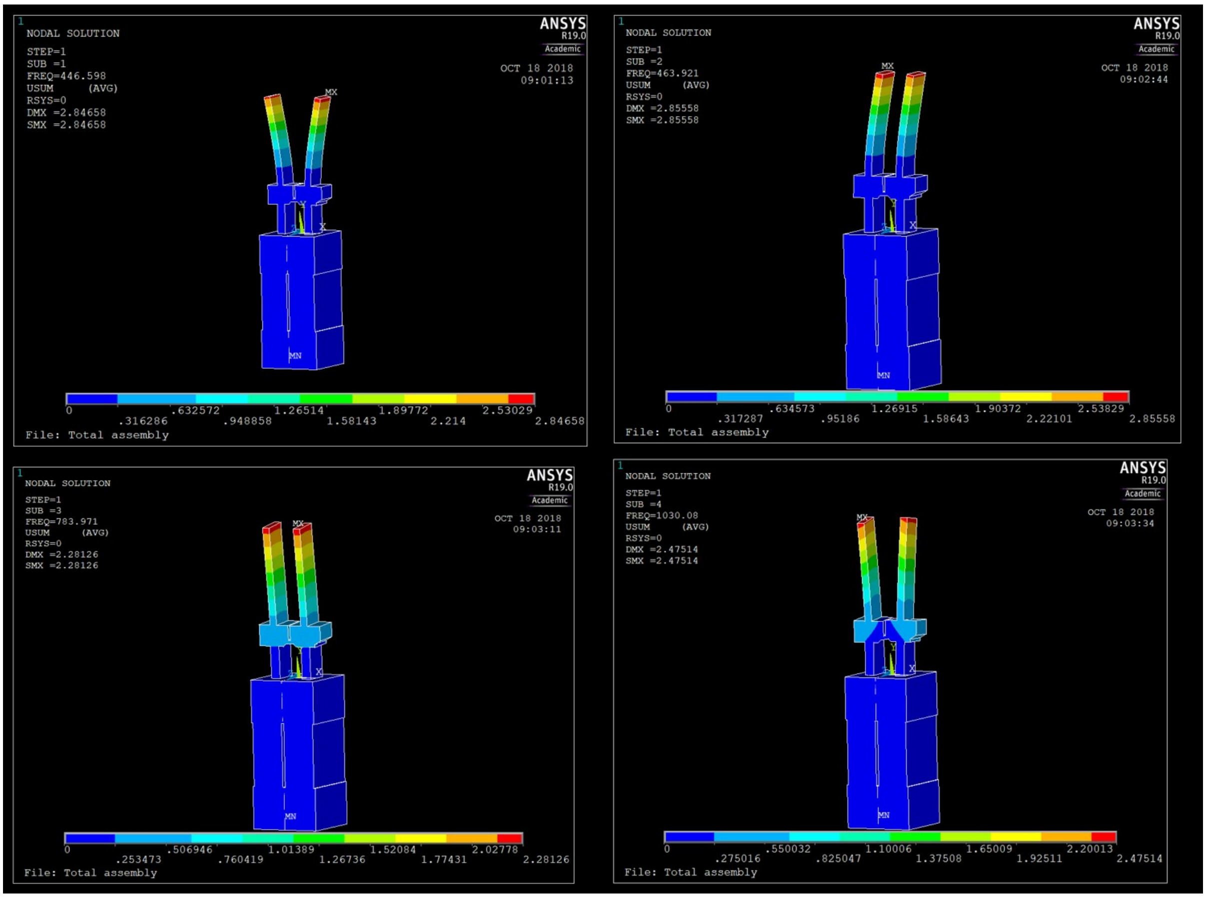

Figure 32: Glued condition modal analysis

CHAPTER 5

LINEAR FREE CONDITION SIMULATION

The aim of this chapter is to verify the correctness of the masss and stiffness matrices, M and K, after they have been extracted from the full FE model and reduced via the Craig-Bampton condensation method. Therefore, we consider the linear part of the numerical method explained in Appendix B, used to calculate the response in the free and forced condition. Moreover, it will also allow us performing a tuning process if required.

5.1 Free condition: results and comparison

The first four natural frequencies for the free condition were calculated. The output plot for the symmetric case is shown inFigure 33, along with the experimental one for an immediate comparison.

Even if the frequency actually matches, there is a clear difference in the amplitude. Therefore, we perform a tuning process by working on the damping coefficients, which is an input parameter for the non-linear part as well. We can perform a further comparison with the modal frequencies found in the Ansys simulations as shown in Table VI. We consider only the symmetric case, since as seen in the previous section, the values are almost identical.

We can clearly see how they actually match, or differ by a small percentage. Therefore, the results obtained with the numerical method are consistent with those found so far.

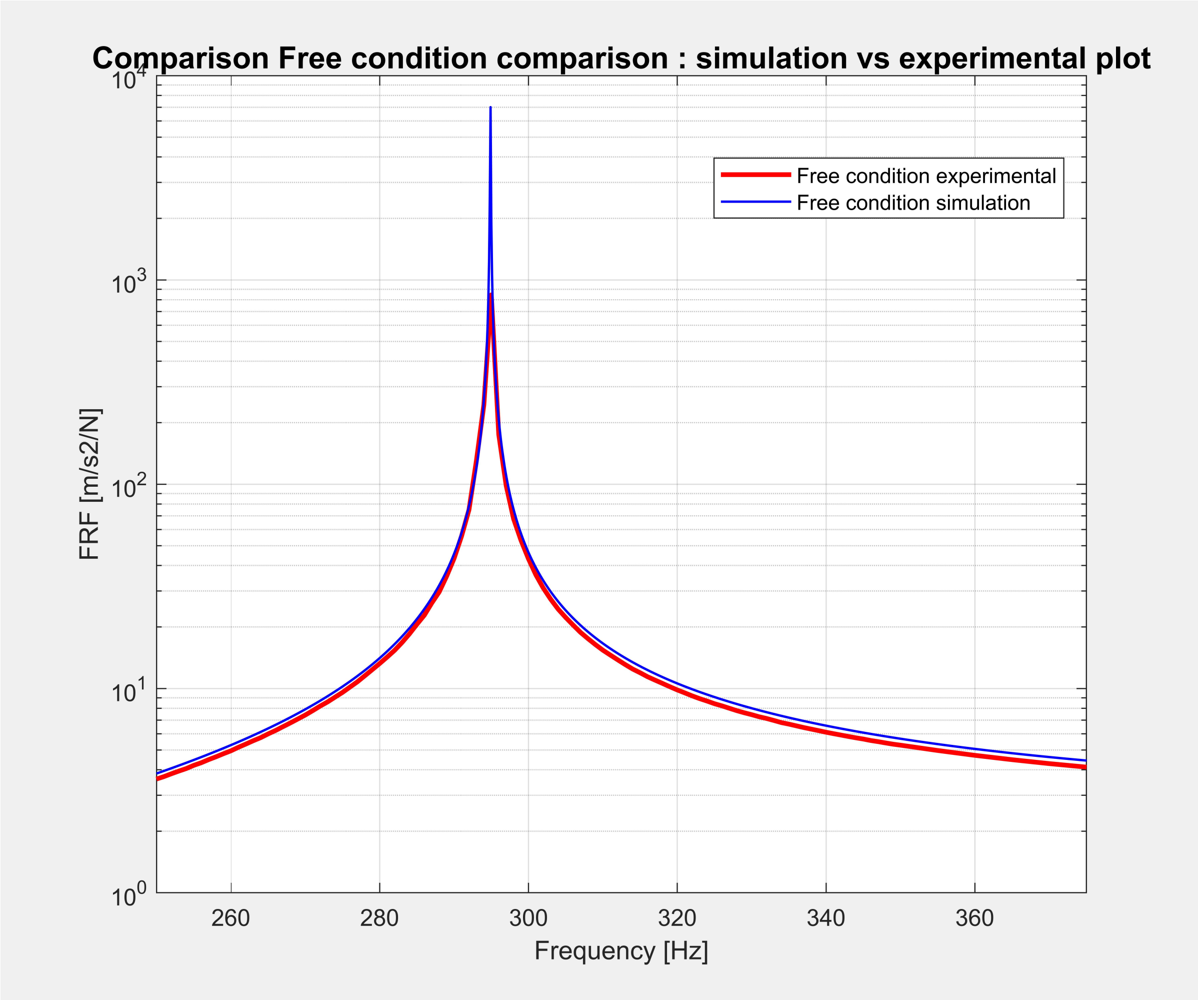

Figure 33: Free condition

TABLE VI: COMPARISON FOR THE FREE CONDITION IN THE SYMMETRIC CASE

	Ansys [Hz]	**MATLAB [Hz]**	
First mode	295	294.88	294.89
Second mode	-	295.19	295.20
Third mode	-	783.88	784.08
Fourth mode	-	784.94	784.98

CHAPTER 6

NUMERICAL METHOD VALIDATION: HALF-SPHERE WITH PLANE CONTACT CASE

In order to verify the solutions provided by the implemented numerical method to obtain the k_n and k_t, we consider a Hertzian geometry, a half-sphere in contact with a half-plane, for which closed-form solutions[3] are already available in the literature such that we can perform an immediate comparison of the results.

6.1 Dimensions and FE model

We modelled a half-sphere, while the plane geometry is provided by the surface of a cube. Both the diameter of the half-sphere and the cube's edge have a length of 10 mm. The reference system's origin is placed on the axis of the two bodies, laying on the half-sphere plane.The z-axis is normal to it and positive directed from the cube towards the half-sphere. A fundamental requirement is to have a regular mesh in the potential contact area on both bodies. Moreover, within the contact area, each couple of nodes, one on the half-sphere and one on the plane, must have the same x and y coordinates, such that when we have the vertical displacement and they come into contact, the nodes in the mesh can superposed one over the other. In order to satisfy this requirement, a well-defined approach was found and followed. It is explained into detail in Appendix A. In Figure 34 we have a lateral view of the FE model.

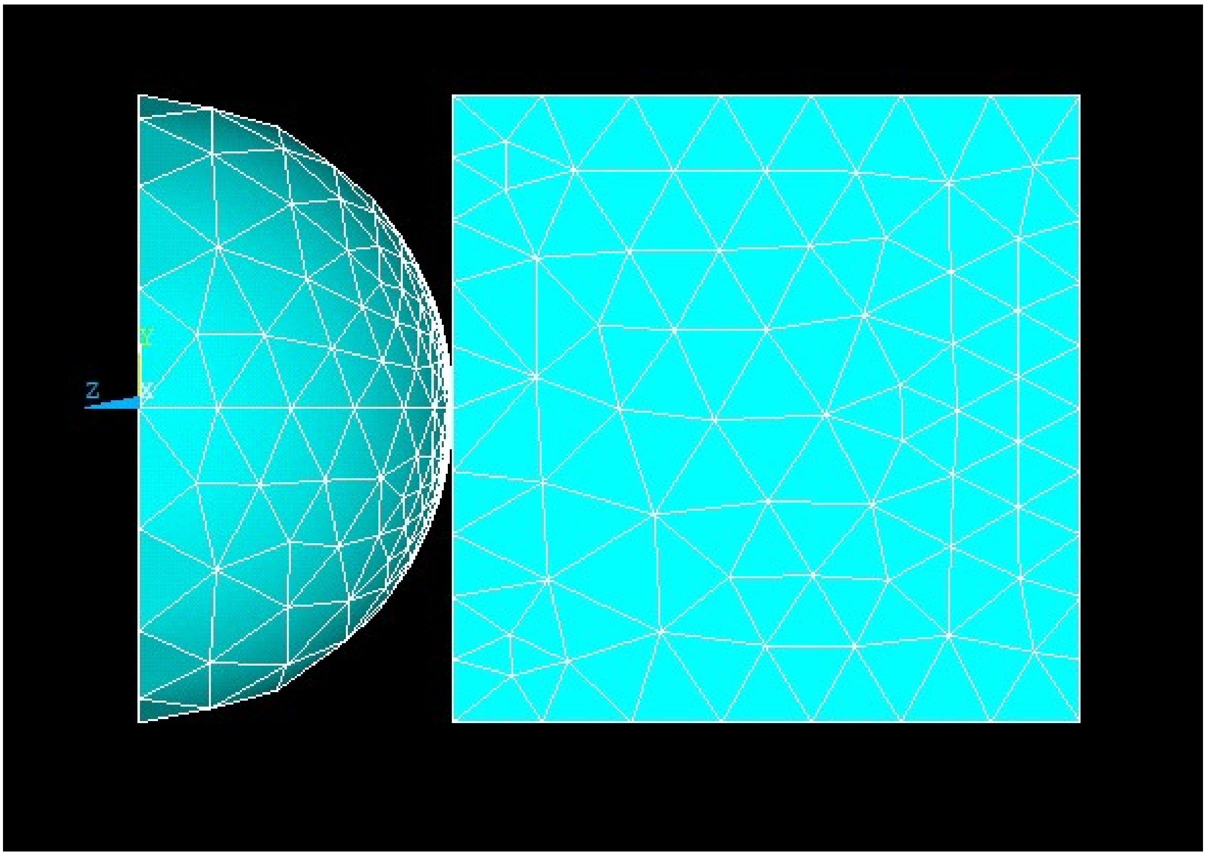

Figure 34: FE model of the semisphere and cube model

The potential contact area was considered to be a square with an edge of 1mm, meshed with 1600 quadrilateral elements, that is 40 elements on each side. The final mesh on both bodies can be seen in Figure 35 and Figure 36.

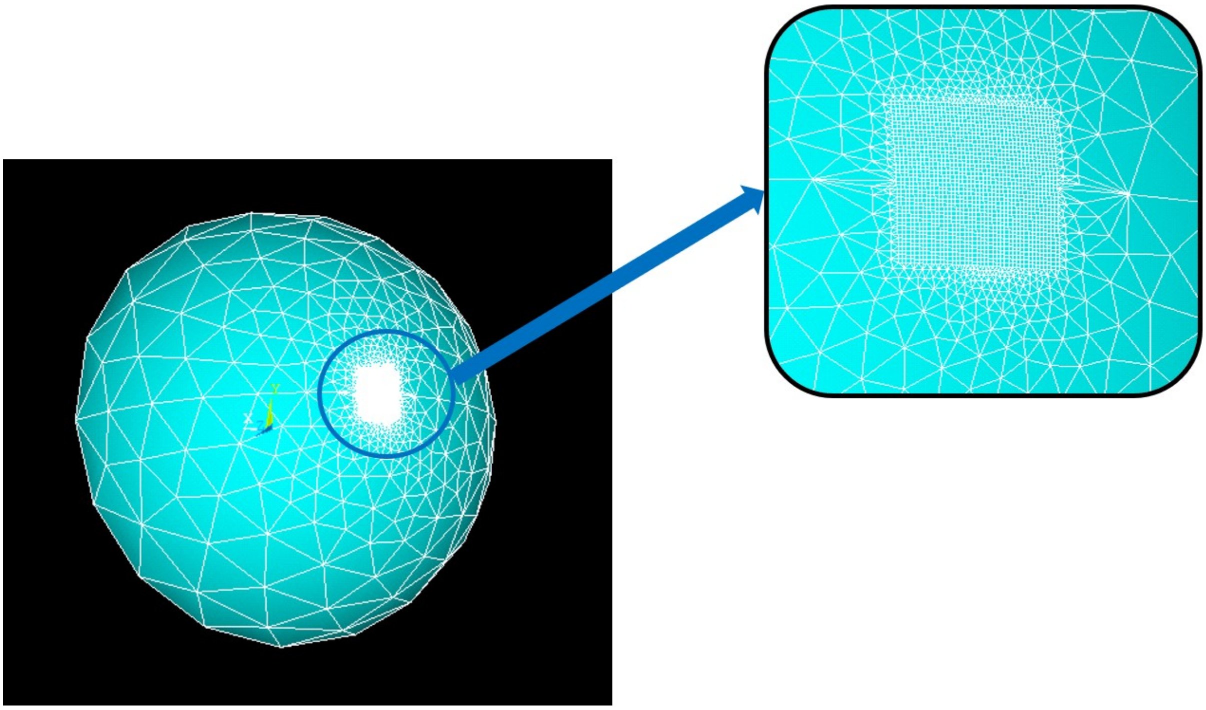

Figure 35: Meshed potential contact area on semisphere

Not only we had to pay attention to the mesh in the potential contact to be fine enough in order not to compromise the reliability of the results, but also to the mesh in the areas the distant nodes lay on, which are generally opposite to the contact area. Since those are the nodes

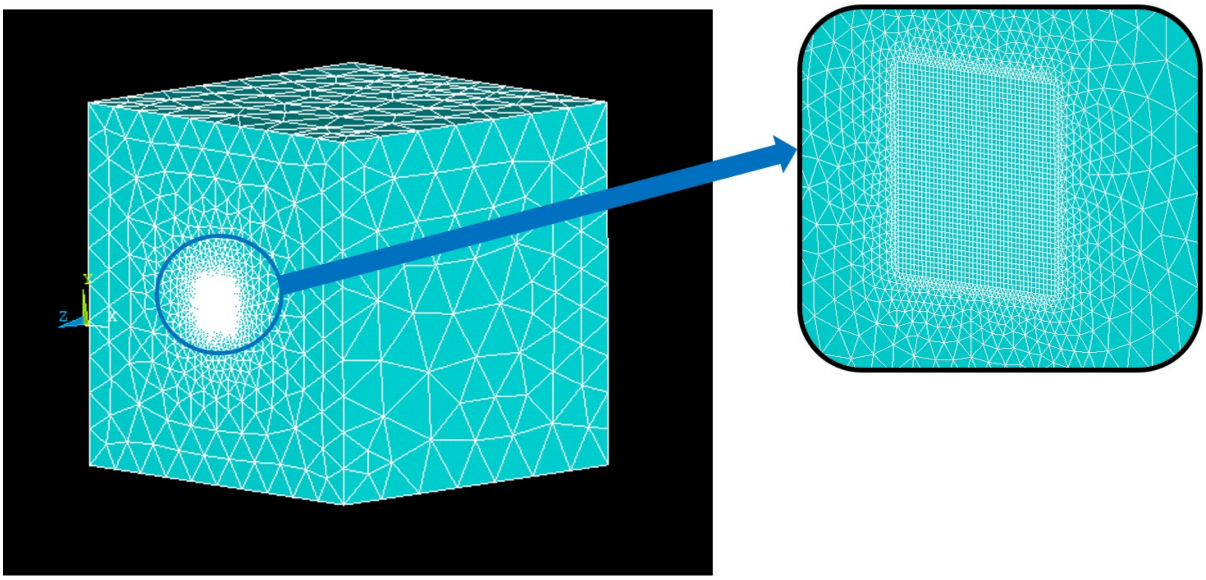

Figure 36: Meshed potential contact area on semiplane

on which the input displacements are applied, their distribution must follow the symmetry of the geometries in contact in order to avoid any potential unbalance. Therefore, the mesh on those areas must respect the geometry symmetry, if any is present. The distant nodes are shown in Figure 37.

6.2 Master nodes selection

For this case, the master node selection is straightforward: as contact nodes we took the 1681 nodes present in the potential contact area meshed in each body, while as distant nodes, the ones on the areas previously shown, which are opposite to it as shown in Figure 37.

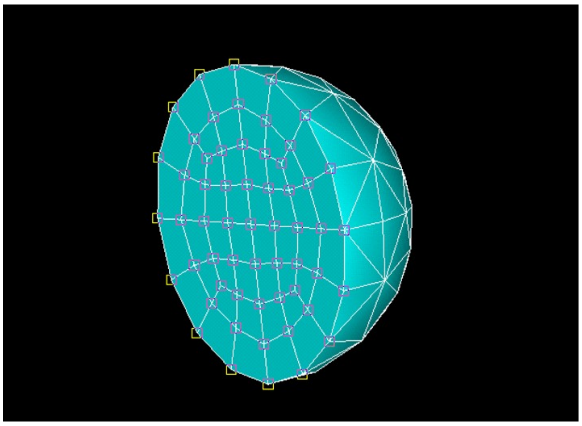

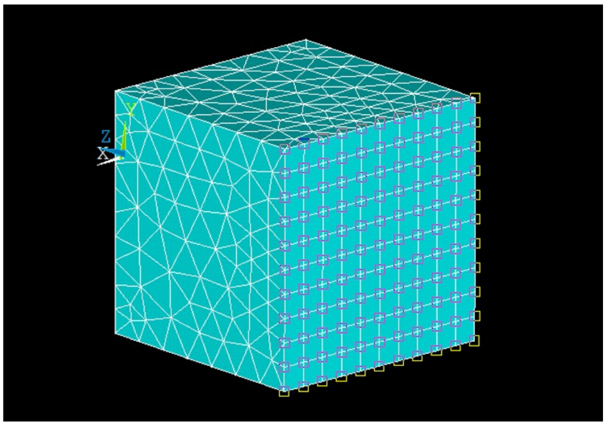

Figure 37: Distant nodes in the half-sphere and cube

6.3 Normal contact problem: comparison with Hertz analitical solution

6.3.1 Hertz contact theory

Hertz lied the basis of the contact mechanics theory back in 1881, providing analytical solution for well-defined geometries. The main assumptions of his theory can be summarized in the following

1. The two bodies in contact must have a common tangent plane, ensuring that the first derivative exist, and the contact point must be a non-singular point, ensuring the existence of the second derivative as well.
2. The material of the bodies in contact is elastic and isotropic.
3. The contact area is small with respect to the dimensions of the two bodies.
4. The contact between the bodies is frictionless.

The main input parameters used in the Hertz formulae are

- F is the normal force applied on the bodies, pressing them together.
- E_1 and E_2 are the elastic moduli of body 1 and body 2 respectively.
- v_1 and v_2 are the Poisson's ratio of body 1 and body 2.
- $\alpha_x, \alpha_y, \beta_x, \beta_y$ are the curvatures of body 1 and body 2 along the two principle directions X and Y.

The main formulae elaborated by Hertz allow calculating the radius of the contact area a and the vertical approach δ.

$$a = \sqrt[3]{\frac{3}{4}\frac{FR}{4}(\frac{(1-v_1^2)}{E_1}+\frac{(1-v_2^2)}{E_2})} \tag{6.1}$$

$$\delta = (\alpha_x + \alpha_y + \beta_x + \beta_y)\Big(\sqrt[3]{\frac{3}{2}\frac{F}{2}(\frac{(1-v_1^2)}{E_1}+\frac{(1-v_2^2)}{E_2})}\Big)^2 \tag{6.2}$$

While the pressure distribution within the contact area is described by

$$p = \frac{3}{2}\frac{F}{\pi a^2}\sqrt{1-\frac{X^2}{a^2}-\frac{Y^2}{a^2}} \qquad X, Y \leq a \tag{6.3}$$

6.3.2 Results comparison

We will consider two different normal forces, $F_N = 50N$ and $F_N = 200N$, in order to perform the comparison of the results obtained with the numerical method and the solution

TABLE VII: COMPARISON: NUMERICAL VS HERTZ RESULTS FOR F = 50 N

	Numerical method	Hertz formulae	Difference
Contact area radius [μm]	1.17 10^2	1.19 10^2	-1.6 %
Approach [μm]	2.73	2.85	-4.2%
Contact area [μm^2]	4.31 10^4	4.48 10^4	-3.7%
Maximum pressure [MPa]	1.80 10^3	1.70 10^3	+5.8%
Mean pressure [MPa]	1.16 10^3	1.15 10^3	+0.8 %

TABLE VIII: COMPARISON: NUMERICAL VS HERTZ RESULTS FOR F = 200 N

	Numerical method	Hertz formulae	Difference
Contact area radius [μm]	1.89 10^2	1.89 10^2	0%
Approach [μm]	6.98	7.16	-2.5%
Contact area [μm^2]	1.131 10^5	1.130 10^5	+0.09%
Maximum pressure [MPa]	2.93 10^3	2.65 10^3	+9.0 %
Mean pressure [MPa]	1.767 10^3	1.769 10^3	-0.11 %

got using the Hertz theory. In Table VII and Table VIII we have the results for the above mentioned normal forces.

In Figure 38 we have a visual comparison, for different F_N, with the analytical solution proposed by Hertz. We can easily see how all the nodes evaluated to be inside the contact area by the numerical method, are within the area predicted by the Hertz theory.

As far as the pressure distribution is concerned, in Figure 39, it is represented along the z-axis. It is worth noticing that, even though the number of elements in the area is not high, the distribution is smooth all over it.

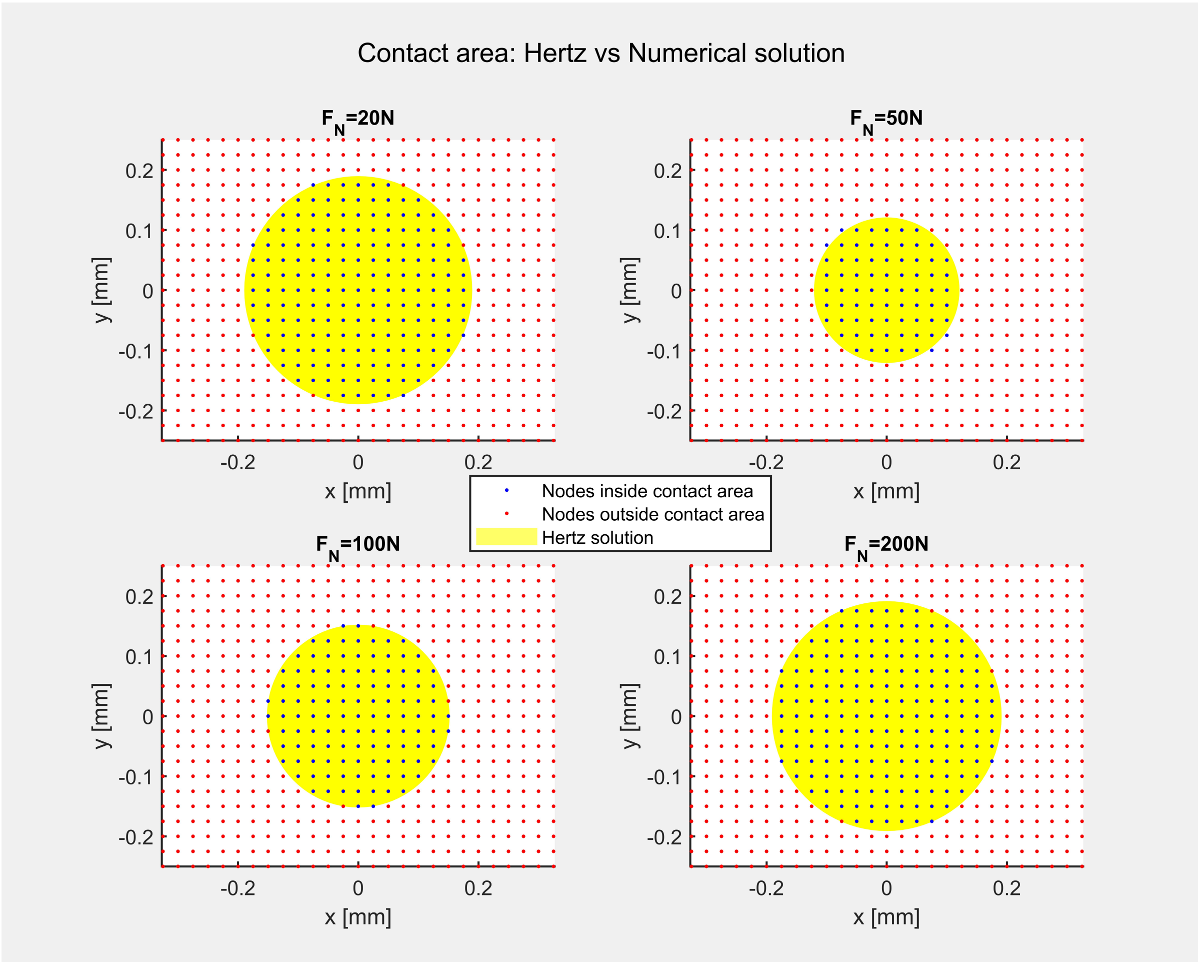

Figure 38: Contact area: Numerical method vs Hertz

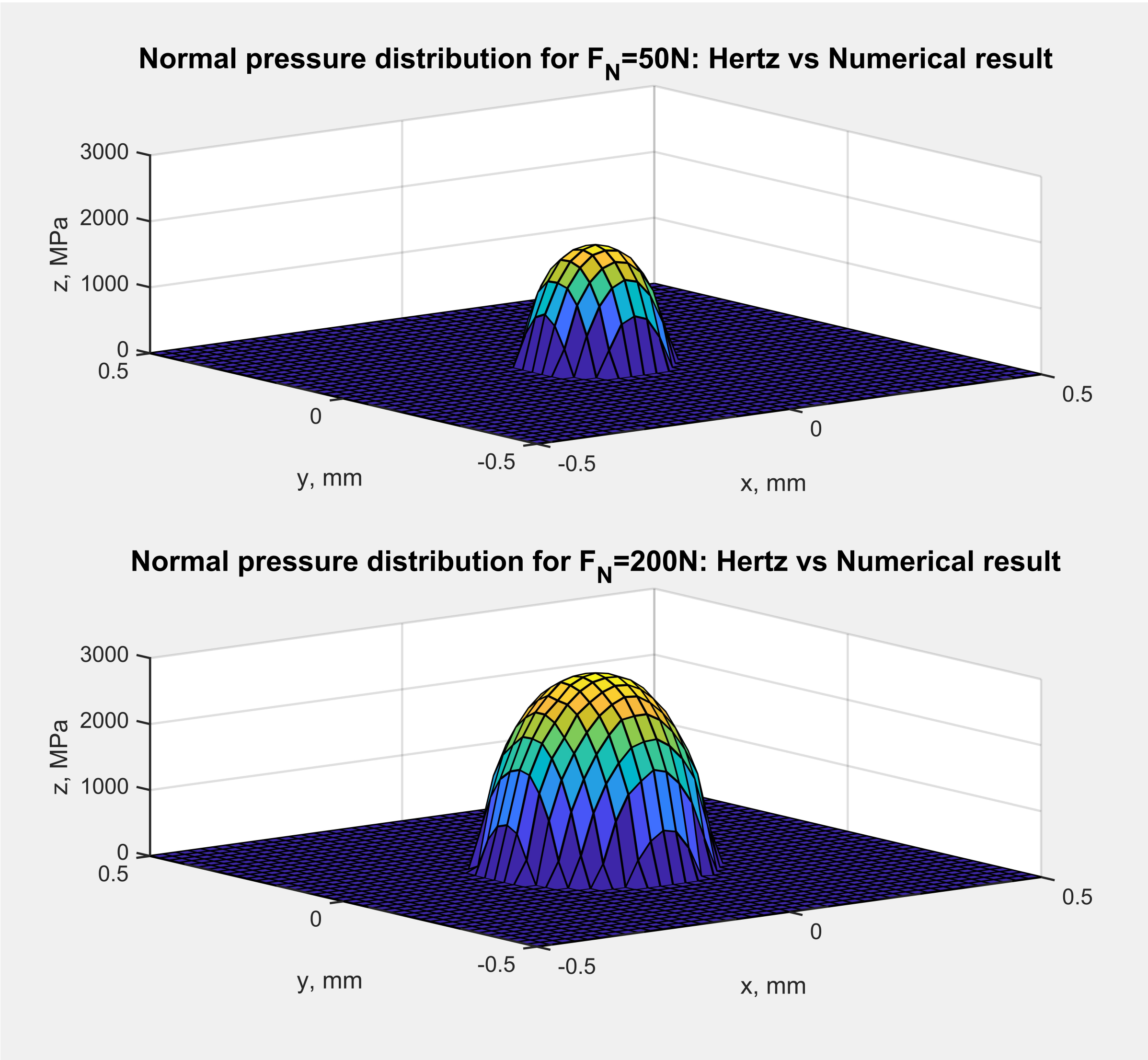

Figure 39: Pressure distribution for $F_N = 50N$ and $F_N = 200N$

An immediate comparison with the pressure distribution calculated with the Hertz formulae is presented in Figure 40. We can notice how, getting closer to the contact area centre, the pressure obtained with the numerical method eventually overcomes the analytical solution.

We can now consider three different cross sections, one passing through the centre and two at an equal distance from it, in order to evaluate the difference in the pressure distribution.

Finally, it is possible to perform a comparison over a wider range of applied F_N, as shown in Figure 43 and Figure 44, both for the contact area and the maximum pressure.

Considering the following steps, the most important comparison is the one related to the F_N - δ relation, as shown in Figure 45, since it defines the normal stiffness.

6.4 Tangential problem: numerical method vs. Midlin solution

6.4.1 Midlin contact model

While Hertz theory comes to help when dealing with the normal contact problem, the Mindlin[4][5] theory is needed in order to carry out a comparison for the tangential contact problem. It can be considered an expansion of the Hertz theory, adding the tangential load to the bodies in contact and considering the slip in contact area. The main assumptions of the Midlin theory are summarized in the following

- The contact area and the pressure distribution over it remain unchanged, as a result of the normal load, while the tangential load is applied.
- The two bodies in contact are perfectly elastic.
- The shear stress in a point in slip condition is equal to $\tau = \mu$f where f is the local applied force in the node.

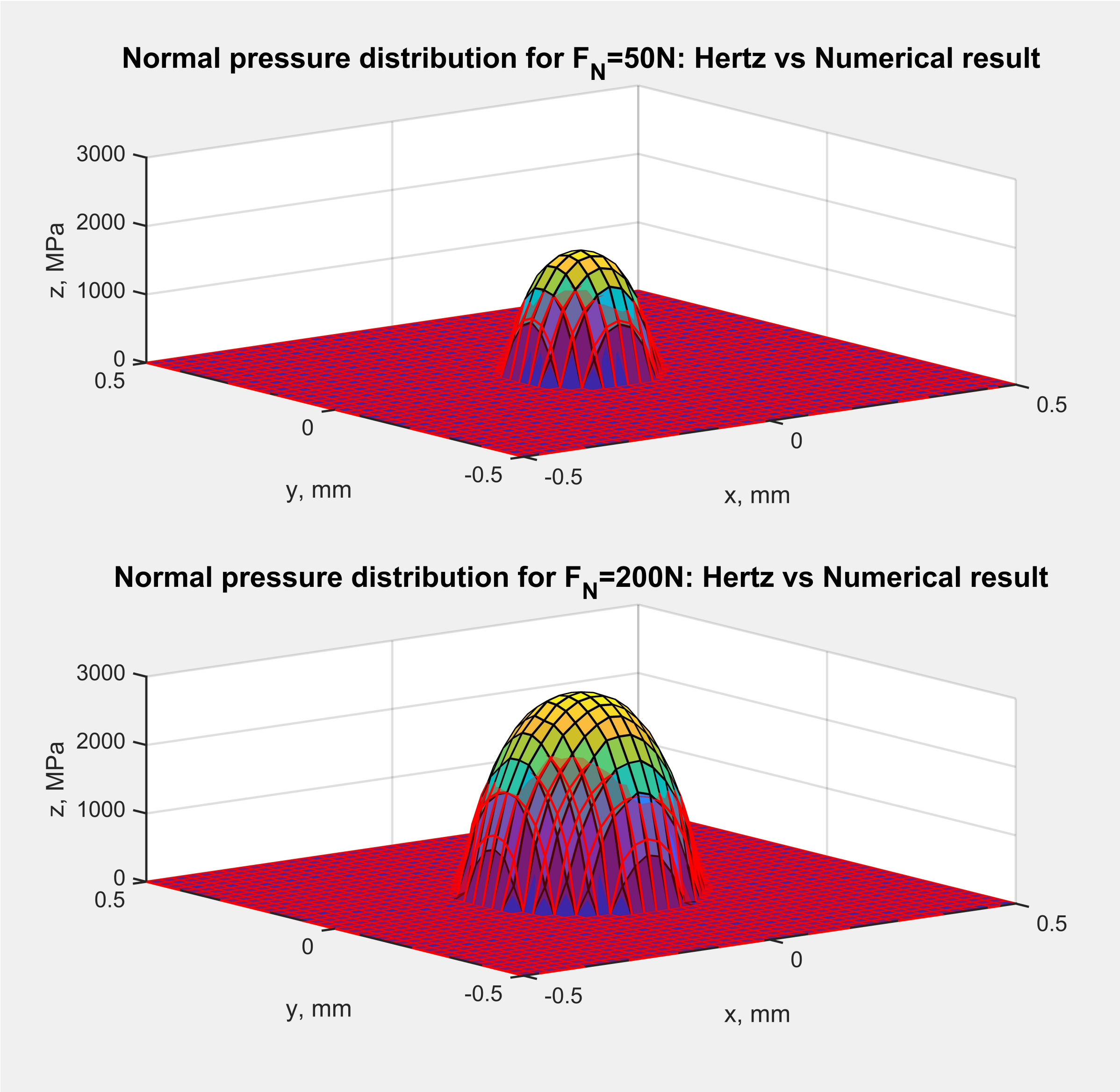

Figure 40: Pressure distribution: comparison with Hertz solution for $F_N = 50N$ and $F_N = 200N$

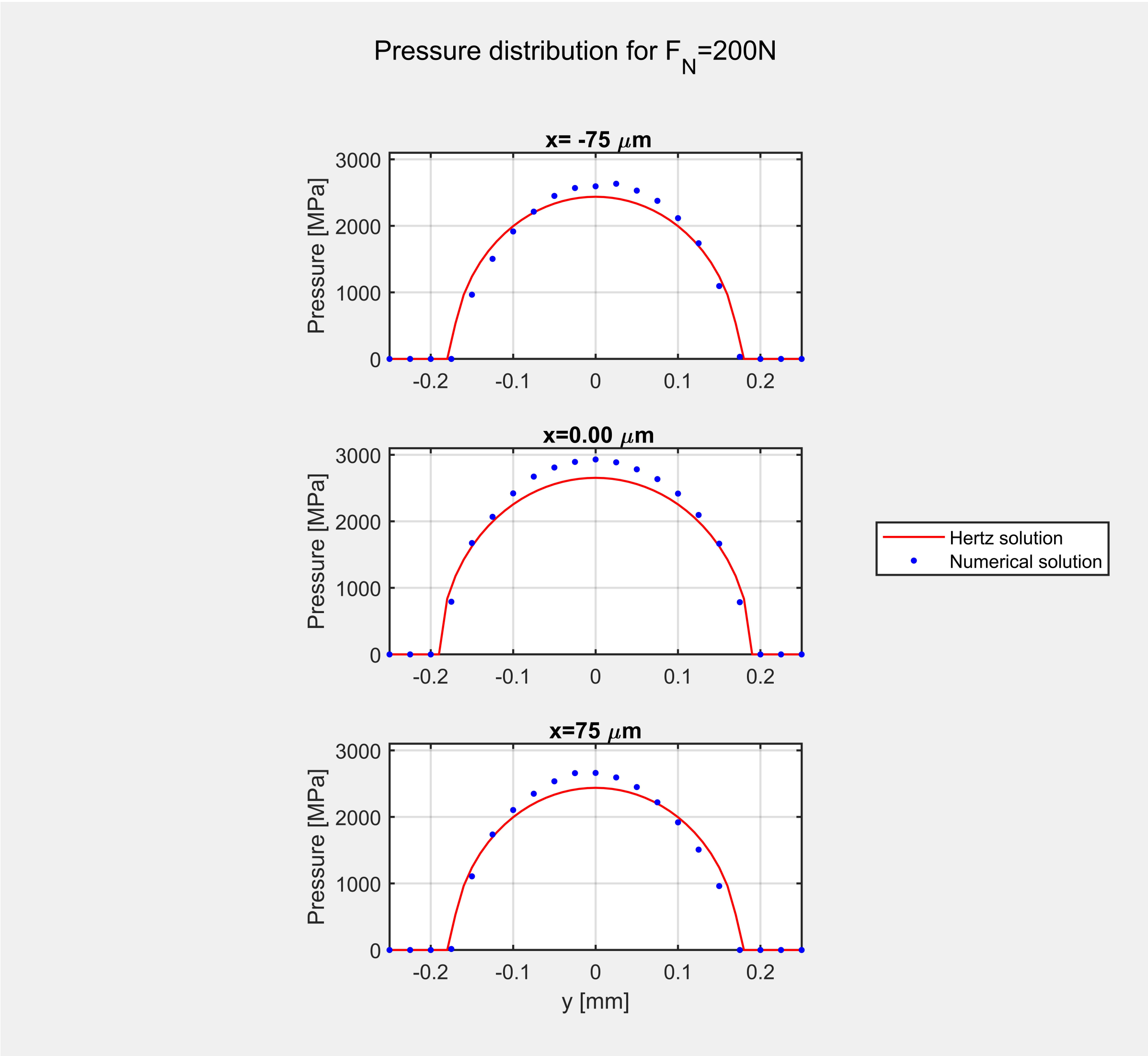

Figure 41: Pressure distribution at different cross sections for $F_N = 200N$

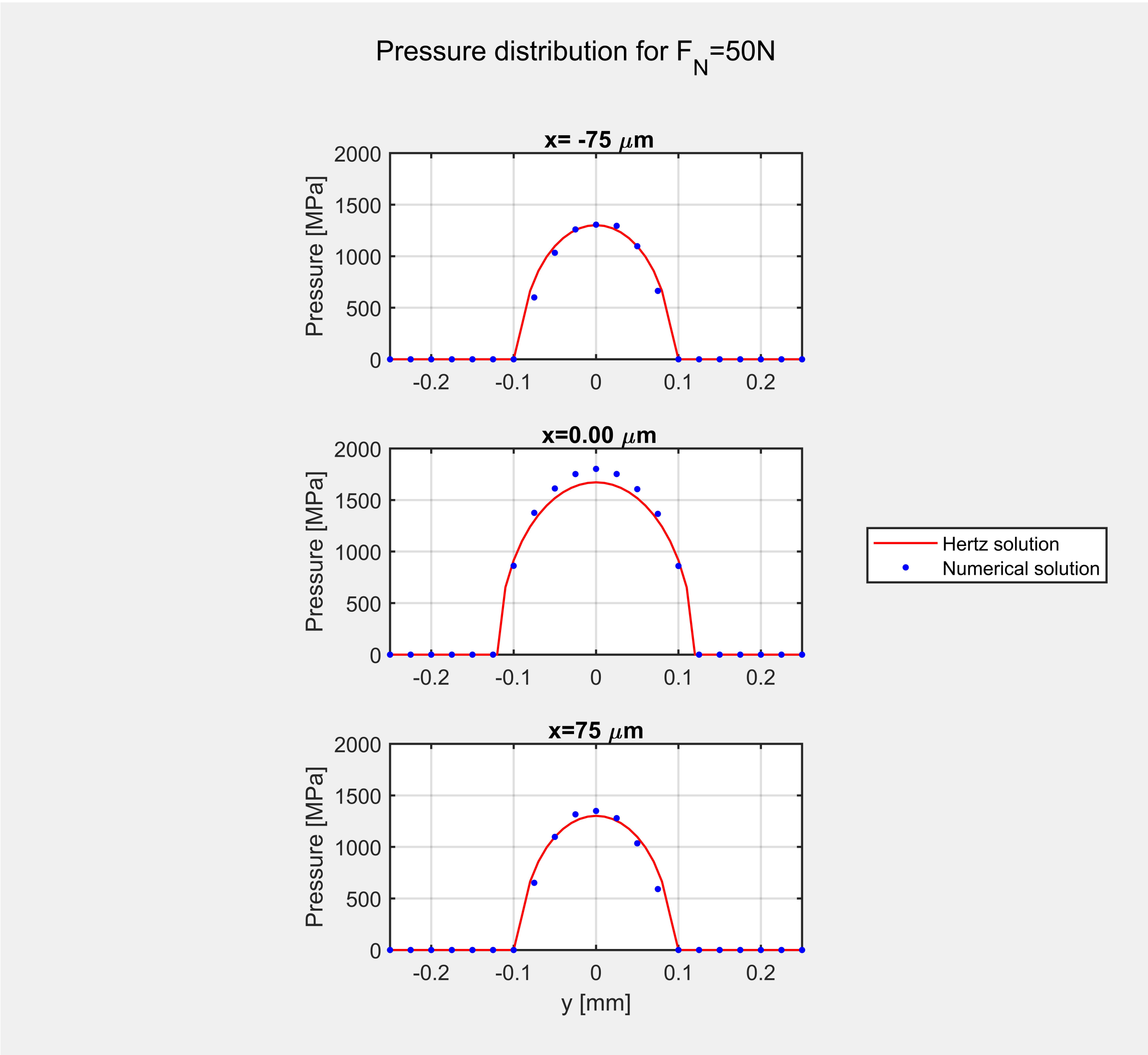

Figure 42: Pressure distribution at different cross sections for $F_N = 50N$

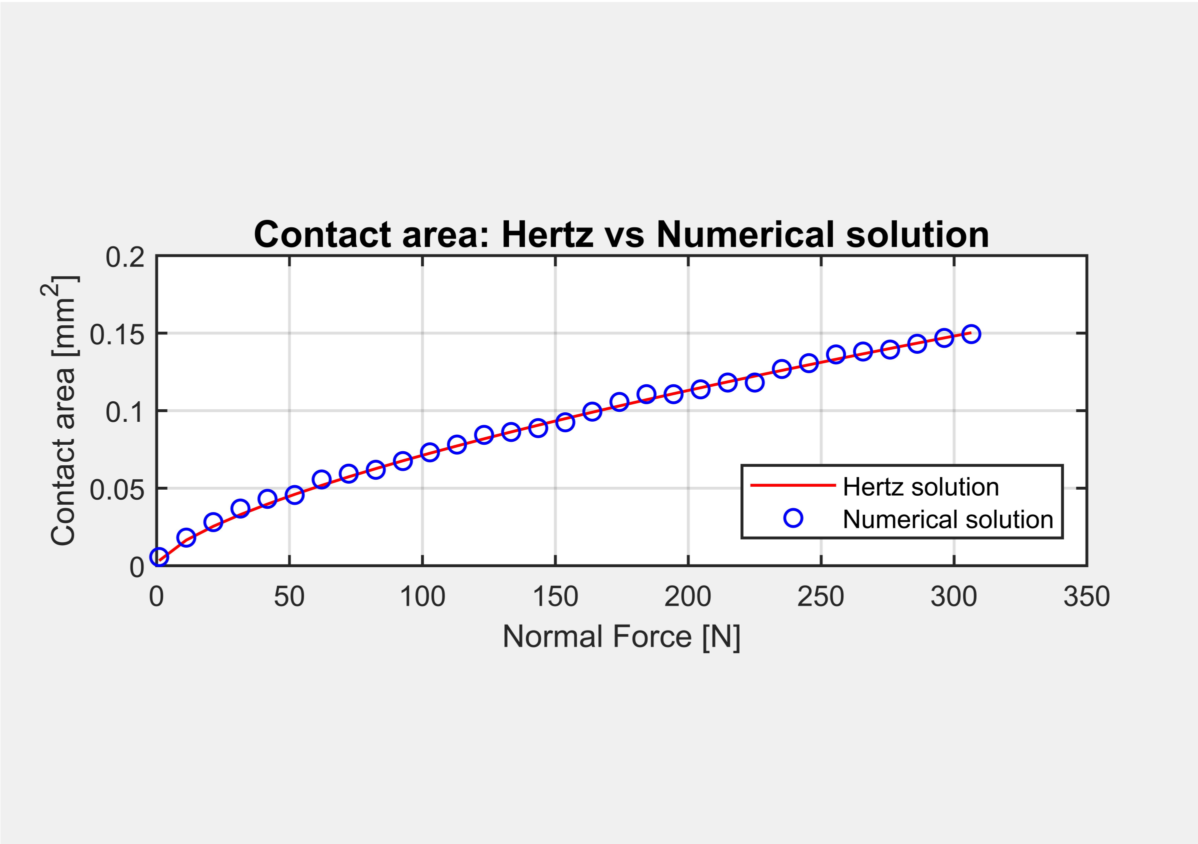

Figure 43: Contact area comparison: Numerical method vs Hertz

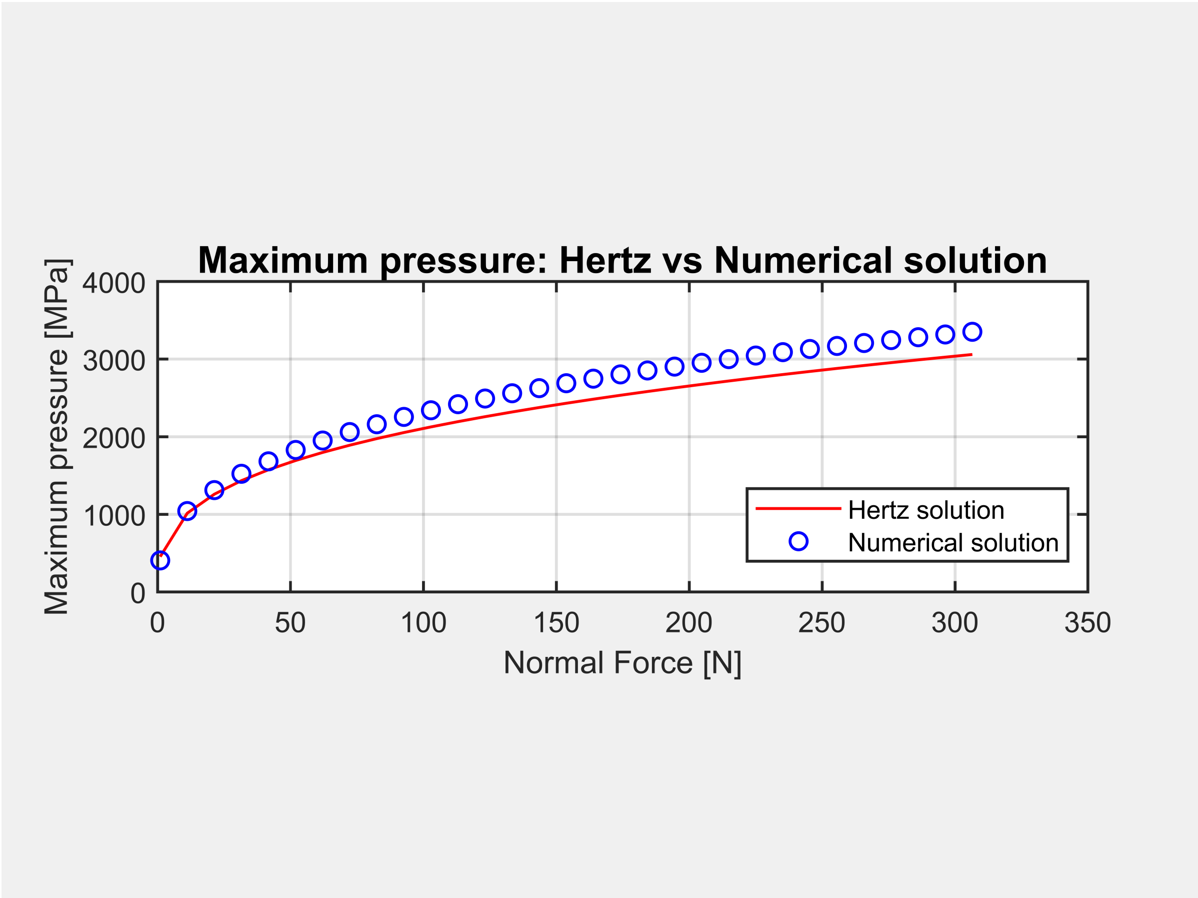

Figure 44: Maximum pressure: Numerical method vs Hertz

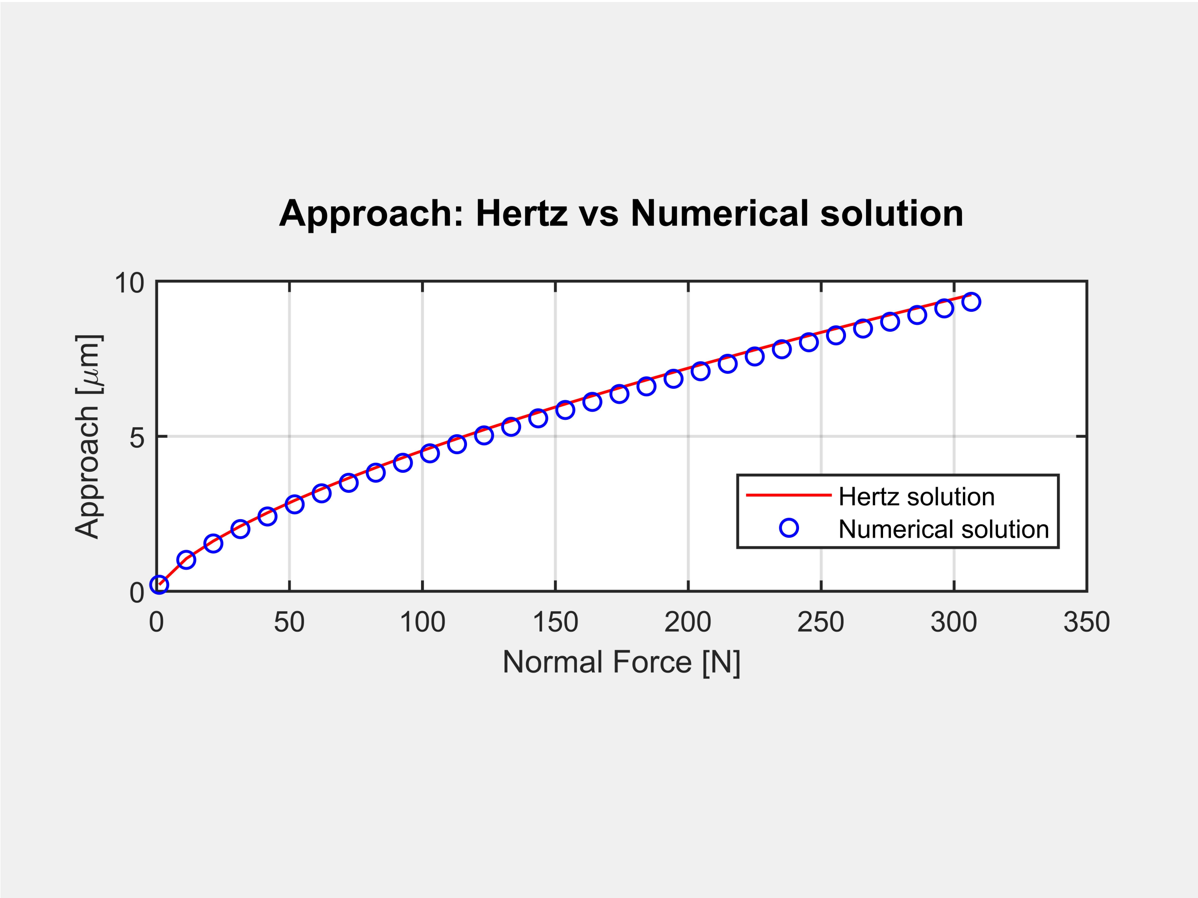

Figure 45: Force-approach: Numerical method vs Hertz

The main formulae developed by Mindlin allow us calculating the radius of the area defining the stick condition region, within the contact area previously found when solving the normal contact problem, the tangential stress distribution and the tangential displacement with respect to the points in adhesive condition. They are all reported in the following

$$c = a\sqrt[3]{1 - \frac{T}{\mu N}} \tag{6.4}$$

in which

- a is the radius of the contact area as defined in the Hertz theory when a normal force N is applied
- T is the applied tangential force
- N is the applied normal force
- μ is the friction coefficient

$$\begin{cases} \tau = \frac{3\mu N}{2\pi a^3}\sqrt{a^2 - r^2} & for c < r \leq a \\ \tau = \frac{3\mu N}{2\pi a^3}\left[\sqrt{a^2 - r^2} - \sqrt{c^2 - r^2}\right] & r \leq c \end{cases} \tag{6.5}$$

in which

- r is the distance of the point from the centre of the contact area

$$\delta = \frac{3(2 - v)\mu N}{16Ga}\left[1 - \left(\frac{c}{a}\right)^2\right] \tag{6.6}$$

where

- v is the Poisson's coefficient
- G is the shear modulus, which for elastic and isotropic materials is directly related to the elastic modulus according to $\frac{E}{1-2v}$

6.4.2 Comparison with Midlin model results

In order to perform the comparison we will consider the normal forces already used for the normal contact problem, F_N=50N and F_N=200N, and for each of them we will apply four different tangential forces F_T.

A first comparison can be performed for the results regarding the definition of the area within which we have an adhesion condition. In Figure 46 and Figure 47 we have an overview of the contact areas for different combinations of F_N and F_T values.

Besides the adhesion area, we can compare the distribution of the traction tangential force as well. In Figure 48 we have along the z-axis the tangential force distribution as obtained with the numerical method, compared with the analytical solution according to Mindlin theory.

6.5 Body compression influence on approach and normal contact stiffness

As far as the normal contact stiffness is concerned, it is worth pointing out that if we are to consider the F_N - δ relation shown in Figure 45 in order to calculate it, we would commit a mistake, even if it could be small: the δ is the vertical displacement applied at the distant nodes, but besides the compression due to the contact, there is a compression of both bodies as well. The concept will be clearer in Figure 49.

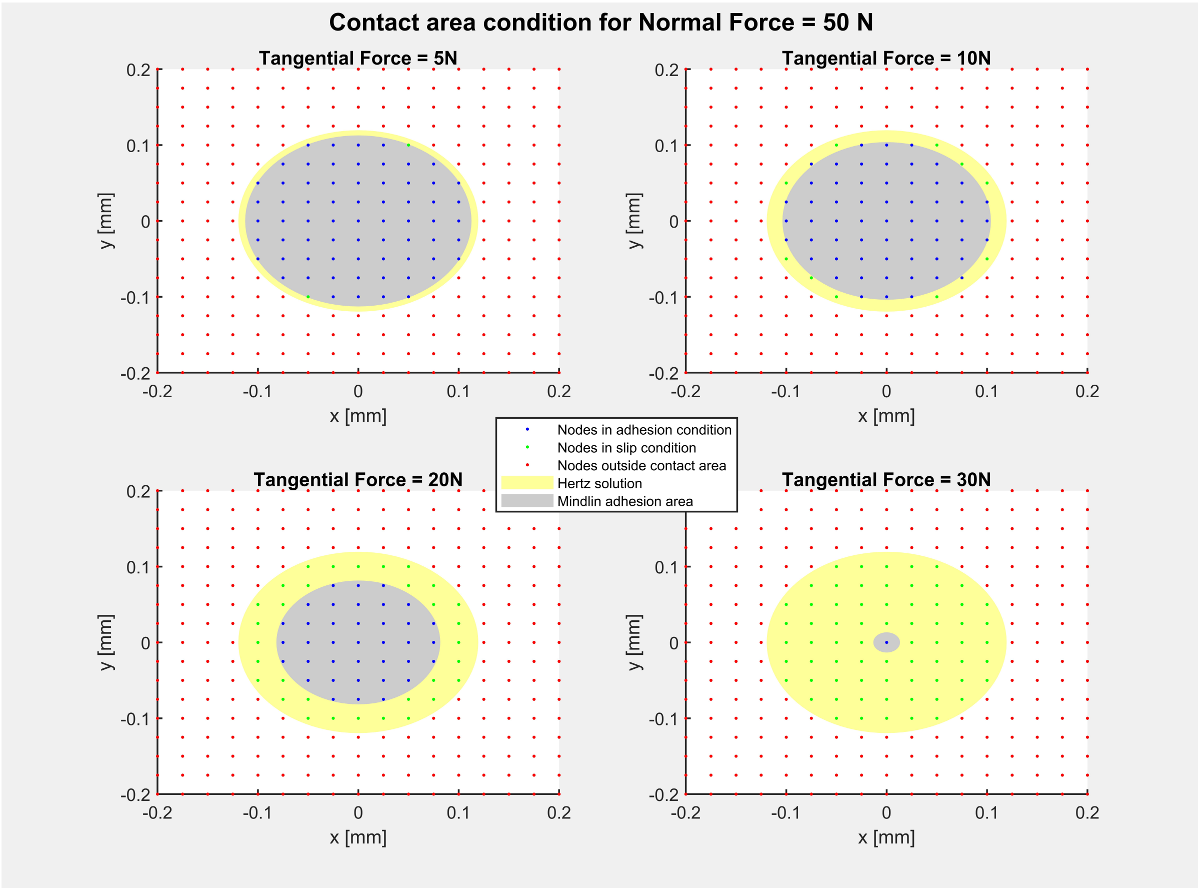

Figure 46: Contact area for F_T at F_N=50N

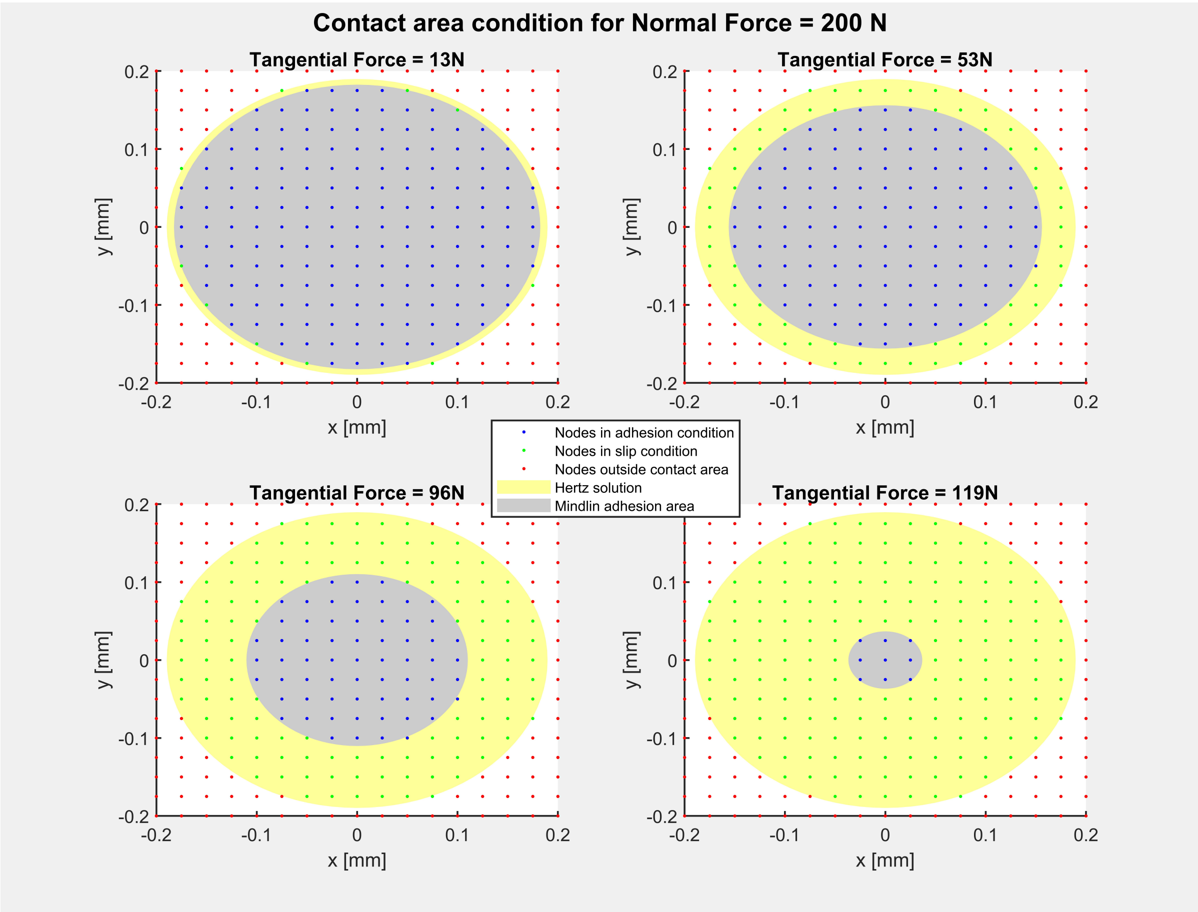

Figure 47: Contact area for F_T at F_N=200N

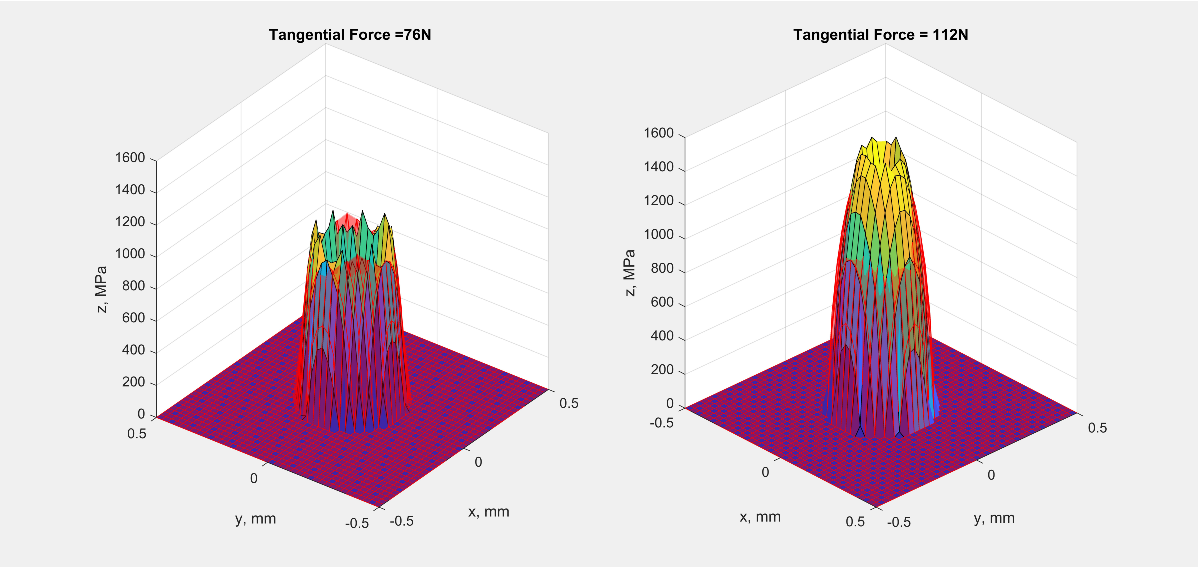

Figure 48: Tangential traction distribution comparison for $F_N = 200$: Numerical method vs Midlin

Therefore, in order to have a more accurate normal contact stiffness, we need to go more into the detail of the bodies compression phenomena, and evaluate its overall influence on the stiffness calculation. In order to have the amount of compression of each body, we can consider the vertical displacement of a node at a distance 3a, where the effect of the contact deformation is null. Since the whole relative displacement is equal to the approach of the sphere since the block is motionless, we can get the amount of compression of a single body by a simple difference

$$\phi_i = \delta_i - \delta_{3ai} \tag{6.7}$$

where

Figure 49: Displacement of bodies in contact

- δ_i is the vertical displacement of the distant nodes of body i
- δ_{3bi} is the vertical displacement at a point at distance 3b from the contact area in body i
- ϕ_i is the compression of body i

Therefore, considering that the block is still, the actual approach obtained after getting rid of the compressibility effect will be simply

$$\delta_{effective} = \phi_1 - \phi_2 \tag{6.8}$$

In Figure 50 we have the percentage of the body compression with respect to the vertical approach at the distant nodes of the half-sphere.

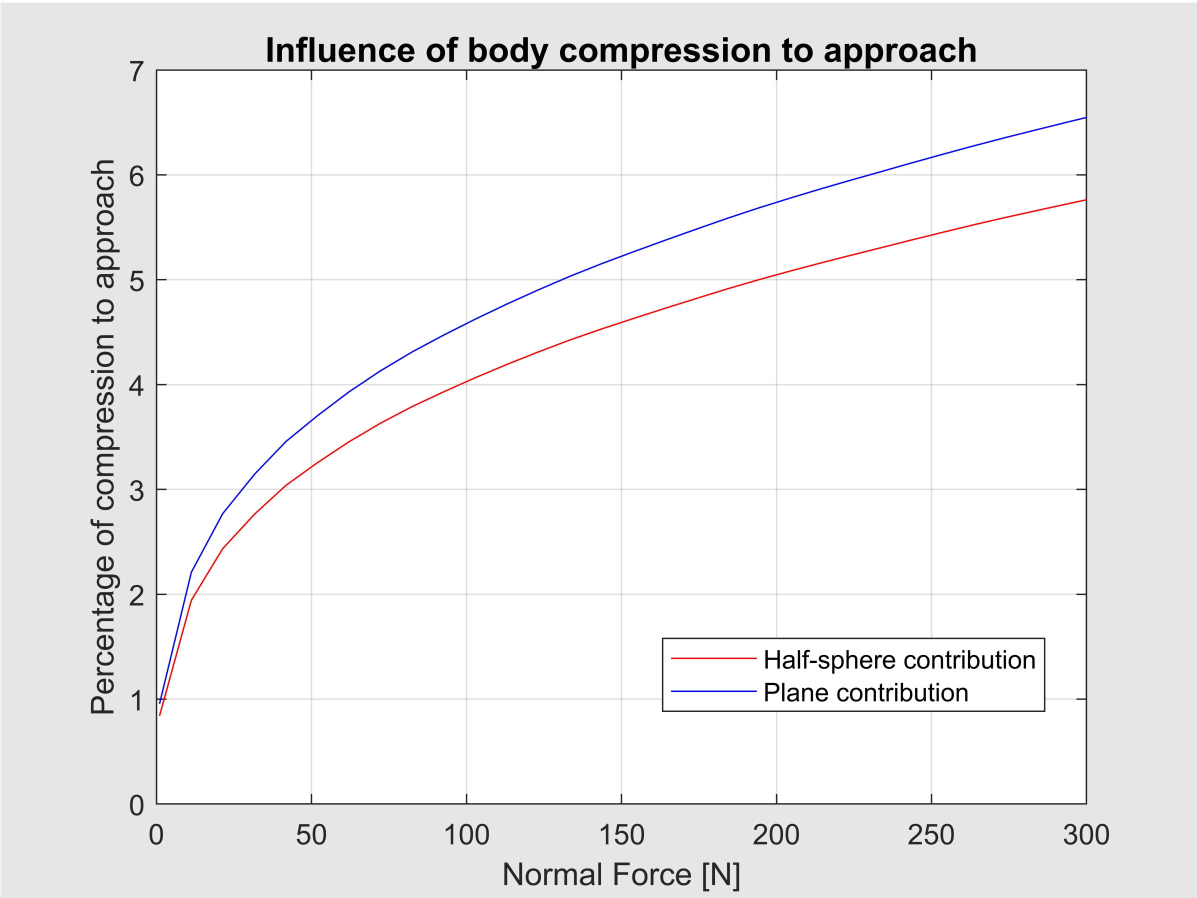

Figure 50: Influence of the body compression on approach

TABLE IX: BODY COMPRESSION EFFECT ON APPROACH

F_N	Theoretical Approach [μm]	Corrected Approach[μm]	Difference [%]
50N	2.80	2.60	-7.14
200N	7.09	6.50	-8.32

TABLE X: BODY COMPRESSION EFFECT ON NORMAL STIFFNESS

F_N	With theoretical approach [μm]	With corrected Approach[μm]	Difference [%]
50N	$2.8\ 10^4$	$3.3\ 10^4$	+15 %
200N	$7.09\ 10^4$	$6.50\ 10^4$	+8.32%

In Table IX, we have the main values of the above mentioned parameters for $F_N = 50N$ and $F_N = 200N$, and the difference in percentage between the corrected approach and the applied one at the distance nodes

Finally, we can calculate the normal K_N in order to quantify the final influence of the compression on the stiffness value.

CHAPTER 7

PLANE-PLANE CONTACT: SYMMETRIC DAMPER

7.1 FE model in Ansys

The model for the plane-plane contact is made up of the symmetric damper and a cube simulating the presence of the blade's underplatform. The dimensions, distances and offsets are exactly like the ones of the full model and the experiments. Therefore, the found results are immediately available for comparison. In Ansys APDL the properties MESH200 for the mesh and SOLID185 for the element definition were used. The latter one ensures elements defined by eight nodes, each of them having three DOFs. In Figure 51 we have the FE model in Ansys APDL along with a sketch showing the main dimensions involved.

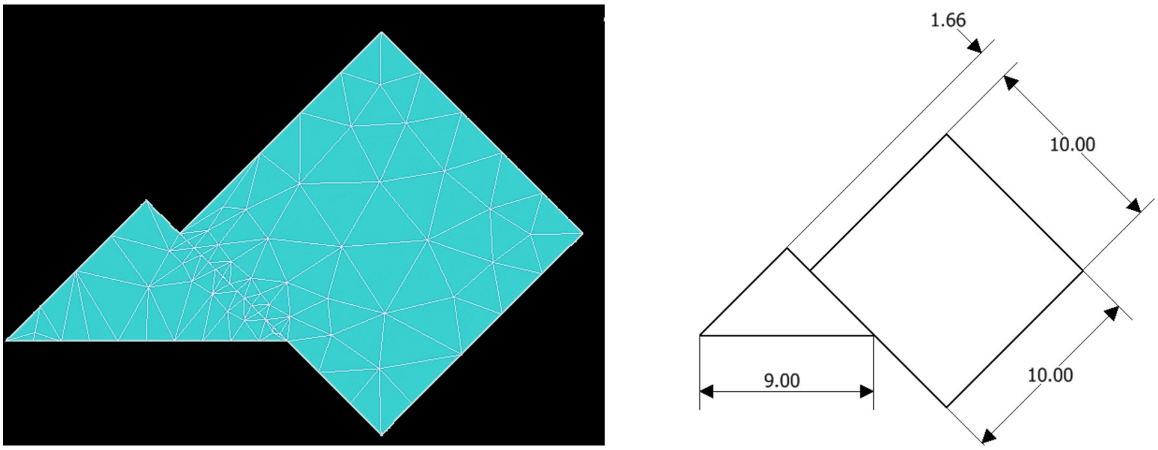

Figure 51: Sketch with main dimensions of the symmetric damper-block model

It is worth paying attention to the reference system, which is on the left bottom corner of the contact area on the damper. The x-axes is along the longer edge, while the y-axes is along the shorter edge. The z-axes instead is consequently defined, positive going from the plane surface towards the damper. Knowledge of the reference system will allow an easier interpretation and localization of the regions in the plots present in the subsequent sections.

7.2 Applied forces

Since in the end we want to have a comparison of the results obtained by using the numerical method with the data available from experiments, we need to try recreating in this model the forces acting on the damper during the experiments. Since in the numerical method the normal contact problem and the tangential contact problem are uncoupled, we need to know the F_N and F_T acting at the interface between the damper and one of the underplatforms only. The centrifugal force is vertically directed, while in each of the two contact areas we have one F_N and F_T acting.

If we assume that there are no any unbalances and that the F_T stays right below the maximum value μF_N as set by the Coulomb friction theory, which is reasonable in this case since we are interested in a stick condition, we have the following equilibrium equation, in which α is the angle between the F_c and the vector normal to the contact area

$$F_C = 2(F_N cos(\alpha) + \mu F_N sin(\alpha)) \tag{7.1}$$

where the normal contribution comes from the contact with one blade, while the tangential one comes from the contact with the other one. In the experiment we had F_c equal to 350N, therefore we obtain F_N=155N, which will be consider from now on. s

7.3 Master nodes selection

The potential contact is divided into 3442 square elements, as it is shown in Figure 52 and the 453 nodes inside it are chosen as contact nodes for the damper. Since the mesh is exactly the same on the block's surface and the potential contact on both bodies are already in contact, the same nodes are chosen as contact nodes for the block as well.

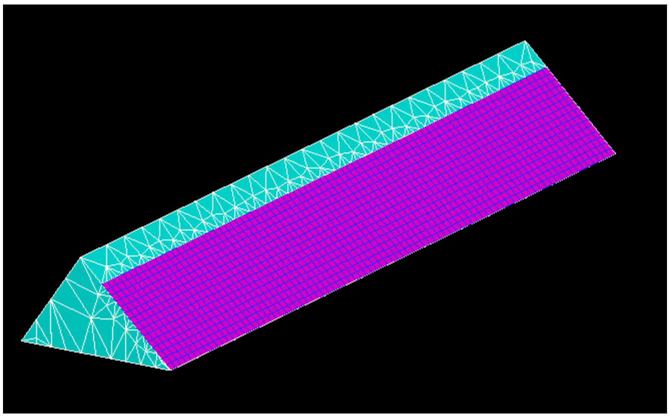

Figure 52: Meshed contact area

As far as the distant nodes are concerned, for the damper we needed to carefully think about how to choose them. The problem is that in the experiments the application points of the forces pulling the damper upwards are at the top edge, but since the wires are passing through the barycentre, we can think them as actually being applied in it. But, they are applied at the extreme sides of the damper's length. Placing the distant nodes in the projection just below where the wires were attached to, would have created a concentrated pressure on their normal projection on the contact area, which would have been in clear disagreement with the worn areas we can see on the damper surface. The fact that the worn areas are not located below the wires direction may be due to the fact that pulling upwards at the two extremes of the damper, the wires cause it to bend leading to a slip condition at the nodes at the extreme edges. Therefore, the idea was to place and spread the distant nodes at bottom surface, but on the direction of the worn areas instead as shown in Figure 53.

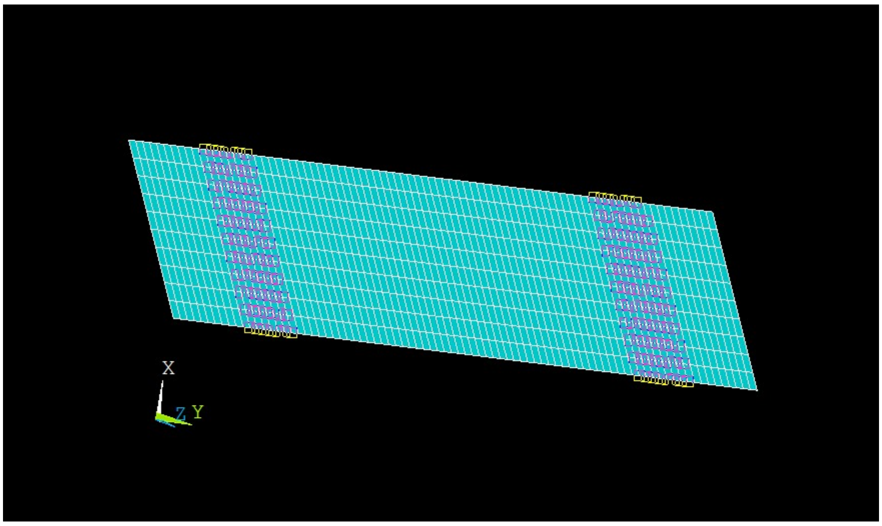

Figure 53: Distant nodes selection for the damper

For the block, instead, the chosen distant nodes were the ones inside the face opposite the one of the contact area as shown Figure 54.

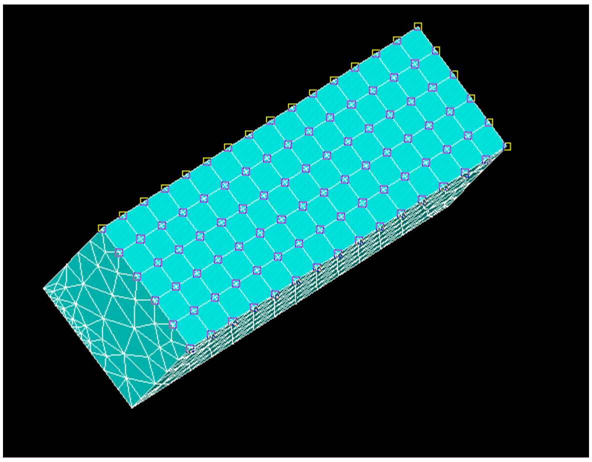

Figure 54: Distant nodes selection in block

7.4 Results of the normal contact problem

One of the main results of the normal contact problem is the pressure distribution over the contact surface, which is shown in Figure 55. Even though the damper's distant nodes were spread across the bottom width, we can easily notice a higher pressure in two spots in the lower part of the contact area, while it constantly decreases moving towards the upper-part.

In Figure 56 we have a plot of the damper's surface with the nodes divided according to whether they are inside and outside the contact area.

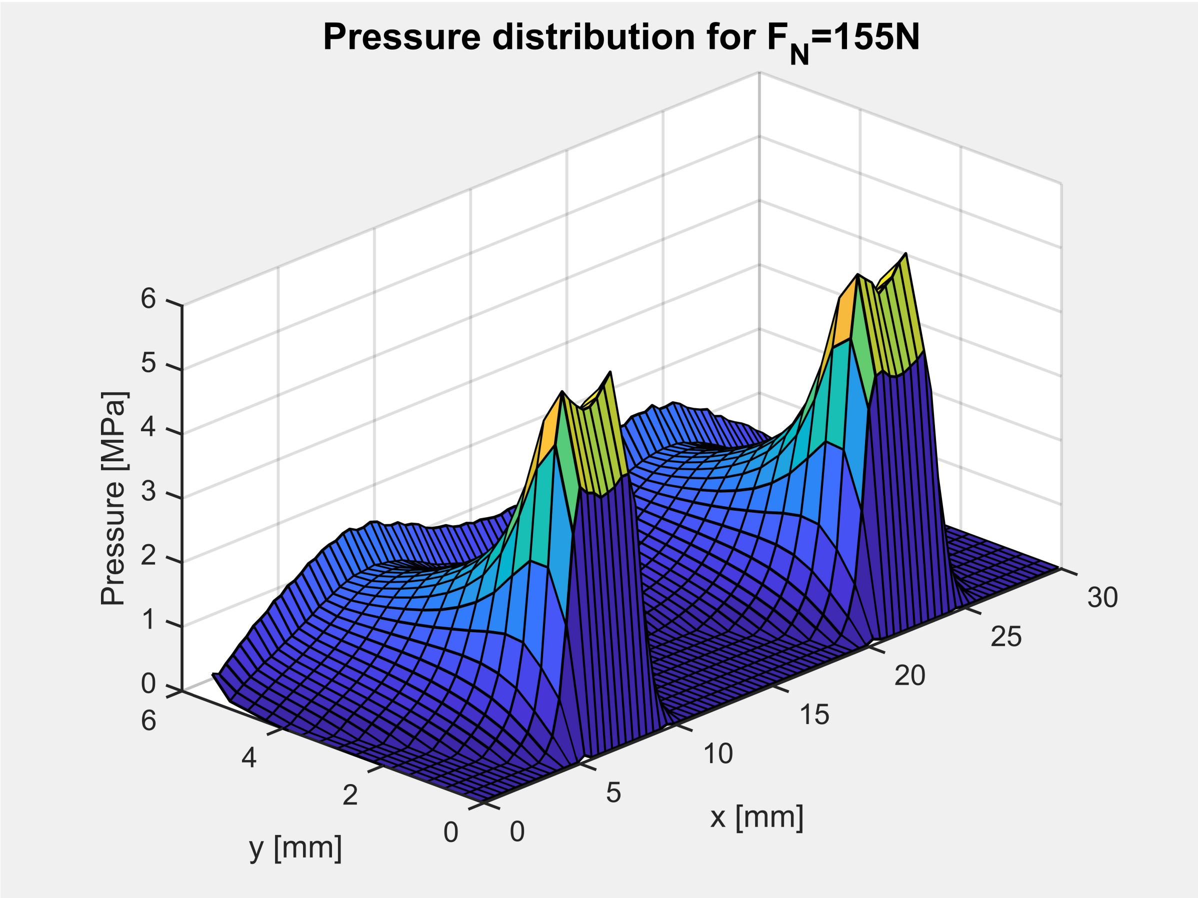

Figure 55: Pressure distribution over contact area

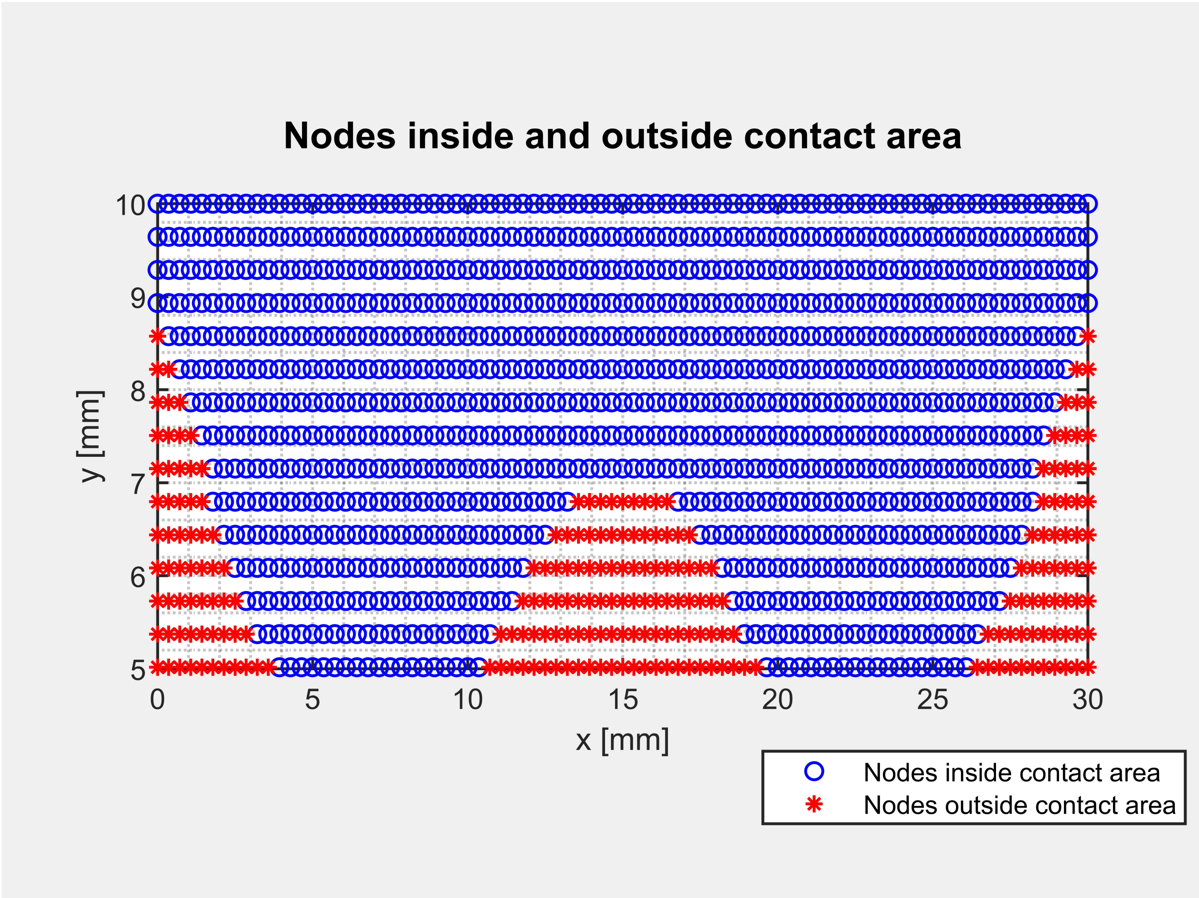

Figure 56: Nodes inside and outside contact area

It is also interesting to see the deformation of the contact surface of one of the two bodies. In Figure 57 we have the deformation of damper in the potential contact area.

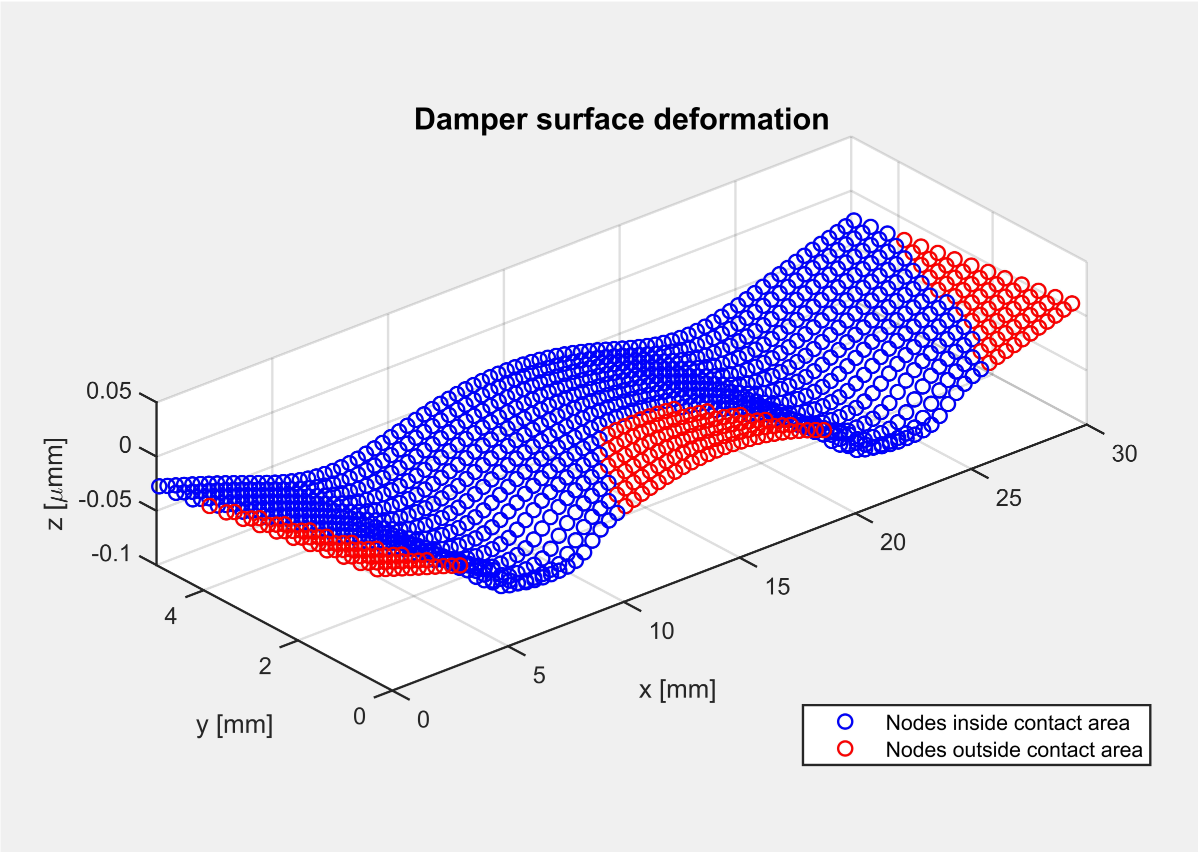

Figure 57: Deformation of the damper surface

It is also important to consider the maximum pressure and mean pressure as a function of the applied F_N.

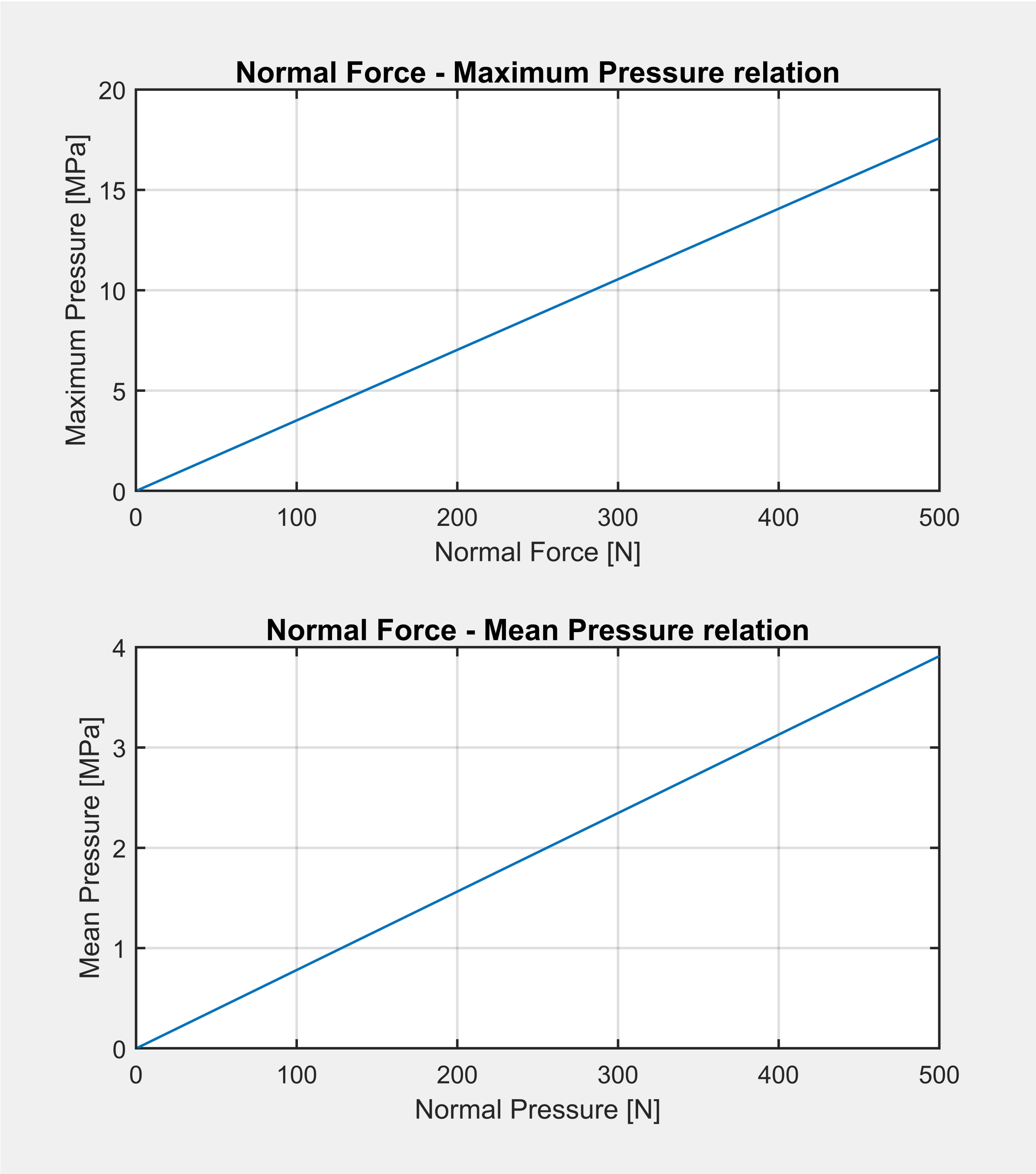

Figure 58: Maximum and mean pressure as a function of the applied normal force

The main result regards the F_N-δ relation, which is shown in Figure 59.

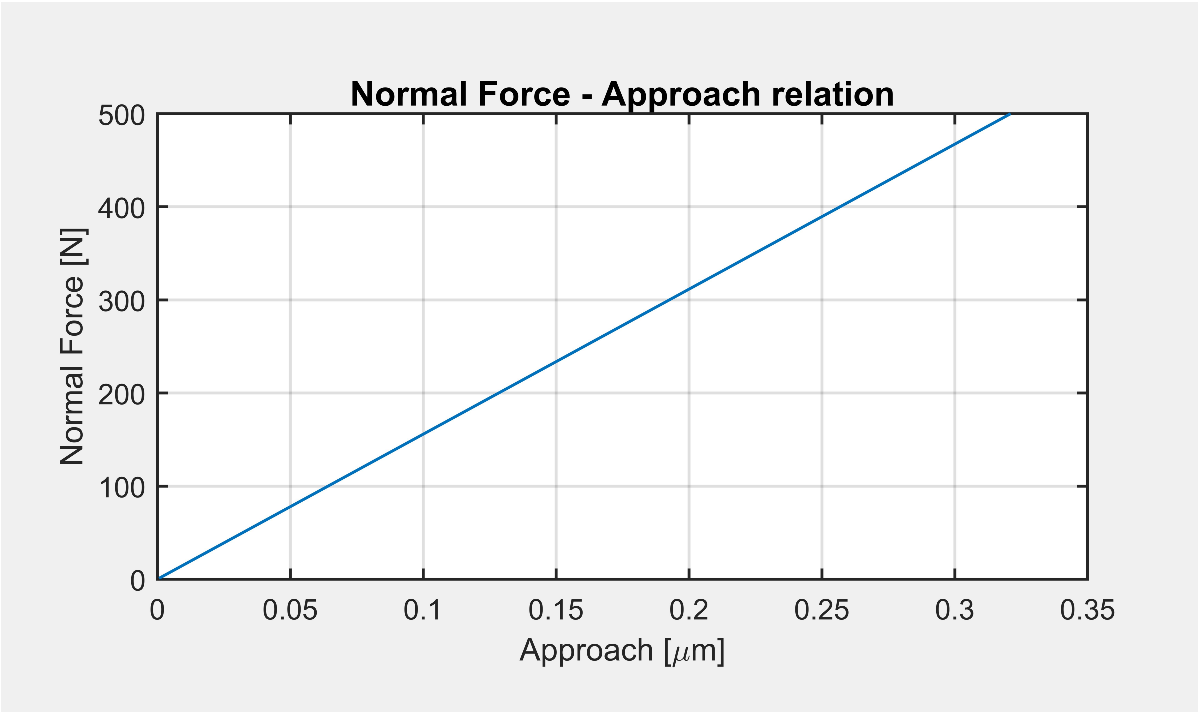

Figure 59: Normal force - Approach relation

7.5 Results of the tangential contact problem

As an output from the tangential contact problem, we have an identification of the nodes in adhesion and in slip condition inside the contact area. In Figure 60 we consider to have a normal pressure $F_N = 155N$ and different tangential forces applied in order to see how the contact evolves.

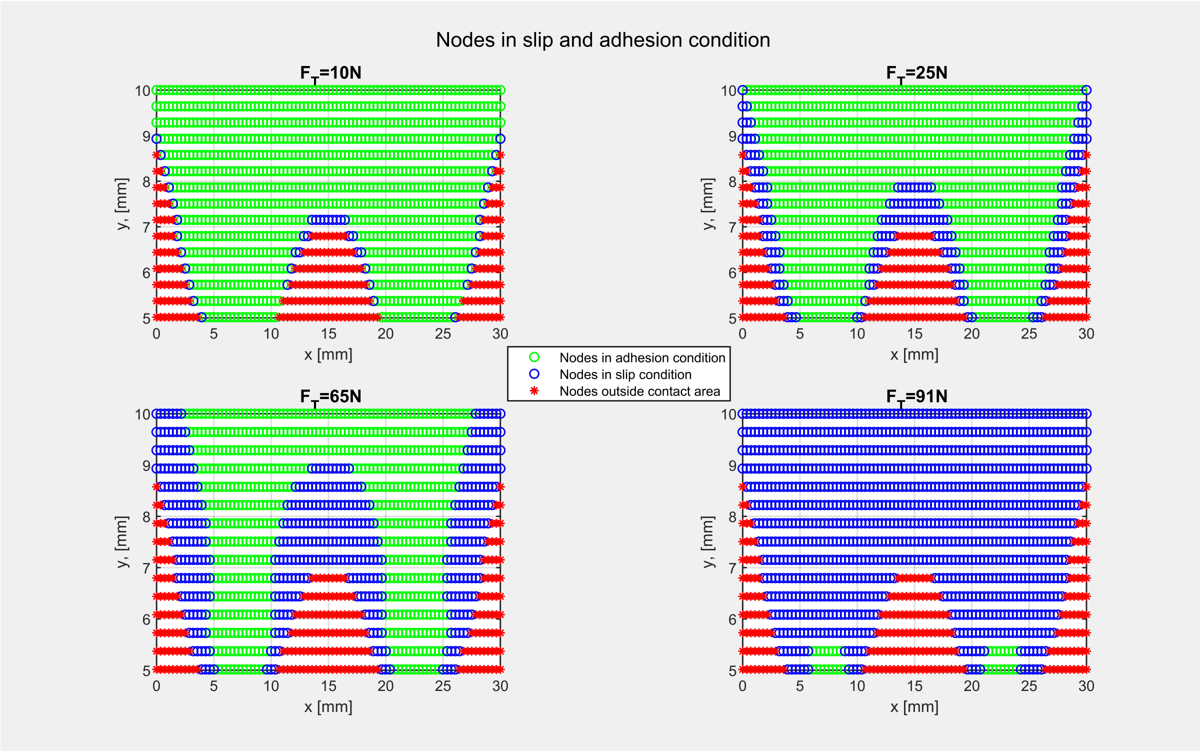

Figure 60: Nodes condition in contact area with tangential load

TABLE XI: NORMAL AND TANGENTIAL STIFFNESS FOR SYMMETRIC DAMPER

	Stiffness Value [N/mm]
K_N	1,56 10^6
K_T	4.90 10^5

While normal contact stiffness is constant as the normal force increases, it may not hold for the tangential contact stiffness. Since the two problems are uncoupled and the tangential problem receives as input the data from the normal contact problem, the latter one directly influences it. We can consider the F_T - $/delta$ relation for $F_N = 155N$ and $F_N = 257$, as shown in Figure 61 to see whether there is any sensible change in the slope. We can see how the slope stays constant for most of the curve before approaching the tangential force limit which depends on the normal load.

7.6 Normal and tangential contact stiffness calculation

We can finally calculate the K_n and K_t from the data collected so far. In order to calculate the actual contact stiffness, we should get rid of the compression of the two bodies in contact, however, since we are looking for an approximation, it can be neglected at first. As seen in Figure 59, the slope of the curve is constant as the applied normal force increases. The same consideration can be done for the tangential stiffness, which is constant for most of the curve, before getting closer to the limit value $F_T = \mu F_N$. The stiffness values are reported in following table.

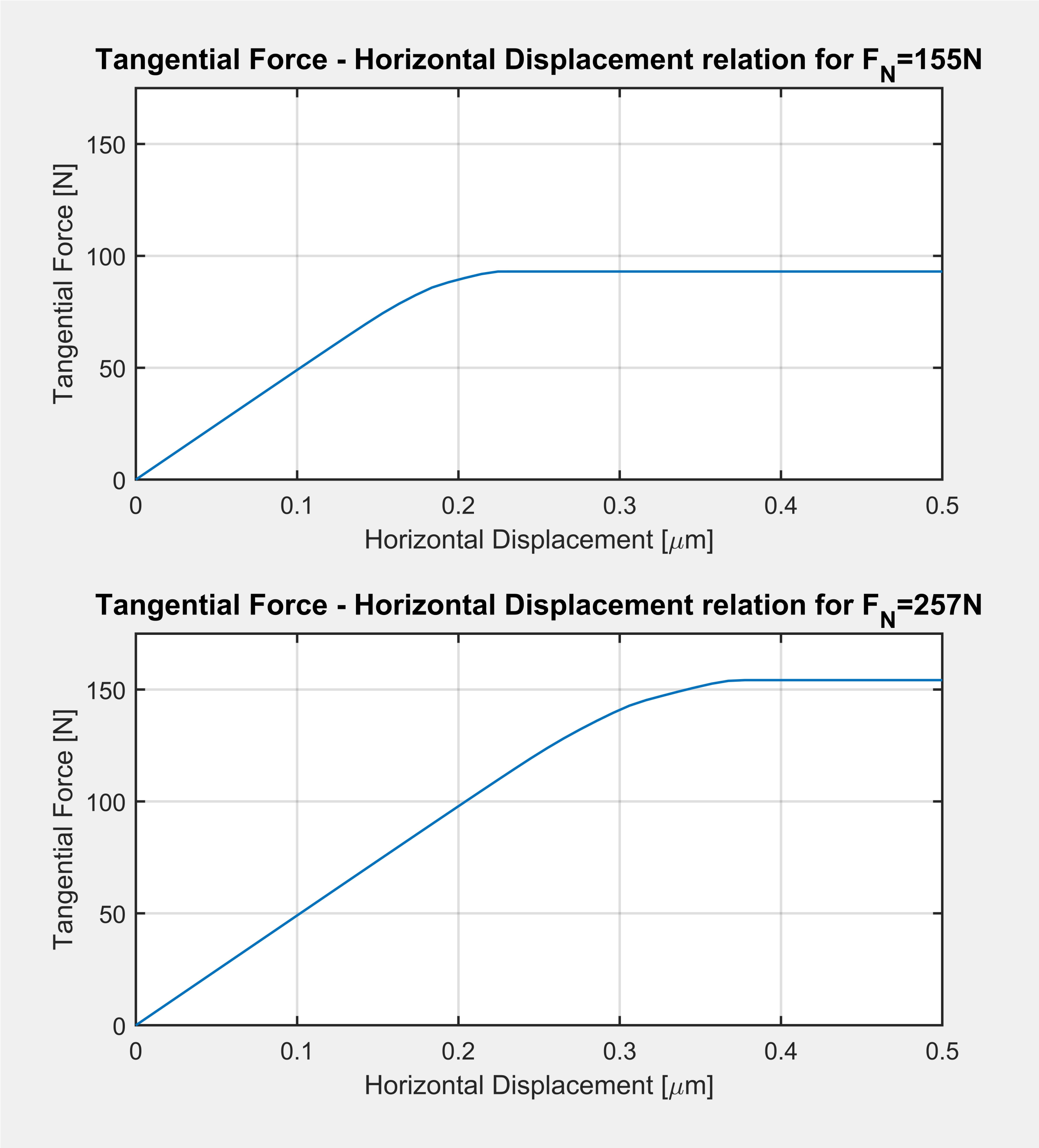

Figure 61: Tangential force - Displacement relation

CHAPTER 8

PLANE-PLANE CONTACT: ASSYMMETRIC DAMPER

8.1 FE model in Ansys

As for the symmetric case, the contact of the damper with the underplatform was simulated by a plane-plane contact with a cube's surface. However, the main dimensions, offsets and material properties were the same we used in the full FE model, and they are shown in Figure 62 along with the FE model in Ansys APDL. Attention was focus on the contact related to the damper's cases rather than on the surface in contact with the left blade.

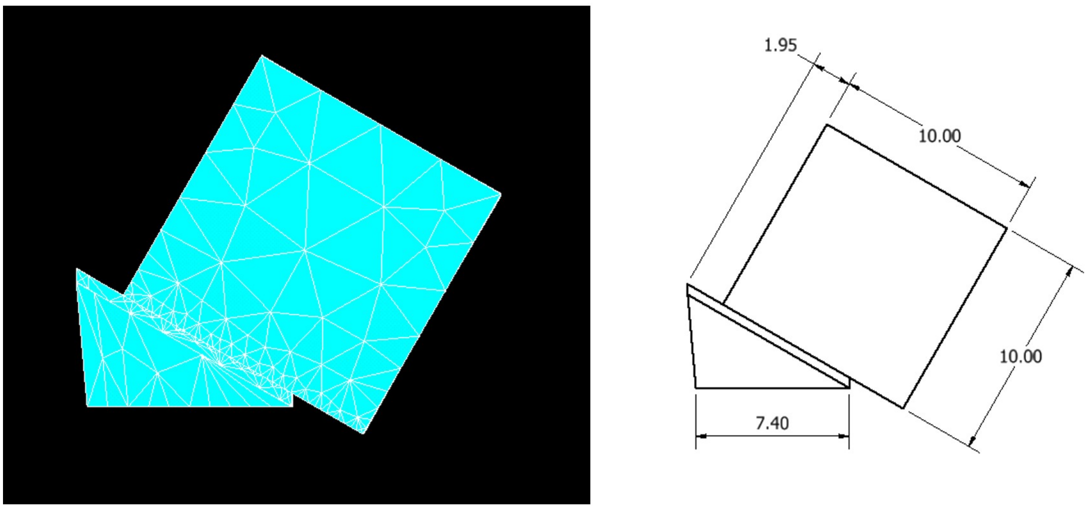

Figure 62: Sketch with main dimensions of the asymmetric damper-block model

The main difference with the symmetric case is that the potential contact area is not a single one, but is made up of two separate areas due to the presence of the two cases on the damper's surface. Each of the potential contact areas is made up of 36x16 square elements, for a total of 576 elements each.

8.2 Applied forces

We need to identify the F_N and F_T acting at the contact interface between the damper and the underplatforms in the experiments, such that we can apply them at the distant nodes of our model. If we assume that the tangential force follows the Coulomb friction theory, that is $F_T = \mu F_N$, and considering that F_c=350N, we have $F_N = 303N$ and $F_T = 175N$.

8.3 Master nodes selection

The 1258 nodes inside the case's surfaces were chosen as master nodes as far as the contact nodes are concerned, while for the distant nodes of the damper, the interested areas are two: each of the two wires which pull the damper upwards passes below the cases, therefore the areas on the same normal direction of the wires are chosen. They are shown in Figure 63.

For the distant nodes of the block we take the ones lying on the area opposite the contact one, as already done for the symmetric damper. Also in this case, the reference system is placed in the bottom left of the contact area on the damper, with the x-axis along the long edge, and the y-axis along the longer one.

8.4 Results to the normal contact problem

From the normal contact problem solution we have the pressure distribution over the two damper's contact areas, which is shown in Figure 64. It is worth noticing the symmetry in

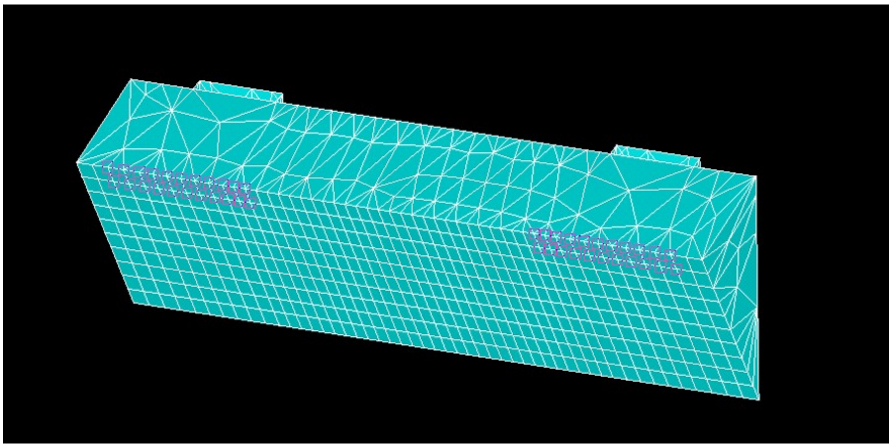

Figure 63: Distant nodes selection in asymmetric damper

the pressure distribution, being it specular over the two contact areas. With respect to the symmetric damper, we can see a higher pressure in the middle part, in correspondence of the wires position. Moreover, we can see a relevant 'edge effect'.

From this point on and for the rest of the chapter, for clearness and simplicity's sake, we are going to consider just one of the two contact areas, since the same holds for the second area due to symmetry. In Figure 65 we have the nodes which remain in contact after the F_n has been applied. While in Figure 66 we have the maximum and mean pressure as a function of the applied normal force.

It is also interesting to see how the damper's surface deforms under the load application as shown in the following.

8.5 Results to the tangential contact problem

In Figure 68 we can appreciate the evolution within the contact of the nodes condition.

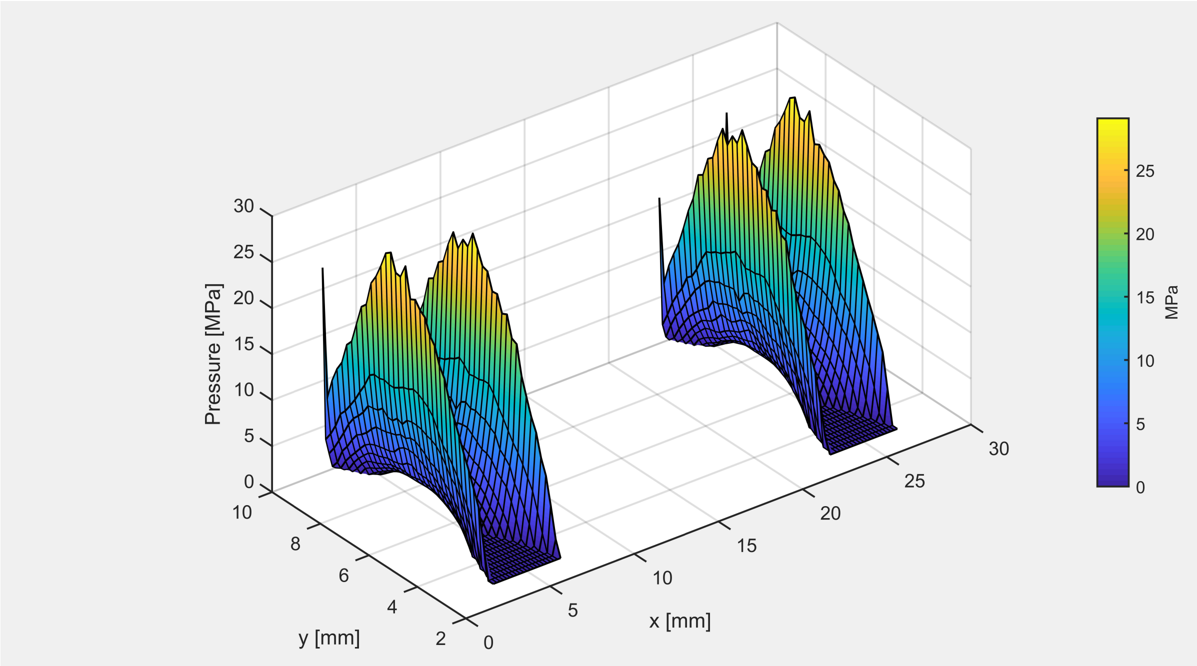

Figure 64: Pressure distribution over contact area

While in Figure 69 we have the relation between the applied F_T and the horizontal displacement δ. We can notice in this case, as for the symmetric damper, that within the linear field, the slope of the curve keeps constant as the F_T increases.

8.6 Kn and Kt values

Finally we can calculate the stiffness values which are shown in Table XII.

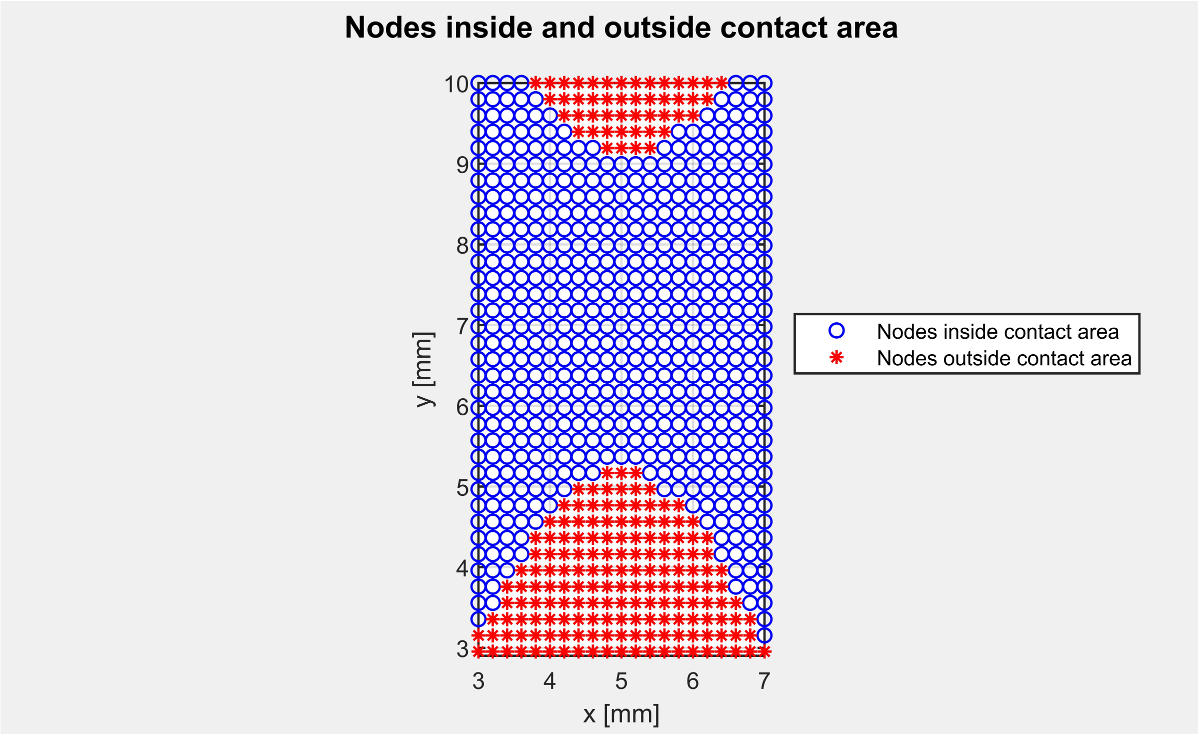

Figure 65: Nodes inside and outside contact area

TABLE XII: NORMAL AND TANGENTIAL STIFFNESS FOR ASYMMETRIC DAMPER

	Stiffness Value [N/mm]
K_N	4.71 10^5
K_T	1.50 10^5

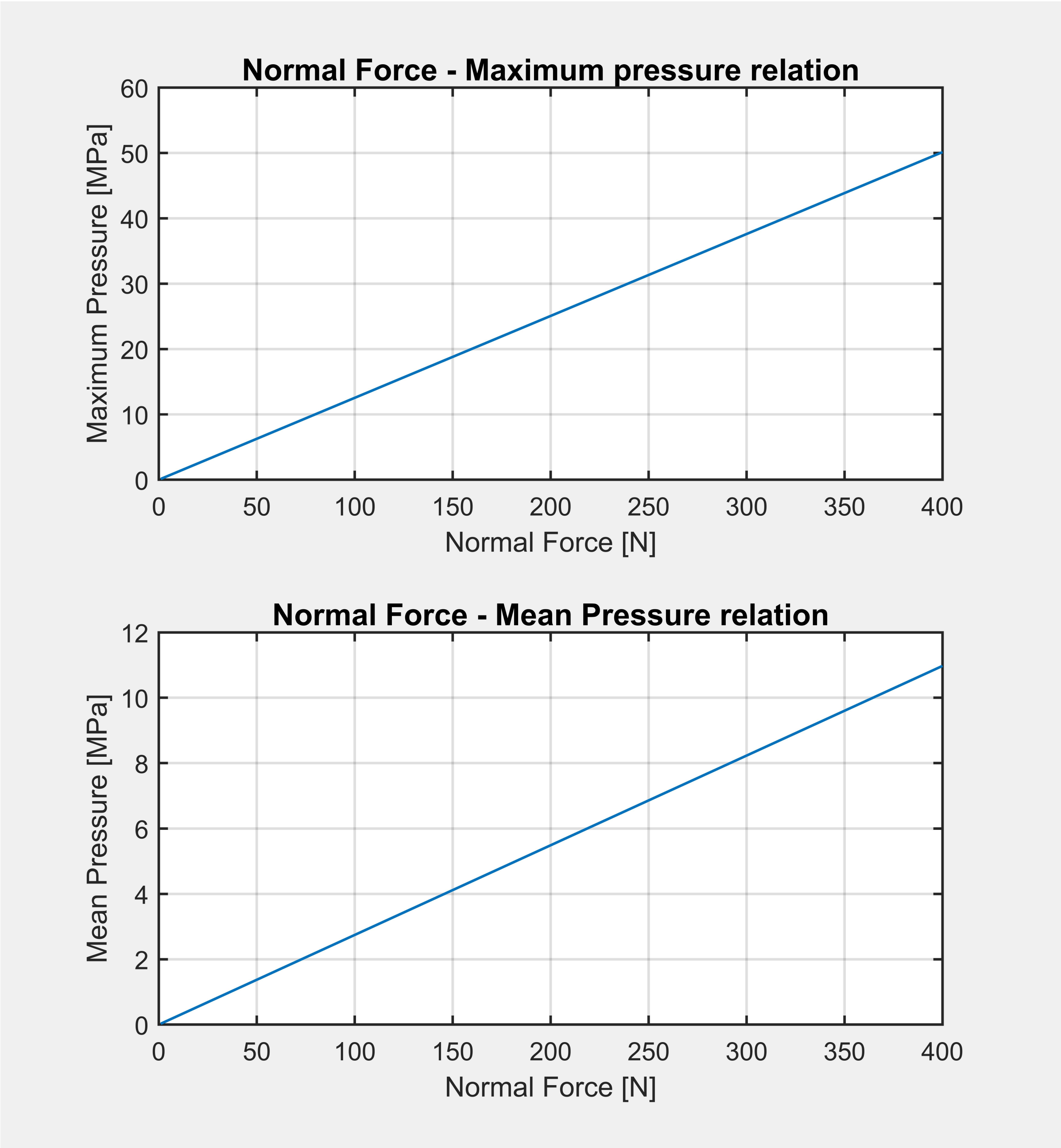

Figure 66: Maximum and mean pressure as a function of the normal force

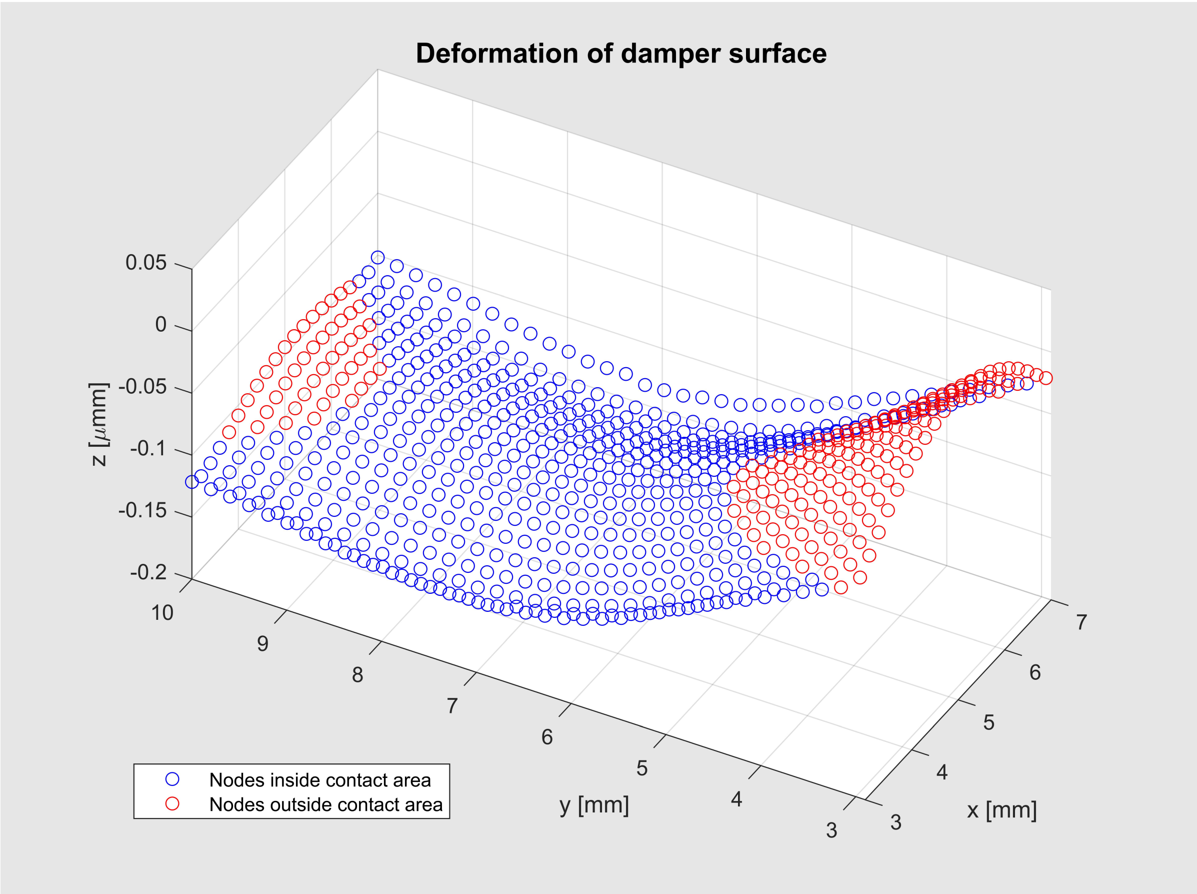

Figure 67: Deformation in one the dampe's cases under loaded condition

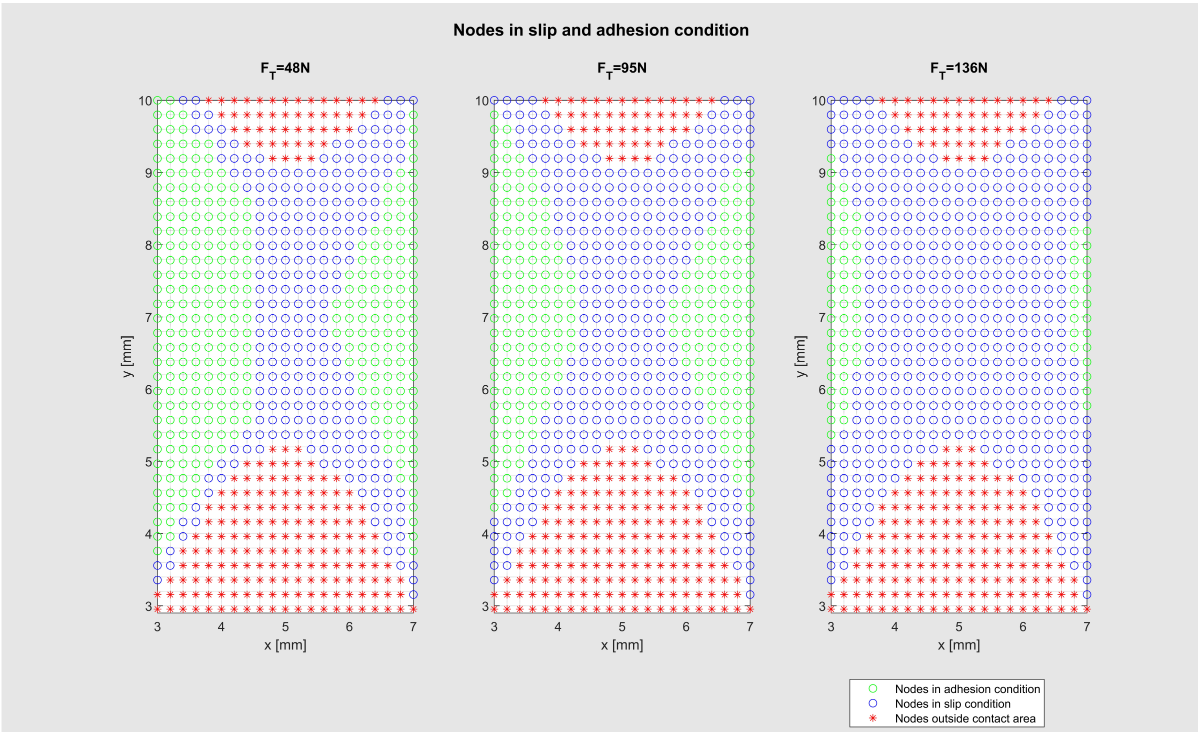

Figure 68: Slip and adhesion points for different F_T with $F_N = 303N$

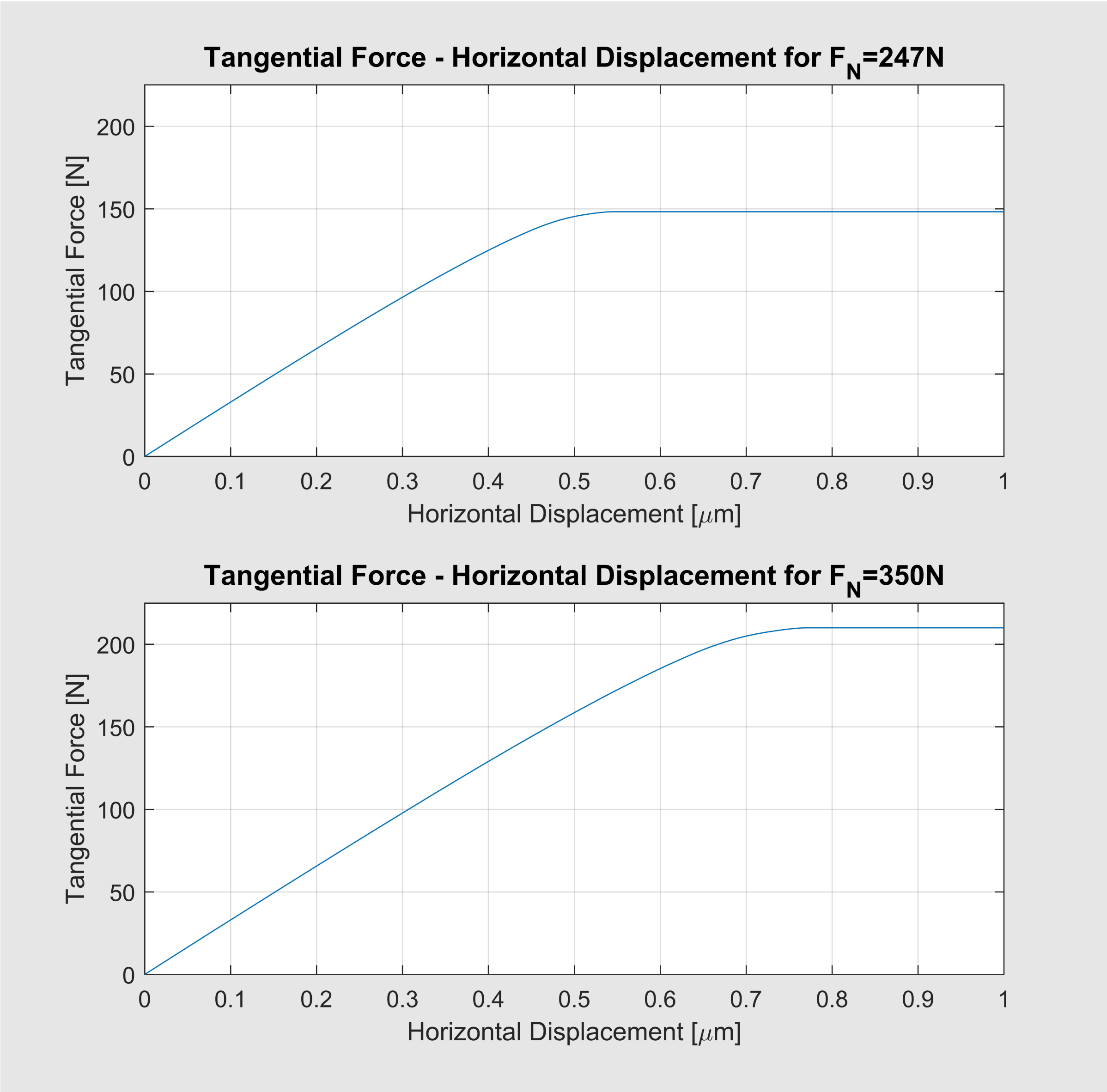

Figure 69: Tangential force - Displacement relation

CHAPTER 9

NON-LINEAR NUMERICAL METHOD RESULTS AND COMPARISON WITH EXPERIMENTS

Now that we have the normal and tangential stiffness for the symmetric and asymmetric case, we can use them as input for the non-linear numerical method explained in Appendix C, such that we can draw a final comparison with the plots for the forced condition coming from the experiments.

9.1 Symmetric damper

9.1.1 Non-linear method results with found Kn and Kt values

For the $K_n and K_t$ to be used here, we refer to the values reported in Table XI. It is worth remarking that a first verification of the other input parameters, such as the reduced mass and stiffness matrices and the damping coefficients, was performed in Section 5, when making the comparison of the linear part for the free condition results with the experimental one.

In Figure 70 we have the response calculate by the non-linear numerical method for such inputs, along with the system response for $F_c = 350N$ and $F_c/F_e = 194$ as shown at the beginning in Figure 11.

We can see that the non-linear response is close to the experimental results, meaning that the approximation of the stiffness values is sufficiently close to the real ones.

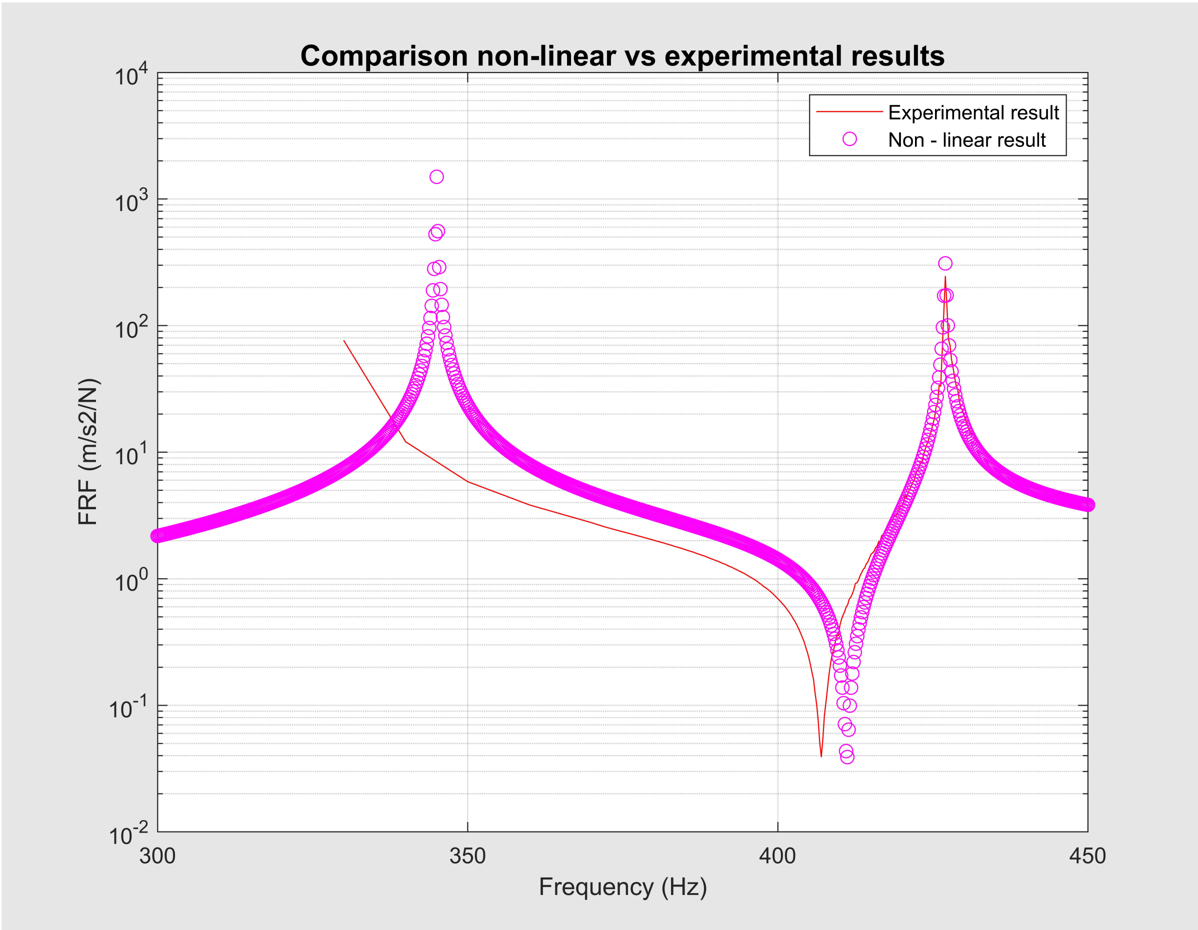

Figure 70: Comparison of the non-linear response with the experimental results

9.1.2 Comparison with damper conditions after experiments

Besides the comparison with the plots coming from experiments, we can interpret the found data in the light of the damper conditions after experiments. In order to make it, we need to consider the pressure distribution coming from the solution to the normal contact problem in section and consider the damper condition after experiment. We can see that the two points in which we have the highest pressure, actually correspond to the worn areas in damper, further verifying the validity of the followed approach. Moreover it is also in agreement with the theoretical and experimental analysis performed by Kenan Y.[8]

9.2 Asymmetric damper

9.2.1 Non-linear method results with found Kn and Kt values

For the asymmetric damper we consider the stiffness value present in Table XII. In Figure 71 we have the comparison between the non-linear result and the experimental ones. This case presents one issue which was not present in the symmetric case: while there, due to symmetry we could assume that the stiffness values were the same on the right and left contact, here we cannot longer make this assumption. Since we have only the stiffness values for the right contact only, we need to make an assumption on the missing stiffness. From the equilibrium of the forces acting on the damper when in between the blades, we can see that assuming a tangential force just below the limit μF_N, a perfect balance is reached between the F_C and the forces involved in the contact with the right blade, with almost null influence of the contact on the left. Therefore, we can assume to a reasonably high contact stiffness for the left contact such as $10^6 K/mm$

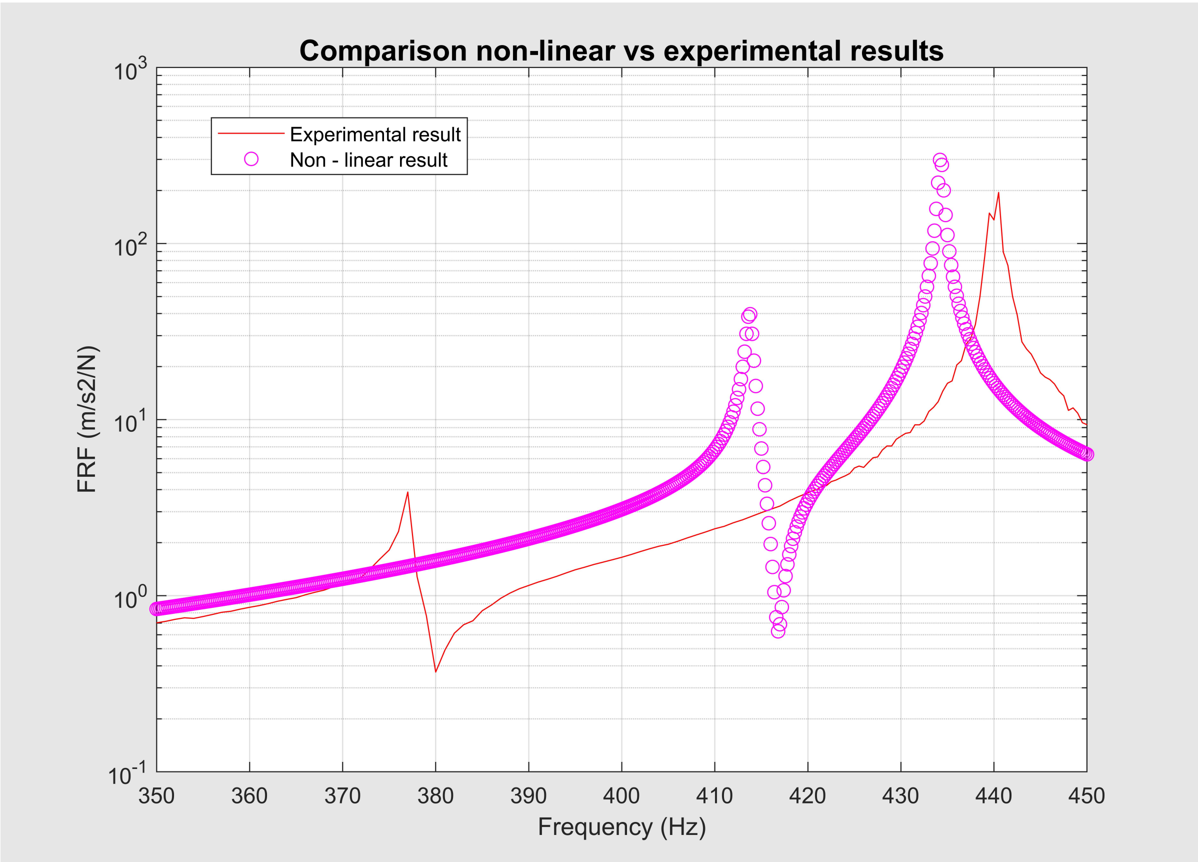

Figure 71: Comparison of the non-linear response with the experimental results

We can see that it is significantly close for the second mode, while it overestimates the first resonance frequency.

9.2.2 Comparison with damper conditions after experiments

As already done for the symmetric damper, we consider the pressure distribution obtained from the normal contact problem. By looking at the damper's surface condition after experiments, we can notice that the highest pressure is close to the worn area, however it is actually more towards the inner part. Therefore, a further study should be performed to investigate the 'edge effect'.

CHAPTER 10

CONCLUSIONS

The followed approach proved to be suitable to find a first approximation of the contact stiffness values, specially in the case of a symmetric damper. However, even though it was less efficient for the asymmetric damper, the vicinity to the second resonance frequency let us know that the order of magnitude of the normal contact stiffness was fine, while the main issue was related to the overestimation of the tangential contact stiffness. Having the possibility to have at least a rough approximation of the contact stiffness is valuable since it allows reducing the field of possible values in case iterative procedures are to be used.

APPENDICES

Appendix A

FE MODEL MESHING PROCESS

When dealing with contact problems, the mesh in the contact area is of fundamental importance since the nodes on the two bodies must superpose perfectly, otherwise the accuracy would be compromised. It can be easily carried out when dealing with planar contact areas, but in case of non-planar ones, some problems arises, indeed, numerous issues can be found when trying to mesh curved areas in Ansys APDL. Among them we have the difficulty in creating an area over a sphere surface and the impossibility of directly meshing a non-planar area with regular quadrilateral elements, which is a fundamental requirement in this step, and

Therefore, a well-defined approach need to be found in order to overcome the above mentioned problems.

If we have the semi-sphere model, in Ansys APDL it is difficult to project a given contact area on a curved surface. Therefore, it is better to have the edges of the contact area already available when importing the model in Ansys APDL. Moreover, even if the curved contact area is already present, it is not possible to directly mesh the area with quadrilateral elements. The problem can be overcome by having planar areas, sharing a common edge with the curved contact area, which can be meshed with quadrilateral elements before being able to mesh the curved area. The modelling part is performed into a standard CAD software, such as Solidworks or Desktop Inventor, which present a wider amount of features for this step. After creating the half-sphere and the block as single parts, we need to define the contact area on both bodies,

Appendix A (continued)

such that we can have a perfect alignment. While delimiting the potential contact area is straightforward on the block's surface, that is not the case for the half-sphere model.

The first step is to create a plane parallel to the tangent plane at the first point which would be in contact with the block. On the new plane we can easily draw the square potential contact area, with an edge of $1mm$, which is projected on the half-sphere surface as shown in Figure 72. It is required to divide the half-sphere surface into two areas by using the projected lines, otherwise they would not appear into Ansys APDL when importing the model.

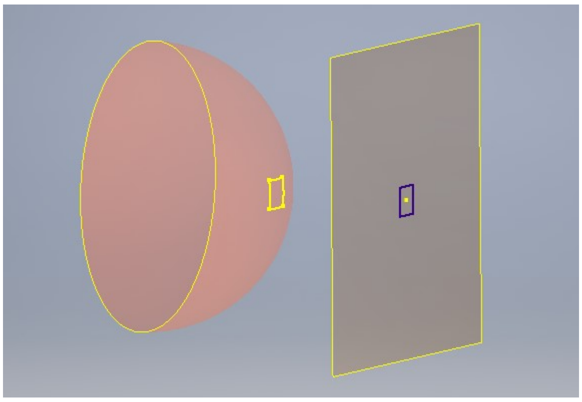

Figure 72: Projection potential contact area over half-sphere surface

As already mentioned at the beginning, having a well-defined area over the curved surface is not sufficient to be able to mesh it, therefore we need to build planar surface with sharing edges with it. Moreover, unless these surfaces are part of a volume, they would not be easily

Appendix A (continued)

recognized in Ansys, therefore we create a new volume as shown in Figure 73, which needs to be subtracted from the half-sphere in order to avoid issues i.e a solid volume within another one.

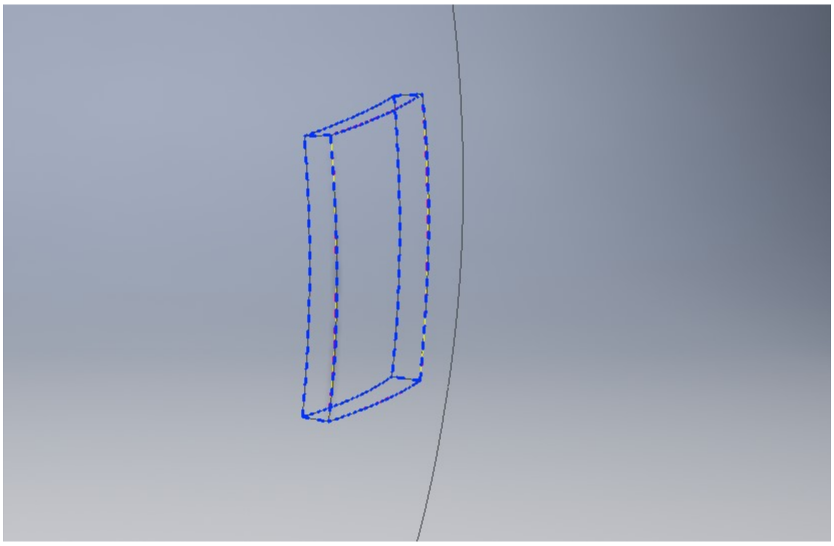

Figure 73: Sketch with main dimensions of the asymmetric damper-block model

As far as the block is concerned, drawing the potential contact area on its surface, would allow both having it already available in Ansys, after we have split the surface into two area as done for the sphere, and aligning it perfectly with the edges of the projected area over the half-sphere surface when building the assembly with both parts, as shown in Figure 74.

Appendix A (continued)

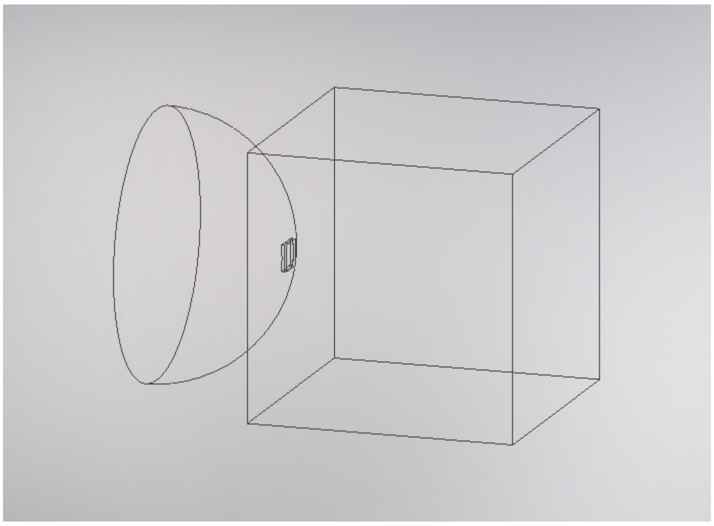

Figure 74: Half-sphere and block assembly CAD models

After the assembly has been imported in Ansys APDL, before meshing the curved area, we need to mesh the adjacent planar areas first. In Figure 75 we have the half-sphere model as imported in Ansys model, while in Figure 76 have to two steps to follow to mesh the curved area.

The final meshed bodies are shown in —-.

In order to verify the nodes alignment, we can plot the vertical position of the nodes in the potential contact area on both bodies for two different sections at constant x coordinates ().

We can see how they are well aligned, meeting the main requirement we wanted. It is worth remarking that this approach provide us with an easy and fast method to mesh the curved area. However, there is one main limitation: it is able to guarantee an accurate alignment provided

Appendix A (continued)

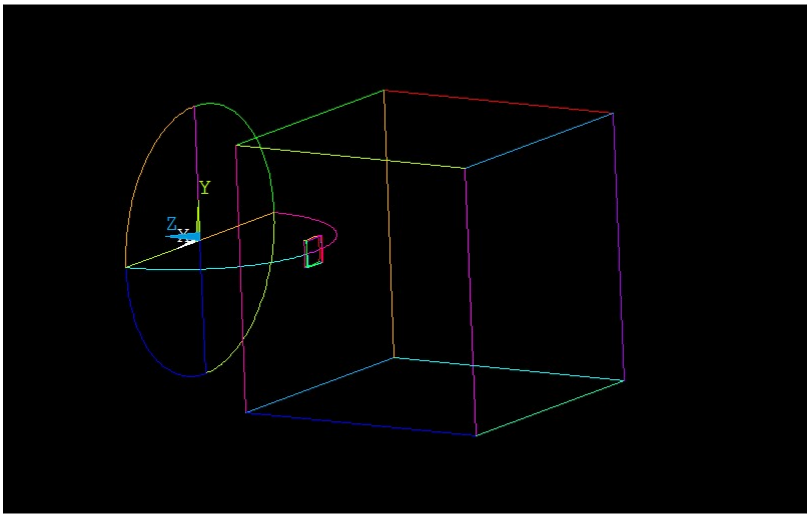

Figure 75: Half-sphere and block as imported in Ansys APDL

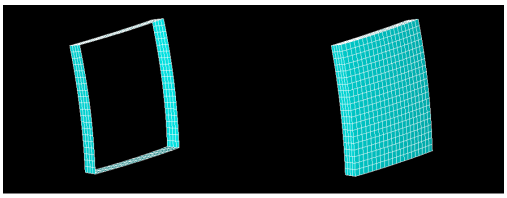

Figure 76: Meshing curve area steps

Appendix A (continued)

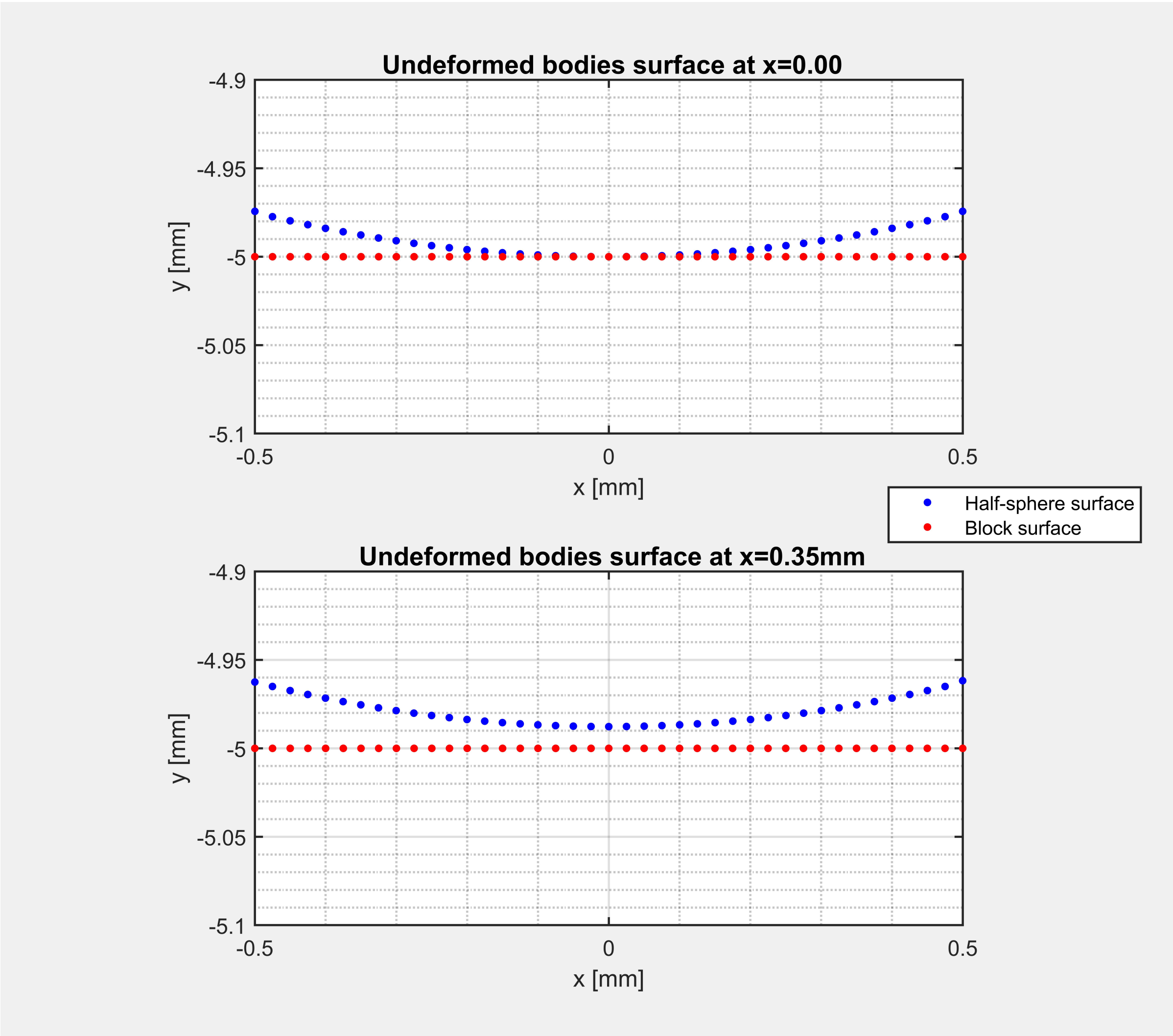

Figure 77: Underformed bodies surfaces at x=0,00 mm and x=0.35 mmm

Appendix A (continued)

that the curved surface to be meshed is relatively small if compared with curvature in that point, which was actually true for this case.

Appendix B

NON LINEAR NUMERICAL TOOL

B.1 Code overview

A numerical tool was developed in Matlab at the Politecnico di Torino, which allows calculating the blades response in the free and forced condition. It is able to model the underplatform damper's behaviour, based on its main physical characteristics, provided the availability of the blades' stiffness and mass matrix extracted from the FE model, after they had been reduced with the Craig-Bampton method. The reduction allows having matrices of smaller dimensions such that they can be handled within Matlab. Therefore, the FE model of the damper is not required at this stage.

B.2 The Craigh-Bampton condensation method

The Craigh-Bamption condensation method is on the partitioned of the model DOFs u_a into boundary DOFs u_b and internal DOFs u_L which are to be condensed according to

$$u_A = \begin{Bmatrix} u_B \\ u_L \end{Bmatrix} = \begin{bmatrix} I & 0 \\ \phi_R & \phi_L \end{bmatrix} \tag{B.1}$$

where

- ϕ_R is the rigid body vector
- ϕ_L is the base modeshapes

Appendix B (continued)

- q is the modal DOFs

being the matrix on the left hand side of Equation B.1 the Craig-Bampton reduction matrix. Therefore, it relies on two aspects: the first one represented by the static modes, which are obtained by applying a unit forces on the DOFs linked to u_b, while the second one is represented by the internal vibration modes. It is one of te best method when dealing separately with subsystems which are to interact with each other.

B.3 Master nodes selection

The master nodes choice is fundamental, since they define the remaining DOFs after the condensation process. They are divided into four categories:

- Left nodes, which are the nodes selected to be in contact with the left blade
- Right nodes, which are the nodes in contact with the right blade
- Force nodes, which is the nodes where the exciting force is applied
- Other nodes, which are the nodes where the accelerometer are attached

B.4 Input parameters

The required input parameters are summarized in the Table XIII. The parameters related to the damper can be easily collected in the used CAD software by setting the material density.

B.5 Contact model

The Hooke's contact model is considered for the contact between the damper and the underplatform. Basically the contact stiffness is represented by the stiffness of three equivalent

Appendix B (continued)

TABLE XIII: INPUT PARAMETERS FOR NON-LINEAR NUMERICAL TOOL

Input
Damper mass
Damper inertia moments
Coordinates of damper centre of mass
Number of contact nodes left/right
Contact angle
Contact stiffness
Friction coefficient
Damping coefficients
Centrifugal force
Excitation force

springs, fully uncoupled, along the three principal axis: one normal to the contact surface, and two laying on it.

B.6 Output data

In the final data we can find the system response in three different conditions

- Free response, which is performed without the damper in between the blades.
- Stuck response, linear calculation for the forces responce, done by simulating the behaviour of the damper, assumed to be connected to the underplaforms via the springs seen in the previous section with the contact stiffness provided by the user as input
- Non-linear response, which solves the forced condition with an iterative procedure, considering the input data concerning the damper

B.7 Node condition

Each node within the contact area can be in any of the following three conditions:

Appendix B (continued)

- Slip condition, if the a tangential displacement
- Stick condition, if the is no any relativo displacement
- Lift condition, if there is a relative normal displacement

The first check is to verify whether the couple of nodes lay on the contact plane or not. This is achieved simply by calculating their vertical position as

$$n_{id} - n_{ib} > 0 \tag{B.2}$$

in which the first subscript i stands for any couple of nodes in the contact area, while the second subscript indicates the body it belongs to, either the damper or the blade. In case there is no a vertical displacement, a further verification is performed to establish they are in stick or slip condition.

$$|T_x| > |\mu N_i| \tag{B.3}$$

While is to be applied in both direction on the contact plane. It is holds then we they are in slip condition, otherwise they are in stick condition.

B.8 Equilibrium equations

Assuming that both the excitation and the response are periodic, the HBM method is used, which works in the frequency domain. The general equilibrium equation of the blades is as follows

Appendix B (continued)

$$M\ddot{u}(t) + C\dot{u}(t) + Ku(t) = F_e(t) - F_c(t) \tag{B.4}$$

where F_c is the force in the contact with the dampers. Displacement and force can be expressed using Fourier analysis as

$$u^*(t) = u_0^* + R\Big(\sum_{n=1}^{N_h} u_n^* e^{in\omega t}\Big) \tag{B.5}$$

$$F_e(t) = F_{e0} + R\Big(\sum_{n=1}^{N_h} F_n e^{in\omega t}\Big) \tag{B.6}$$

$$F_c(t) = F_{c0} + R\Big(\sum_{n=1}^{N_h} F_c e^{in\omega t}\Big) \tag{B.7}$$

Where N_h is the number of harmonics, being the first order sufficient for this case the above equations become simply

$$u^*(t) = u^*0 + R\Big(u_1^* e^{in\omega t}\Big) \tag{B.8}$$

$$F_e(t) = F_{e0} + R\Big(F_{e1} e^{in\omega t)}\Big) \tag{B.9}$$

$$F_c(t) = F_{c0} + R\Big(F_{c1} e^{in\omega t)}\Big) \tag{B.10}$$

Appendix B (continued)

Substituting them into Equation B.4, we can apply the HBM method. Therefore, from the time domain we shift to the frequency domain. Setting the balance equation for each harmonic, we get two equations, one static and one dynamic

$$Ku_0 = F_{e0} - F_{c0} \tag{B.11}$$

$$Du_1 = F_{e1} - F_{c1} \tag{B.12}$$

in which D is the dynamic stiffness of the blades. As far as the damper is concerned, we have the following equilibrium equation

$$M\ddot{u}(t) + C\dot{u}(t) + Ku(t) = \mathbf{CF}(t) - F_c(t) \tag{B.13}$$

where **CF** is the centrifugal force. Considering that the damper is conceived as a rigid body within the numerical method developed, it simply becomes

$$M\ddot{u}(t) = \mathbf{CF}(t) - F_c(t) \tag{B.14}$$

The information regarding the displacement of the damper, is applied at its centre of mass, **u**(t)=u(t, v(t), w(t), β_x(t), β_y(t), β_z(t) being the displacement vector. As already done for the blades, we shift from time to frequency domain, truncating at the first term

Appendix B (continued)

$$\mathbf{u}(t) = u_0 + u_1^c cos(\omega t) + u_1^s sin(\omega t) \tag{B.15}$$

$$F_c(t) = F_{c0} + F_c(u_1)^c cos(\omega t) + F_c(u_1)^s sin(\omega t) \tag{B.16}$$

$$\mathbf{CF} = CF_0 \tag{B.17}$$

Therefore the equilibrium equation becomes

$$\mathbf{CF} = F_{c0} \tag{B.18}$$

$$-\omega^2 M u_1^c = F_c(u_1)^c \tag{B.19}$$

$$-\omega^2 M u_1^s = F_c(u_1)^s \tag{B.20}$$

B.9 Iterative procedure

The iterative procedure starts by guessing u_0, u_1^c, u_1^s, which are transformed into time domain by using a Fast Fourier Transform. The **u(t)** is converted into local displacement vector which is used to compute the force vector $T_i = \tau$ The contact forces vector are then converted to frequency domain via FFT. The residuals are computed for the static and dynamic

Appendix B (continued)

balance equation of the damper, if they are below the chosen tolerance, the solution is accepted, otherwise another guess is done for the next iterative step.

Besides the mass and stiffness matrices, we need to provide some damper's information. The required input data is summed up in Table XIII

The interaction of the modelled damper with the two blades happens through the chosen contact points. However, the damper is modelled as a rigid body, without considering its bulkiness.

The damper's parameters are easily obtained from the CAD assembly model, if the reference system was kept unchanged when passing from Solidworks to Ansys APDL. The coordinate system consistency is important since the system origin is moved to the damper's centre of mass, and all the nodes coordinates are transform accordingly.

Appendix C

NUMERICAL METHOD FOR NORMAL AND TANGENTIAL CONTACT PROBLEM

C.1 Method overview

While closed-form solutions are available for the contact problem of well-defined geometries such the sphere-sphere and the sphere-plane contact, a different approach is needed when dealing with other geometries. Numerical methods come to help for those cases, among which the finite element (FE) approach is one of the most important. The problem is that most of the approaches inside the FE methods need to add extra dofs, increasing the dimension of the stiffness and mass matrices of the full FE model. The considered numerical method hereby, uses the stiffness and mass matrices coming from the FE model after they have been reduced by applying the Guyan reduction method allowing processing the matrices by an in-house software.

C.2 Assumptions

The main assumptions are

- The material of the bodies in contact is linearly elastic, and deformation are small.
- The contact surface is assume to be perfectly smooth, therefore, roughness is neglected.
- The friction coefficient is constant, and the Amonton-Coulomb model of friction is used, assuming it holds locally at each contact point.
- The normal and tangential contact problems are uncoupled.

Appendix C (continued)

C.3 Guyan condensation method

The Guyan condensation method is based on the assumption that for low frequency modes, the inertia force of nodes to be condensed is negligible with respect to the elastic forces acting on the master nodes, which are the DOFs we want to actually keep. It performs a division of the full FE DOFs into two categories: the one on which the applied force is different from zero, called active or master dofs, and the ones on which the applied force is null, called delected dofs. Therefore the stiffness equation of the full FE model

$$[K_n]\{x_n\} = \{F_n\} \tag{C.1}$$

is partitioned into two equations

$$\begin{bmatrix} K_{aa} & K_{ad} \\ K_{da} & K_{dd} \end{bmatrix} \begin{Bmatrix} x_a \\ x_d \end{Bmatrix} \begin{Bmatrix} F_a \\ F_d \end{Bmatrix} \tag{C.2}$$

Since F_d is equal to zero, the second equation in equation Equation C.2 can be written as

$$[K_{da}]\{x_a\} + [K_{dd}]\{x_d\} = \{0\} \tag{C.3}$$

when solving for the displacement of the deleted dofs

$$\{xd\} = -[K_{dd}]^{-1}[K_{da}]\{x_a\} \tag{C.4}$$

Substituting into the first equation in equation Equation C.2, we obtain

Appendix C (continued)

$$\left[K_{aa}\right]\left\{xa\right\}+\left[K_{ad}\right]\left[K_{dd}\right]^{-1}\left[K_{da}\right]\left\{x_a\right\}=\left\{F_a\right\} \tag{C.5}$$

through manipulation we have the transformation matrix:

$$\left[T_d\right]=\begin{bmatrix}\left[I\right]\\ \left[K_{dd}\right]^{-1}\left[K_{da}\right]\end{bmatrix} \tag{C.6}$$

Finally, we have the relation between the stiffness matrix of the full FE model and the reduced stiffness matrix $[K_a^G]$

$$\left[K_a^G\right]=\left[T_s\right]^T\left[K_n\right]\left[T_s\right] \tag{C.7}$$

According to Guyan, the same transformation applies to the mass matrix

$$\left[M_a^G\right]=\left[T_s\right]^T\left[M_n\right]\left[T_s\right] \tag{C.8}$$

Due to the main assumption made at the beginning, this method is mostly suitable when dealing with static cases.

C.4 Master nodes selection

The master node choice is fundamental since it defines the remaining DOFs from the full model. They are divided into two categories

Appendix C (continued)

- Contact nodes, which are the ones inside the potential contact area whihc needs to be decided a priori
- Distant nodes, which are far from the contact area. They are the application point of the chosen displacement and the found normal and tangential forces

C.5 Normal contact problem

At the basis of the normal contact problem solution we have the following three equations - Compatibility of displacements, which states that in any point of the potential contact area the sum of the elastic displacements, the distance between the bodies and the rigid bodies approach must be greater or equal to zero. It is written as follows

$$h(x, y) + (u_{1z} - u_{2z}) + (\delta_{n1} - \delta_{n2})e >_0 \tag{C.9}$$

where the first term is the distance of the profiles in the underformed state, while u_z is the vertical displacement, and δ is the rigid-body approach.

- Displacements-forces relation, which is described as follows

$$Ku = f \tag{C.10}$$

where K is the matrix of the full FE model already reduced using the Guyan condensation method. Therefore, u and f are the displacements and the applied forces regarding the master nodes only.

Appendix C (continued)

-Equilibrium equation, which states that each point inside the potential contact area must be in equilibrium

$$f_{c1} + f_{c2} = 0 \tag{C.11}$$

Moreover the sum of all the forces along the vertical direction must balance the applied load F_N.

$$e^T \cdot f_{cz} = F_N \tag{C.12}$$

in which fcz is the vertical component of the forces in the potential contact area only. Therefore the classification of a point being either inside or outside the potential contact area, is performed according to the following equations:

$$h(x,y) + (u_{1z} - u_{2z}) + (\delta_{n1} - \delta_{n2})\mathbf{e} \begin{cases} = 0 & inside \quad contact \quad node \\ > 0 & outside \quad contact \quad area \end{cases} \tag{C.13}$$

$$f_{1z} = -f_{2z} \begin{cases} = 0 & insidecontactnode \\ > 0 & outsidecontactarea \end{cases} \tag{C.14}$$

Appendix C (continued)

C.6 Step 1: Reduction to vertical DOFs

Since the normal and tangential contact problems are assumed to be uncoupled, that is the tangential forces have no influence on the normal problem, we can further reduce the system by deleting the DOFs lying on the contact area. It can be done by partitioning the DOFs in the displacement-force relation as follows

$$\begin{bmatrix} K_{zz} & K_{zx} \\ K_{xz} & K_{xx} \end{bmatrix} \begin{Bmatrix} u_z \\ u_x \end{Bmatrix} = \begin{Bmatrix} f_z \\ f_x \end{Bmatrix} \tag{C.15}$$

where u_x stands for the tangential displacement along both x and y-axis, if we assumed the z-axis to be normal to the contact area. Isolating u_x from the second row in Equation C.15 and substituting in the first one we get

$$K_z u_z = f_z - K_{xx} K_{xz}^{-1} f_x \tag{C.16}$$

but $f_x = 0$ due to the coupling assumption, therefore **??** becomes simply

$$K_z u_z = f_z \tag{C.17}$$

C.7 Step 2:Vertical DOFs partioning

The vertical DOFs are further partitioned into components related to nodes inside the contact area, outside it and the distant nodes

Appendix C (continued)

$$\begin{bmatrix} K_{zii} & K_{zio} & K_{zi\delta} \\ K_{zoi} & K_{zoo} & K_{zo\delta} \\ K_{z\delta i} & K_{z\delta o} & K_{zi\delta\delta} \end{bmatrix} \begin{Bmatrix} u_z i \\ u_z o \\ u_z \delta \end{Bmatrix} = \begin{Bmatrix} f_{zi} \\ f_{zo} \\ f_{z\delta} \end{Bmatrix} \tag{C.18}$$

Isolating the displacement of the nodes outside the contact area u_{zo} and since f_{zo} is null, substituting in the first row we get

$$K_{zi}u_{zi} + K_{z\delta}u_{z\delta} = f_{zi} \tag{C.19}$$

which holds for the two bodies in contact. Considering the balance of all the forces acting in the vertical direction, as stated in the equilibrium equation in.., we have

$$K_{1zi}u_{1zi} + K_{2zi}u_{2zi} + K_{1z\delta}u1z\delta + K_{2z\delta}u_{2z\delta} = 0 \tag{C.20}$$

Combining it with the compatibility of displacement within the contact area and setting $\delta_{n2} = 0$ for simplicity, we get finally

$$(K_{1zi} + K_{2zi})u_{1zi} = -K_{1z\delta}u_{1z\delta} - K_{2zi}(\delta_{n1}e_i + h_i) \tag{C.21}$$

in which the only unknown is the vertical displacement of the nodes inside the contact area. But, it is required to know what the contact area actually is. Therefore, an iterative procedure was considered, as presented in the following section.

Appendix C (continued)

C.8 Step 3: Iterative procedure to solve the contact problem

A first guess of the true contact area is performed considering the whole interpenetration area for the provided δ_{n1} assuming a rigid body motion. It allows solving Equation C.21 for u_{1zi} and use the compatibility equation to get u_{2zi}. The force in the contact nodes is obtained from Equation C.19. In case in a specific node we have an applied force equal or smaller than zero, it is moved to the group of nodes classified as being outside the contact area. The displacement of the outside nodes is got from the second row of Equation C.18.

At this points it is possible to perform a verification of the consistency of the results found so far by applying the compatibility equation for the nodes outside the contact area. If the equation is not verified for a node, it is moved to inside nodes. In the end the set of inside and outside nodes will be different, defining a new contact area, and they are used to update the matrices K_{zi} and $K_{z\delta}$ for both bodies. They along with the updated true contact area will be the input for the next iteration starting from Equation C.21.

C.9 Tangential contact problem

The tangential contact problem receives as input from the normal contact problem the applied force in the contact area and the nodes vertical displacement.

C.10 Step 1: Reduction to tangential DOFs

As done for the normal contact problem, we separate the tangential DOFs from the vertical ones in the force-displacement equation

Appendix C (continued)

$$\begin{bmatrix} K_{xx} & K_{xz} \\ K_{zx} & K_{zz} \end{bmatrix} \begin{Bmatrix} u_x \\ u_z \end{Bmatrix} = \begin{Bmatrix} f_x \\ f_x z \end{Bmatrix} \tag{C.22}$$

Isolating the u_z from the second row and substituting in the first one, we get

$$K_x u_x = f_x - K_{zz} K_{zx}^{-1} f_z \tag{C.23}$$

which, since f_z is negligible due to the uncoupling assumption, becomes

$$K_x u_x = f_x \tag{C.24}$$

C.11 Tangential DOFs partitioning

The tangential DOFs can be divided into distant nodes and nodes inside or outside the contact area.

$$\begin{bmatrix} K_{xii} & K_{xio} & K_{xi\delta} \\ K_{xoi} & K_{xoo} & K_{xo\delta} \\ K_{x\delta i} & K_{x\delta o} & K_{x\delta\delta} \end{bmatrix} \begin{Bmatrix} u_x i \\ u_x o \\ u_x \delta \end{Bmatrix} = \begin{Bmatrix} f_{xi} \\ f_{xo} \\ f_{x\delta} \end{Bmatrix} \tag{C.25}$$

Substituting u_{xo} from the second row into the first one we get

$$K_{xi} u_{xi} + K_{x\delta} u_{x\delta} = f_{xi} \tag{C.26}$$

Appendix C (continued)

C.12 Contact area nodes partition

While $x\delta$ in Equation C.26 is known since it is an input parameter, we can further split the nodes in the contact area into nodes in adhesive condition and in slip condition. The classification is performed in each according to the following equation

$$f_{ix} < \mu f_{iz} \tag{C.27}$$

where the f_x is the tangential force applied in the specific node, while f_z is the normal load on it, coming from the normal contact problem. Therefore, Equation C.26 can be written as

$$\begin{bmatrix} K_{xiaa} & K_{xias} \\ K_{xisa} & K_{xiss} \end{bmatrix} \begin{Bmatrix} u_x ia \\ u_x is \end{Bmatrix} + \begin{bmatrix} K_{x\delta a} \\ K_{x\delta s} \end{bmatrix} \begin{Bmatrix} u_x \delta \end{Bmatrix} = \begin{Bmatrix} f_x ia \\ f_x is \end{Bmatrix} \tag{C.28}$$

Getting from the second equation

$$u_{xis} = Kzi^1 f_{xis} - (K_{xisa} u_{xia} + K_{xi\delta s} u_{xi\delta}) \tag{C.29}$$

Considering that the maximum value a tangential force can take is μf_{zis}, we can substitute it into Equation C.29 and substitute into the first row of Equation C.30. We have

$$K_{xia} u_{xia} + K_{x\delta} u_{x\delta} + f_{zxis} = f_{xia} \tag{C.30}$$

Appendix C (continued)

which hold for the two bodies. If we sum them together, taking into account that the forces in nodes in adhesion condition are equal and setting the displacement of the distant nodes of the second body to zero, we have

$$(K_{1xia} + K_{2xia})u_{1xia} + K_{1x\delta}u_{1x\delta} + (f_{1zxis} + f_{2zxis}) = 0 \tag{C.31}$$

C.13 Iterative procedure to solve the tangential problem

At the first iteration, all the nodes in the contact area provided by the normal contact problem are assume to be in stick condition. By applying the formulae above mentioned, we get to Equation C.31 which is solved for u_{xa}. It is subsequently used to find the tangential force f_{xia} in nodes in adhesion condition by solving Equation C.30. Therefore, we can overall tangential force applied at the contact interface. At this point, for each node we check whether Equation C.27 holds or not. If it doesn't, the node is moved into the slip node set, redefining the area of nodes in adhesion condition. The iterative procedure stops, when the for all the nodes in the adhesion set, Equation C.27 holds. At each further iteration, the DOFs related to nodes in slip condition are deleted, reducing the system further. In the end, the final output allows knowing the area of nodes in stick and slip condition, along with the tangential force F_T.

CITED LITERATURE

1.Botto D., Lavella M.: A numerical method to solve the normal and tangential contact problem of elastic bodies, Elsevier, 2015

2. Savito. M. Prove sperimentali di smorzamento per attrito con smorzatori sottopala in pala di turbina, 2005

2. Gola M., Liu T.: Design of a new test rig to evaluate under-platform damper performance. Proceedings of the ASME 2010 10th Biennial Conference on Engineering Systems Desing and Analysis, 2010

3. Hertz, H.R.: Uber die beruehrung fester elastischer koerper. Gesammelte Werke, 1895

4. Mindling, R.D. and Deresiewicz, H.: Elastic spheres in contact under varying oblique forces. ASME J. Appl. Mech, 1953

5. Mindlin, R.D,Compliance of elastic bodies in contact. ASME J. Appl. Mecha, 1949

6. Kenan Y., Daivs. J., Underplatform dampers for turbine blades: theoretical modelling, analysis and comparison with experimental data, ASME, 1999